University of Reading

Department of Meteorology

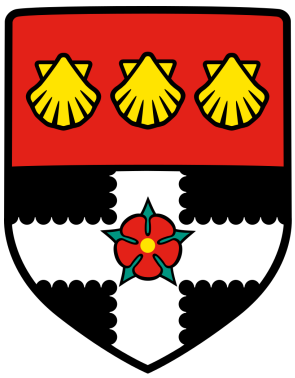

What is the global impact of 3D cloud-radiation interactions?

Sophia Alexandra Katja Schäfer

A thesis submitted for the degree of Doctor of Philosophy

September 2016

Declaration

I confirm that this is my own work and the use of all material from other sources has been properly and fully acknowledged.

Sophia Schäfer

Abstract

Clouds have a decisive impact on the Earth's radiation budget and on the temperature of the atmosphere and surface. In global weather and climate models, however, cloud-radiation interaction is treated in an approximate way that contributes to the large uncertainty due to clouds in climate predictions. One of the simplifications is to only consider radiative transfer in one vertical dimension and neglect horizontal radiative transfer. This thesis provides the first systematic estimates of the global impact of 3D cloud-radiation interactions in the shortwave and longwave. We show that 3D cloud effects consist of both horizontal transfer through cloud sides and horizontal transfer within regions.

We develop the longwave part of the SPARTACUS radiation scheme that incorporates treatment of these 3D effects in a one-dimensional radiation calculation at a numerical cost suitable for a global weather and climate model, and validate the scheme. SPARTACUS includes the effects of cloud internal inhomogeneity, of horizontal in-region transport and of the spatial distribution of in-cloud radiative fluxes. Algorithm evaluation is facilitated by an exact theoretical benchmark: for idealised optically thick cubic clouds, we can reason analytically that neglecting longwave 3D cloud side effects leads to an underestimation of cloud radiative effect (CRE) by exactly a factor of three.

We introduce a new measure of the cloud geometry information relevant to radiation in the "effective cloud scale" C_S, which only depends on cloud type. Analysis of the effective cloud scale of various cloud types demonstrates that $C_S = 1.0 \pm 0.4\,\mathrm{km}$ is a good estimate for the cloud scale of boundary-layer clouds, irrespective of their cloud type and of data source. More variety of cloud types at middle and high levels leads to a greater uncertainty range of $C_S = 5$ to $20\,\mathrm{km}$ for clouds above the boundary layer, with

a best estimate of $C_S = 10\,\mathrm{km}$.

We conduct offline radiation calculations on atmospheric states from a year of ERA-Interim re-analysis. We estimate that overall 3D cloud effects warm the Earth by about $4\,\mathrm{W\,m^{-2}}$, with warming effects in both the shortwave and the longwave, of $3\,\mathrm{W\,m^{-2}}$ and $1\,\mathrm{W\,m^{-2}}$ respectively at top-of-atmosphere and both about $2\,\mathrm{W\,m^{-2}}$ at the surface. Longwave heating and cooling in vertical layers is increased by up to $0.2\,\mathrm{K\,d^{-1}}$ and $-0.3\,\mathrm{K\,d^{-1}}$ respectively. In the shortwave, we have separated two different 3D effects. We find that the effect of transport through cloud sides has a cooling effect of around $-1\,\mathrm{W\,m^{-2}}$. This cooling is dominated by the previously rarely investigated effect of in-region horizontal transfer that significantly decreases cloud reflectance and warms the Earth's system by $5\,\mathrm{W\,m^{-2}}$. These 3D effects are neglected by current models, but are noticeably stronger than the effect of anthropogenic greenhouse gases and therefore definitely worth considering in climate simulations. We have shown for the first time how this can be achieved in a computationally affordable way.

Acknowledgements

I would like to thank all the people without whose help and support this work never could have been finished. First of all, many thanks to my supervisors Robin Hogan, Christine Chiu and Susanne Crewell (at the University of Cologne) for their guidance and support. I have learned a lot from them over the course of my project. A massive thanks especially to my lead supervisor Robin, who was always available for questions, invested a lot of time in my project and often had more confidence in it than I had myself.

Many thanks also to my Monitoring Committee, Helen Dacre and Chris Westbrook, for their support and constructive feedback. Jon Shonk and Mark Fielding provided greatly appreciated introductions into the algorithm that ultimately became SPARTACUS, the use of the 3D radiation code SHDOM and scanning cloud radars, and valuable discussions. Further, thanks to my collegues in the Initial Training for atmospheric Remote Sensing (ITaRS) Network for many interesting discussions, including some philosophical debates at around 2 am; and to the members of the work groups Crewell and Neggers at Cologne University and staff at ECMWF who were very welcoming and helpful during my secondments.

I would like to thank everybody in the Department of Meteorology for the great atmosphere and broad range of social activities that make this such a great place to work, especially the PhD students in 1U07 during my first year and in Lyle 505 during the remaining years, who endured my bouts of frustration when things were not working as planned; and to housemates over the years who helped with the practical issues of life in the UK. Many thanks also to the chaplains, assistants and regular crowd of the University Chaplaincy, wo were always ready to provide tea, food or sympathy when needed.

Finally, I am extremely grateful to my family and many friends both in Reading and at home for their friendship and support, especially to Maggie and Clive Nunn who let me stay at their house for the last month while I was finishing my thesis, and to Julia Danhof and my parents, Martina and Andreas Schäfer for their unfailing support (as well as proofreading on short notice).

Contents

Chapter 1

Introduction

Clouds can be strikingly beautiful. Be it silvery streaks of cirrus or the towering dark masses of an advancing storm front; fragile wisps of fair-weather cumulus, forever changing, joining and tearing apart; the proverbial silver lining shining at the edges of clouds before the sun or cloud shapes outlined as ragged shadows against the flaming colours of a sunset, they provide dramatic views, painting the sky in complex, evolving shapes of light and shadow. But for anyone working in atmospheric radiation, these same views can be daunting: clouds are a key component of the climate system because they strongly influence the radiative gain and loss of energy that drives atmospheric processes on all scales, from global temperature patterns to microphysical processes (Boucher et al., 2013). Because they so strongly interact with radiation, it is crucial to capture the effect of clouds correctly, but modelling their complex shapes on scales down to individual droplets and their rapid evolution in time exactly is impractical — and on global scales, impossible. How, therefore, can we simplify this complexity enough to be manageable while retaining the relevant information to produce accurate radiation calculations?

Currently, the uncertainty about the radiative effect of clouds, about $\pm 5\,\mathrm{W\,m^{-2}}$ (Stephens et al., 2012), is larger than the total anthropogenic climate change forcing of around $2\,\mathrm{W\,m^{-2}}$ (Myhre et al., 2013), introducing a large uncertainty in climate change predictions. It is therefore an important aim to improve the representation of cloud-radiation interaction in current models in order to increase confidence in the fidelity of their predictions of future climates. In this thesis, we will focus on the impact of 3D cloud-radiation effects due to horizontal radiative transport that are neglected in almost all estimates of global cloud effect on radiation. Numerous studies have shown locally that these effects can be large for individual cloud scenes. We will investigate the global 3D cloud effects on radiative fluxes and heating rates, leaving feedbacks due to atmospheric adjustment for future research.

In this chapter, we will first address our current knowledge of clouds and discuss how they are represented in models in Section 1.1. Our knowledge is based on a range of cloud observations, so we give a short overview about historical and current cloud observations. In Section 1.2 we explain the current methods used in global models to treat radiative transfer in the vertical direction only, and in particular the simplifications of interaction between radiation and clouds in different global radiation schemes. Section 1.3 describes the various 3D effects of horizontal radiative transfer in real cloudy atmospheres that are neglected in the current one-dimensional radiation models. Finally, Section 1.4 presents an outline of the thesis and our approach to quantifying these 3D effects globally.

1.1 Cloud observations and cloud representation in models

There are many ways to observe clouds. The oldest and simplest method is by ground-based human observers who judge cloud type, altitude and coverage based on the clouds' visual appearance from below. Scientific classification of clouds into types by their shape and physical extent, which relate to their dynamics, started in 1802 with a classification scheme designed by L. Howard that, with modifications, is still used today (Stephens, 2003). Climatologies of cloud amount can be compiled from ground-based human observations, although cloud measures might be subjective (Mokhov and Schlesinger, 1994, listed some 20^{th}-century examples and compared them to satellite climatologies). Radiosondes can measure atmospheric conditions like temperature or humidity within clouds, which can then be compared to values in the clear sky, but since they travel up to 100 km horizontally during their ascent, the information they provide on local cloud scenes is limited.

With the deployment of the first meteorological satellites in the 1960s (Kidd et al., 2009), the available quantity of cloud observations increased by orders of magnitude. The early satellites solely photographed or measured visible and infrared radiation, which gives a global overview of total horizontally projected cloud cover over the Earth's surface. Satellite-based climatologies of total cloud amount have been compiled since the late 1960s, and the International Satellite Cloud Climatology Project (ISCCP; Schiffer and Rossow, 1983) has provided a continuous climatology since 1983. Radiation obser-

vations like the Clouds and the Earth's Radiant Energy System (CERES; Wielicki et al., 1996) provide an estimate of cloud radiative impact that can be compared to retrieved cloud properties (e.g. Minnis et al., 2004).

Temperature and hence height of cloud tops can be inferred from infrared measurements, and with certain assumptions about cloud water distribution and radiative transfer, reflectance properties allow an estimate of the average particle size in clouds. Instrument sensitivity and spatial resolution have been much refined since the earliest satellites. The Landsat satellites conduct measurements of visible and infrared radiation at very high spatial resolutions of 15 to 60 m (Roy et al., 2014), although with the drawback that this information is not co-located with other observations. The methods to determine cloud top height, cloud optical properties, water content and particle size have also been improved and incorporate spectrally finely resolved measurements of emitted thermal and reflected solar radiation like those from the MODerate Resolution Imaging Spectroradiometer (MODIS; Justice et al., 1998) on NASA's Aqua and Terra satellites (Platnick et al., 2003). However, since they can only provide horizontally projected cloud cover and cloud top and vertically integrated quantities such as cloud optical depth, these measurements yield little information on the 3D distribution of clouds below cloud top or on cloud internal structure. Vertical position of clouds and cloud fraction at each height are inferred using various assumptions, which lead to some uncertainty and to differences between different retrieval methods (Pincus et al., 2012). Figure 1.1 shows a comparison of annual-mean high, middle and low cloud amount between three different cloud retrievals, as conducted by Pincus et al. (2012). Although large-scale patterns are similar, there are sizeable differences in the different cloud amounts.

In order to understand and model the physical processes within clouds and their crucial interaction with energy and water transport as well as with radiation, more precise estimates of the constituent elements of clouds are required: we need to know as much as possible about the number concentration, size, shape and spatial distribution of the small liquid and ice particles that form a cloud. Samples of particles can be obtained by in-situ measurements from aircraft during observation campaigns (e.g. Albrecht et al., 1995; Boers et al., 1996; Heymsfield et al., 2002), which aid understanding of physical processes and parametrisation development, but they are sparse in time and space. Remote-sensing instruments that can probe into clouds provide the possibility

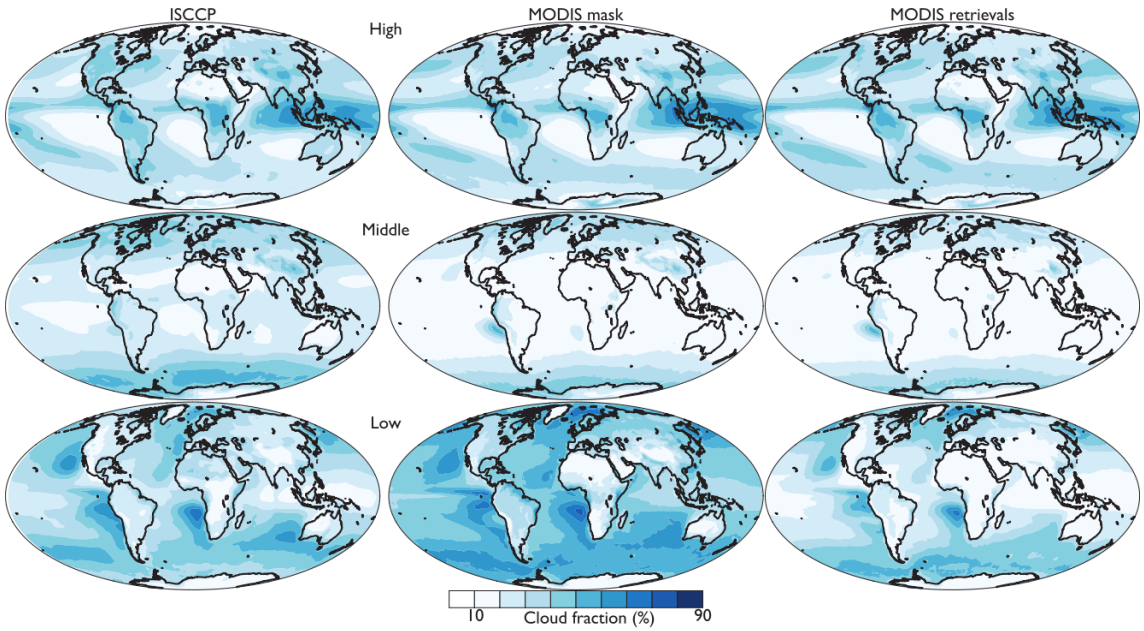

Figure 1.1: Comparison of annual-mean cloud distribution between different satellite retrievals: ISCCP (left-hand column), the MODIS cloud mask (middle column) and the MODIS cloud retrieval (right-hand column). The maps show cloud fraction at various heights: (top) high clouds (pressure $<$ 440 hPa), (middle) middle clouds (440 hPa $<$ pressure $<$ 680 hPa), and (bottom) low clouds (pressure $<$ 680 hPa). Figure from Pincus et al. (2012).

to monitor cloud distributions and internal cloud structure on a more continuous basis. Passive microwave radiometers based either on the ground or on satellites can provide information about total cloud water, and a rough vertical cloud water distribution, although at coarse vertical resolution (Kummerow et al., 1998).

Active radar instruments can probe cloud structure at a much higher resolution. Vertically pointing cloud radars have been deployed in networks like the Atmospheric Radiation Measurement (ARM) project (Stokes and Schwartz, 1994) or the Cloudnet project (Illingworth et al., 2007). If they are equipped with Doppler capabilities, they can also add information on cloud and precipitation particle motion. Combining several radars at different frequencies can yield detailed information on particle size and shape distribution (Kneifel et al., 2011; Stein et al., 2015b). The radar information can be supplemented by lidar measurements to help pinpoint cloud base height, and to detect clouds that are too optically thin to be sensed by the radar, such as high ice clouds, as well as aerosol. A similar combination of instruments from space is possible through combining observations from the CloudSat cloud radar (Stephens et al., 2002) with those from the Cloud-Aerosol Lidar and Infrared Pathfinder Satellite Observation lidar (CALIPSO;

Winker et al., 2003). The forthcoming Earth Clouds, Aerosol and Radiation Explorer satellite (EarthCARE; Illingworth et al., 2015) will combine radar and lidar instruments with improved sensitivity on one platform together with 2D horizontal imager measurements of spectral visible and longwave radiation and measurements of broadband radiative fluxes.

To determine the effects of 3D cloud-radiation interaction in this thesis, we need information on three-dimensional cloud structure. All the observations discussed above have in common that they are in (at most) two dimensions: either 2D imagers that see a horizontal projection of the atmosphere or profiling instruments that see a time-height section. There are two main methods to obtain three-dimensional views of clouds: first, the comparatively new ground-based scanning cloud radars can sample cloud observations in three-dimensional space (Fielding et al., 2013; Kollias et al., 2014a,b). While as yet there are not many of these radars globally, they can provide detailed three-dimensional cloud information at a high spatial resolution of tens of meters to one hundred meters, especially when supplemented with additional information from other instruments (Fielding et al., 2014). The scanning pattern can be varied to yield increased spatial and temporal resolution in particular areas according to the requirements of specific research questions (Fielding et al., 2013).

The other approach is to combine co-located horizontal imager data and vertical profiler data, using the assumption that columns that appear similar in the imager data have similar vertical structure. Hence, to each column in the horizontal image, the same vertical structure is assigned as that of the column in the profiler section whose imager observations are closest. This method has been proposed to obtain 3D cloud retrievals from EarthCARE (Barker et al., 2011) and can already be used on combined CloudSat, CALIPSO and MODIS data. It can thus provide global 3D reconstructions. How realistic these reconstructions are depends on how close to reality the underlying assumption that columns that appear similar in imager measurements have similar vertical structure is, which will need to be closely evaluated, for example by comparison with 3D scanning cloud radar observations. As with satellite observations in general, spatial resolution is also still limited to scales too coarse to show the shape and structure of individual clouds.

Neither of these approaches is far enough developed to provide a good global sampling of high-resolution three-dimensional cloud structure observations at sufficient res-

olution for calculating 3D cloud-radiation interaction to a high level of confidence. This is why studies of 3D cloud-radiation effects have hitherto relied on local case studies based on high-resolution observations where available, or more commonly on high-resolution simulated cloud fields. We will present a method to parametrise the necessary cloud geometry information from globally available cloud variables in Chapter 3, based on a number of high-resolution cloud case studies. This method can be refined in the future as global availability of and confidence in three-dimensional cloud observations continues to develop.

Cloud models have to account both for dynamical movements of air masses that happen on a range of scales from that of fronts at several hundred kilometres to that of turbulent mixing at metres or less and for the microphysical evolution of cloud particles driven by thermodynamic conditions. High-resolution cloud models on limited domains like large-eddy simulations (LES) and cloud-resolving models can resolve dynamical up-and downdrafts and the larger turbulent scales explicitly, and can also represent the spatial inhomogeneity of atmospheric conditions that leads to differential microphysical formation and evolution of cloud particles (e.g. Moeng et al., 1996; Heus et al., 2010). They are, however, much too computationally expensive to use on a global scale, especially in the context of long climate simulations or operational weather forecasts. Operational global weather and climate models address the cloud modelling problem in a highly simplified manner, through bulk cloud water schemes (e.g. Tiedtke, 1993) that only diagnose the total amount of water of each phase per gridbox and vertical layer and how much of the gridbox is covered with cloud (the cloud fraction). Convection is represented using simple mass-flux schemes (e.g. Arakawa and Schubert, 1974).

1.2 Radiation model uncertainties and simplifications

Radiative transfer in the atmosphere is a highly complex problem. Shortwave visible, ultraviolet and near-infrared radiation from the sun enters the atmosphere, some of which is scattered or absorbed by atmospheric gases, aerosol particles and particularly cloud particles, while the remainder reaches the surface to be either absorbed and thereby heat the surface or to be reflected back up into the atmosphere. The Earth's surface as well as all components of the atmosphere (gases, aerosol and cloud particles) also emit, absorb

and to some degree scatter thermal radiation, some of which is radiated out to space, cooling the Earth system. The rate of absorption and scattering by atmospheric particles and the angle of scattering depend primarily on the ratio of the wavelength to the particle size (e.g. Petty, 2006). Interaction of radiation with clouds is especially challenging to capture, due to the complex 3D shapes and high spatial and temporal variability of clouds and their strong influence on radiation. A note on nomenclature: the change in net radiative fluxes due to clouds (determined as radiative fluxes in the presence of clouds minus fluxes in the clear sky at otherwise identical atmospheric conditions) is commonly referred to as both cloud radiative effect (CRE) and cloud radiative forcing (CRF), although it is not really a forcing in the sense of an effect that changes the current climate, but an integral part of the current climatic state. We will use both notations interchangeably in this thesis.

Numerical radiative transfer schemes in weather and climate models have traditionally relied on several assumptions both to simplify the problem in line with the simplified modelling of clouds and to reduce computational cost. They usually treat radiative transport only in the vertical dimension, referred to as the *two-stream approximation*, which drastically reduces the complexity of the radiative transfer problem. Since bulk cloud schemes in these global models usually only provide cloud fraction and cloud water content in each gridbox and layer, without any information on cloud geometry, radiative transfer models have to make geometric assumptions, and have huge freedom in what geometry to assume. In order to treat several vertical layers, models have to incorporate empirical rules on how the clouds in various levels overlap, either explicitly or by dividing the gridbox into sub-columns that represent the various possible cloud configurations. Originally the maximum-random overlap (Morcrette and Fouquart, 1986) was most common, which was later refined based on observational evidence, e.g. into exponential-random overlap taking account of vertical separation by Hogan and Illingworth (2000), or to include the effects of wind shear by Di Giuseppe and Tompkins (2015).

Further assumptions are that the cloudy region of a model gridbox can be treated as horizontally homogeneous, neglecting the horizontal variability observed in real clouds (the plane-parallel assumption) and that it is sufficient to treat vertical radiative fluxes within cloudy and clear regions separately, without including horizontal transport be-

tween them (the 1D, independent pixel or independent column approximation, abbreviated IPA or ICA, e.g. Cahalan et al., 1994b). Although these assumptions are obviously not realistic, until the early 2000s, global models typically used one-dimensional *region-based two-stream schemes* (e.g. Edwards and Slingo, 1996) that divide each model gridbox into one clear and one cloudy region and rely on both the two-stream approximation and the plane-parallel assumption (e.g. Meador and Weaver, 1980).

The plane-parallel assumption is not realistic even for stratiform clouds, due to in-cloud variability. Because optical properties such as longwave emissivity and shortwave albedo depend on cloud water content in a non-linear manner, values calculated from the mean water content (according to the homogeneity assumption) are biased with respect to the actual average values. This effect was discussed by Harshvardhan and Randall (1985) and Stephens (1985). A wide range of observations have since quantified the water-content variability in clouds, as reviewed by Shonk et al. (2010). This problem has been addressed by the development of fast radiation schemes able to treat cloud horizontal structure, at first by weighted averaging of cloud optical properties (Oreopoulos and Barker, 1999). The Monte Carlo Independent Column Approximation (McICA; Pincus et al., 2003) allowed a more rigorous account of in-cloud inhomogeneity by representing horizontal cloud variability and vertical overlap through stochastically generated sub-columns and used the ICA assumption to treat radiative transfer in each sub-column separately with a one-dimensional two-stream calculation. The adaption of McICA schemes for global models was achieved by spreading the required computations at different wavelengths over the sub-columns. This method is now widely used in large-scale models. Another way of including in-cloud inhomogeneity is the Tripleclouds method of Shonk and Hogan (2008), which separates the cloud in each gridbox into an optically thick and an optically thin sub-region. McICA schemes are faster than the Tripleclouds method, and are unbiased compared to other ICA calculations, but contain some noise due to the random distribution of spectral intervals over the sub-columns.

Estimates of the biases in traditional region-based two-stream schemes by comparing to new schemes that include cloud inhomogeneity have established that neglect of in-cloud horizontal structure results in an overestimation of the magnitude of the net longwave plus shortwave cloud radiative effect (CRE) at top-of-atmosphere (TOA) by around 14% globally (Shonk and Hogan, 2010). Both the McICA and Tripleclouds

methods keep the radiation calculation one-dimensional according to the ICA assumption, not allowing radiation to travel horizontally. This would be justified for emission or isotropic scattering if the clouds were actually homogeneous and large enough that cloud edges play a negligible role, as radiative fluxes in opposite horizontal directions at any point would be equal, and hence net horizontal fluxes would vanish, but real clouds often have comparable horizontal and vertical extent. The ICA assumption that horizontal transport between columns is negligible compared to vertical transport actually becomes less realistic when the cloud is divided into smaller in-cloud sub-columns with a higher vertical-to-horizontal aspect ratio.

In the shortwave spectral region, neglecting 3D effects as per the ICA assumption causes an error in CRE at TOA of between -25% and $+100\%$ (depending on solar zenith angle) in individual scenes of strongly non-plane-parallel clouds such as cumulus, contrails or deep convection (Benner and Evans, 2001; Di Giuseppe and Tompkins, 2003b; Gounou and Hogan, 2007), but considerably less for stratocumulus and cirrus (Zuidema and Evans, 1998; Zhong et al., 2008). Barker et al. (2003) evaluated shortwave albedo and heating rate calculations of 25 one-dimensional radiation models used in leading general circulation models (GCMs) of the time (both ICA models and region-based models with different cloud overlap assumptions) against the results of four fully 3D Monte Carlo models for four cases of realistic stratocumulus and convective clouds. They also calculated 3D Monte Carlo benchmarks using the cloud geometry assumptions of each class of 1D models. For (nearly) overcast sky, all region-based two-stream models systematically overestimated albedo, presumably due to the non-linear dependence on optical depth discussed above, while ICA models agreed closely with 3D benchmarks. Albedo was also always overestimated by models using random overlap, which produces higher-than-realistic total cloud cover. In cases with partial cloudiness and more horizontal structure, 1D models (and also the benchmarks for 1D model classes) using overlap assumptions other than random overlap were found to underestimate cloud albedo for overhead sun, and overestimate cloud albedo for low sun (see Figure 1.2 for one typical case study from Barker et al., 2003). On average, the ICA benchmarks were closest to the 3D Monte Carlo results, although the errors due to neglecting 3D effects were still large. Two-stream models using the exact cloud overlap tended to overestimate cloud albedo for most solar zenith angles, while for non-overcast cloud scenes two-stream schemes

with maximum-random overlap were closer to the 3D results or underestimated them (which might be due to compensating errors). The spread of 1D models in each class was generally large, up to ± 0.1 in albedo.

For longwave radiation, much less work has been done and longwave 3D effects are often assumed to be negligible. However, studies have estimated that 3D effects increase longwave surface CRE by 30% for cumulus (Heidinger and Cox, 1996) and both TOA and surface longwave CRE by 10% for aircraft contrails (Gounou and Hogan, 2007). Takara

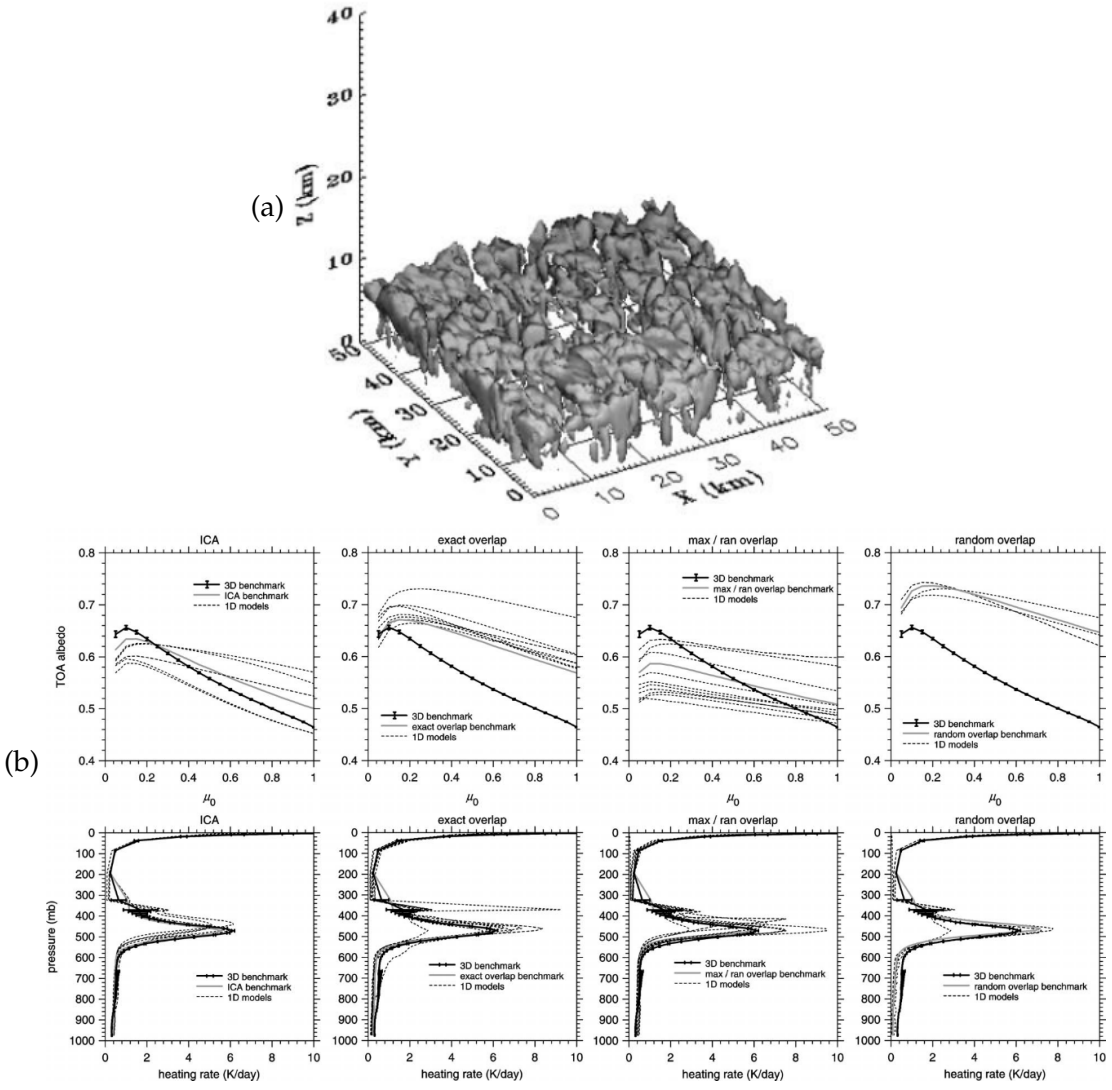

Figure 1.2: (a) 3D representation of open cell cloud case. (b) Comparison of broadband shortwave albedo at TOA and heating rate results for the open cell cloud case with 3D Monte Carlo benchmarks, by model type, plotted against the cosine of solar zenith angle μ_0. The left-hand column shows the results of ICA models, the other three columns those of region-based models using different overlap assumptions. Benchmark calculations for each model type are also shown. Both figures from Barker et al. (2003).

and Ellingson (2000) have reported surface longwave flux errors of up to $10\,\mathrm{W\,m^{-2}}$ due to neglecting both 3D effects and longwave scattering. It should be noted that 3D longwave effects are largest at the surface, because their strongest contributions come from optically thick broken clouds like cumulus that occur low in the atmosphere. Kablick III et al. (2011) found errors in net longwave flux within cloud layers of $2-3\,\mathrm{W\,m^{-2}}$ for an ICA model using sub-columns and up to $20\,\mathrm{W\,m^{-2}}$ for a maximum-random overlap two-stream scheme with one clear and cloudy region each, decreasing above the clouds.

On regional and global scales, such estimates of 3D effects are harder to conduct, both because of the lack of global high-resolution 3D observations to use as input and because even if global 3D cloud fields were available, any fully 3D calculations to compare against would be prohibitively numerically expensive. Randall et al. (2003) suggested embedding a cloud-resolving model in a large-scale model to overcome the lack of 3D cloud structure information, an approach referred to as "superparametrisation". Using this approach and a two-dimensional radiative transfer model, Cole et al. (2005) estimated a change in zonally averaged shortwave CRE between 2D and 1D calculations of -5 to $+5\ \mathrm{W\,m^{-2}}$ in the shortwave, depending on latitude, and an increase of less than $1\,\mathrm{W\,m^{-2}}$ in the longwave in 2D. Zonal mean changes are generally smaller than local changes. The use of 2D calculations, which neglect one dimension of horizontal radiative transfer, and the coarse spatial resolution of 4 km, which neglects some of the cloud structure, could also have led to an underestimation of the effects of horizontal radiative transfer. Barker et al. (2015) studied horizontal radiative transfer effects in 3×10^5 globally distributed cloud scenes observed using CloudSat and CALIPSO, again using 2D calculations and at a resolution of 1 km, and estimated shortwave broadband errors due to neglected 3D effects of around -5 to $+5\ \mathrm{W\,m^{-2}}$ (depending on solar zenith angle). Pincus et al. (2005) estimated that 3D effects from cumulus clouds calculated in 2D rather than 3D were underestimated by around 30%. Recently, Barker et al. (2016) have proposed using 3D stochastically generated cloud fields (based on available cloud information) and fully 3D Monte Carlo models with reduced photon number for truly 3D global calculations. However, in spite of the lowered photon numbers, this approach remains highly computationally expensive, and has therefore not yet been used for a global estimate of 3D effects.

1.3 Mechanisms of 3D cloud-radiation effects

Differences between realistic 3D radiation and 1D models are caused by several horizontal radiative transport effects, both of cloud sides and internal transport in regions, and can partially compensate each other. Horizontal radiative transport effects have previously been classified in different ways by Várnai and Davies (1999) and Hogan and Shonk (2013). The first three effects we consider here were also treated by Hogan and Shonk (2013). Figure 1.3 depicts the various effects schematically. Cloud side effects are neglected in all 1D models, while in-region horizontal transport is approximately represented in region-based two-stream schemes, but not in ICA schemes.

- Shortwave cloud side illumination and cloud side leakage (shown in Figure 1.3 a and b)

  For solar shortwave radiation, there are two ways that radiation can interact with cloud sides, which have opposite effects on the fluxes. First, solar radiation can be intercepted by cloud sides as well as cloud tops (as seen in Figure 1.3 a). This effect is most relevant when the sun is low in the sky. It increases the amount of radiation that is intercepted and reflected or absorbed and therefore increases effective cloud cover, leading to higher cloud reflectance, higher shortwave atmospheric heating rates and less downwelling shortwave radiation below the cloud.

  On the other hand, radiation in the cloud (both direct and scattered) can also leak out of cloud sides (shown in Figure 1.3 b). This leakage increases the amount of radiation that passes through the cloud instead of being scattered or absorbed, and thereby increases downwelling flux below the cloud and decreases cloud reflectance and atmospheric heating. It is most relevant for high sun.

  Which of these two complementary effects is dominant, and therefore the sign of the shortwave *3D cloud side effect* (the sum of these two effects) depends on the solar zenith angle (SZA). For high sun, cloud side leakage dominates, leading to lower cloud reflectance and less negative cloud radiative effect in 3D compared to 1D calculations. If the sun is low, however, cloud side illumination is the stronger effect, increasing cloud reflectance and strengthening the negative CRF compared to 1D schemes. When considering integrated results over time intervals of a day or more, the effect of cloud side illumination dominates, as will be seen in our year-

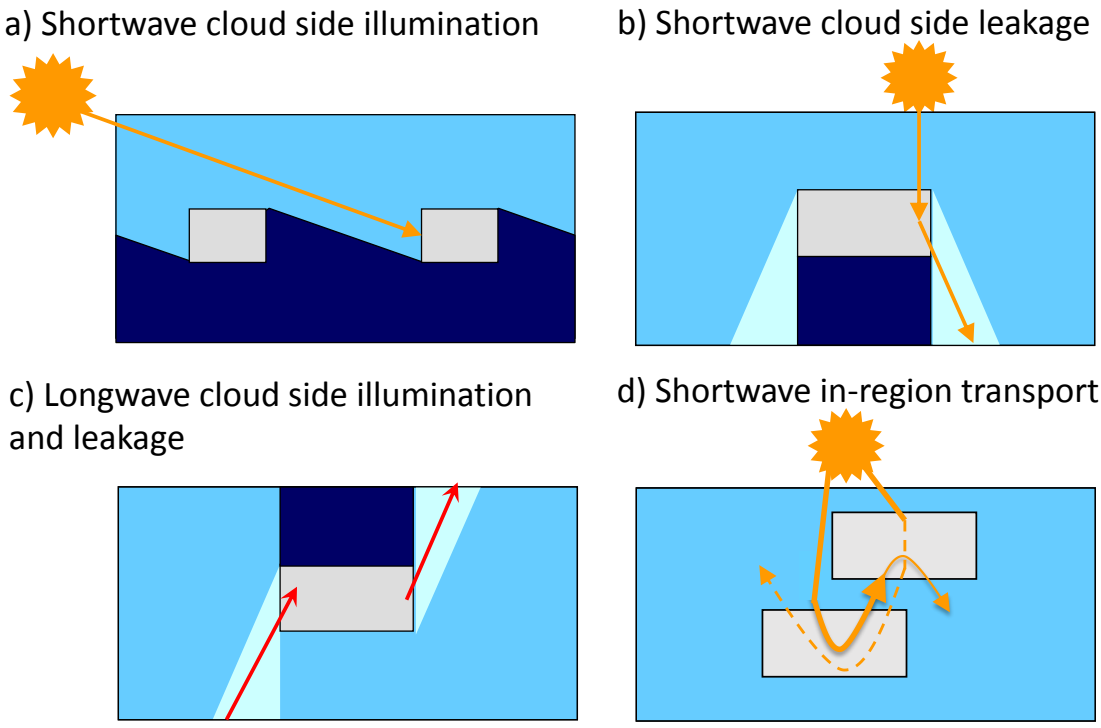

Figure 1.3: 3D effects in reality that are not considered in ICA calculations: (a) Shortwave cloud side illumination. This effect increases shortwave cloud reflectance, and decreases downwelling flux below the cloud. (b) Shortwave cloud side leakage. This effect decreases shortwave cloud reflectance, and increases downwelling flux below the cloud. (c) Longwave cloud side illumination and cloud side leakage. These effects increase the total longwave cloud effect by increasing both cloud absorption and cloud emission. The result is to increase downwelling flux below the cloud and decrease upwelling flux above the cloud (since clouds are usually cooler than the surface and emit less longwave radiation than they absorb). (d) Shortwave horizontal in-region transport. This effect increases the fraction of reflected radiation that reaches higher cloud layers instead of clear sky. Since the chance of further scattering or absorption is higher within the cloud, the effect reduces the amount of reflected radiation reaching TOA and increases downwelling flux below the cloud and atmospheric heating. Panels a) and b) adapted from Hogan and Shonk (2013).

long global experiments in Chapter 4. This is because this effect applies to a longer part of the diurnal cycle. The overall result is a negative 3D cloud side effect on net downwelling shortwave radiation.

- Longwave cloud side illumination and cloud side leakage (shown in Figure 1.3 c) In the longwave, the 3D effect of cloud sides is to allow both additional interception by the cloud of fluxes emitted by the surface or atmosphere below and additional cloud emission through cloud sides. Hence, the total effect of the cloud increases (similar to the effect of increasing cloud cover slightly). The cloud effect in the

longwave is to intercept and decrease upwelling flux from the surface or atmosphere below, while also emitting longwave radiation both upwards and downwards. Since the clouds are typically cooler than the surface, they emit less thermal radiation, and therefore upward emission from the cloud is lower than their absorption of upwelling radiation from the surface. Hence the clouds cause a decrease in upwelling longwave flux above, while cloud emission strongly increases downwelling longwave flux below the clouds, generally warming the Earth. This effect is enhanced when cloud side effects are included.

- Shortwave horizontal in-region transport (shown in Figure 1.3 d)
  This effect was not considered by Hogan and Shonk (2013), but we find in this thesis that it is at least as important as the other two shortwave effects. While the two previous effects were caused by interaction of radiation with cloud sides, this effect is due to internal horizontal transport in each region. Essentially, in-region horizontal transport has an effect on total gridbox fluxes because regions are not exactly vertically overlapped between different vertical layers and in-region transport can lead to radiation being reflected into a different region in layers above than it passed through on the way down. The situation in which the effect is strongest is when shortwave radiation travels downwards through the clear sky until it reaches one particular cloud layer, and is then reflected up into a higher cloud layer instead of into the clear sky. The chance that the radiation is subsequently scattered again or absorbed is much stronger within the higher cloud than in the clear sky, so this effect decreases the amount of reflected radiation that reaches TOA. While analogous transport also occurs for radiation that has travelled through other cloud layers before reaching a particular layer (which can be reflected up into the clear sky, as shown by the dashed arrow in Figure 1.3 d), and for diffuse up-and downwelling fluxes, all of these fluxes are much weaker than direct flux that reaches the cloud layer in question through the clear sky. Therefore the reduction in upward reflectance of direct solar radiation is dominant, and the total effect of in-region horizontal transport is to decrease shortwave cloud reflectance and thereby decrease the negative shortwave CRF, while increasing shortwave atmospheric heating and downwelling flux below the clouds. Other than for shortwave 3D cloud side effects, the sign of the in-region horizontal transport effect does not depend

on the position of the sun, so the effect does not compensate over the course of the day.

Since the effect of horizontal in-region transport is due to different illumination of the parts of the cloudy region that lie beneath other clouds and beneath clear sky and to multiple scattering, it is much less relevant in the longwave, where direct solar illumination is negligible, the dominant source of in-cloud flux is internal emission that does not depend on layers above or below, absorption is stronger and multiple scattering much less significant.

The horizontal in-region transport effect is neglected by models that use cloudy sub-columns together with the ICA assumption to represent cloud overlap since radiative transport between sub-columns with different overlap configurations is impossible in these models. However, since region-based 1D two-stream radiation schemes assume homogeneous radiative fluxes within each region and layer, they actually represent this effect unless the solver is particularly adapted to avoid in-region horizontal transport. Shonk and Hogan (2008) considered ICA as the truth and hence treated in-region horizontal transport as an error, which they termed "anomalous horizontal transport", and developed a method for largely removing the effect in their shortwave solution to the radiative transfer equations. However, although complete homogenisation of radiative fluxes in each region is probably an overestimation, some in-region horizontal transport is in fact a realistic effect. This implies that neglect of horizontal in-region transport causes an overestimation of cloud reflectivity in ICA models like McICA compared to region-based two-stream models, which is somewhat ironic since part of the motivation for the widespread adoption of McICA models was to overcome the high-reflectivity bias due to neglect of in-cloud inhomogeneity in region-based models. We will test this hypothesis in our experiments in Chapter 4.

The 3D effects of cloud side transport and in-region transport can influence each other, since interception of radiation by the sides of higher clouds due to 3D cloud side effects can lead to shadowing of lower clouds, reducing the incident radiation on the lower clouds and therefore the amount of the in-region transport effect.

While high-resolution 3D radiation models are capable of calculating the precise radiative effect of a known 3D cloud field (e.g. Cahalan et al., 2005; Pincus and Evans, 2009;

Mayer, 2009), they are not suitable for climate models because of their high computation cost. Killen and Ellingson (1994) and Heidinger and Cox (1996) proposed simple scaling of the cloud fraction as an empirical approximation to account for longwave 3D effects, but that method is too crude for general cloud fields, especially with multiple cloud layers. Consistency with 3D cloud effects in the shortwave is also hard to achieve, as any equivalent shortwave method would only hold for one particular solar zenith angle. We seek a more sophisticated method that is physically consistent between spectral regions and valid for general cloud fields. Recently, fast approximations for 3D radiative transfer on cloud resolving scales have been developed (Klinger and Mayer, 2016; Jakub and Mayer, 2015), but these approaches are not designed for use in global models.

1.4 Research in this thesis

In order to obtain a global estimate of the importance of 3D cloud-radiation effects, there are two key ingredients we need: a radiation scheme that is efficient enough for global calculations and represents these 3D cloud effects to sufficient precision, and information on the 3D structure of clouds to provide to the radiation scheme. As detailed above, neither of these required components is easily available as yet, so we need to develop our own methods.

Hogan and Shonk (2013) presented an outline for a method that includes 3D cloud side effects in a two-stream scheme in the shortwave. Based on their work, we develop the idea into a complete radiation scheme (called SPeedy Algorithm for Radiative TrAnsfer through CloUd Sides or SPARTACUS), suitable for global calculations. This entails deriving a longwave treatment that incorporates parametrisation of geometrical effects that are relevant in the longwave (some of which could be neglected in the shortwave) and evaluating the scheme for realistic clouds. The development of the longwave component and evaluation of SPARTACUS are described in Chapter 2.

Algorithm development is intertwined with the determination of the most appropriate cloud geometry input for the scheme, since the cloud geometry information that is necessary depends on the nature of the parametrisations. So, after completing development of the radiation scheme and deciding what cloud geometry information is needed, the next question is how to provide the necessary input. Our approach is to de-

velop a simple description of cloud scene geometry that consists of only two parameters in each cloud level, one that measures the amount of cloud edge length in a domain, and one that describes cloud horizontal spacing. While no global well-evaluated high-resolution 3D cloud observations are currently available, there are many local studies of cloud structure based on a variety of observations as well as high-resolution cloud simulations. However, many cloud structure investigations use methodology and geometry variables that are not related to the length of cloud edges, which is what radiative transfer in our scheme is sensitive to, and hence are of limited use. Therefore, we conduct our own cloud geometry analysis on a number of high-resolution 3D case studies of various cloud types, both simulated and observed with a scanning cloud radar. To build a broader picture, we also consider values found in the few available studies that consider similar cloud geometry variables, and re-analyse some of the data used in the literature. This analysis is discussed in Chapter 3, where we first derive the best variables to capture the crucial pieces of information and then use the case studies to determine typical values of the cloud geometry variables, and how they depend on the type, amount and location of the clouds and on the meteorological conditions. Understanding these dependences allows us to estimate the cloud geometry variables we need from cloud information that *is* available in observations and models on a global scale.

Having thus acquired both an efficient enough radiation model and a method to estimate the necessary cloud geometry input globally, we can embark on a set of global experiments to determine the impact of 3D cloud-radiation effects, described in Chapter 4. Our experiments are offline calculations that isolate 3D cloud-radiation effects without considering feedbacks due to atmospheric adjustment to the change in fluxes and heating rates. We use a whole year (2001) of ERA-Interim atmospheric data as a basis for our experiments, and conduct 3D calculations with a range of cloud geometry inputs as well as two sets of 1D experiments that include and exclude different 3D effects. This allows us not only to estimate the total 3D cloud impact on radiative fluxes and heating rates in both the longwave, shortwave and in total, but also to separate the impact of each 3D effect, and to determine the spatial and annual distribution of these effects and their dependence on cloud geometry. We can hence provide a detailed answer to the question of what impact 3D cloud-radiation effects have globally.

Chapter 2

SPARTACUS model development

2.1 Introduction

The lack of a fast broadband radiative transfer scheme that can reliably represent 3D effects in large-scale models means that we currently have no way to estimate the impact of 3D radiative transfer on the Earth's radiation budget or on the evolution of weather systems. As a first step to tackling this issue, Hogan and Shonk (2013) proposed a method to incorporate 3D effects into a conventional two-stream radiative transfer code. Their approach described 3D cloud structure information in terms of cloud side area, and added terms to the two-stream equations to represent the loss and gain of radiation through cloud sides, with a modest increase in computational cost. The assumption underlying this formulation is that the fraction of clear-sky flux that encounters a cloud edge is proportional to the length of cloud edge, which roughly corresponds to assuming a random horizontal distribution of clouds within a gridbox. Thus, the cloud edge length versus height, which may be expressed in terms of an effective cloud size (Jensen et al., 2008), is the only input that is needed in addition to the large-scale information on cloud fraction and water content provided in global models. However, Hogan and Shonk (2013) only considered monochromatic calculations in the shortwave part of the spectrum, they neglected in-cloud horizontal inhomogeneity, and their method for solving the modified two-stream equations was excessively complicated, with multiple steps that still resulted in numerical imprecisions and a dependence on vertical resolution.

Here, we describe the development of a broadband radiation scheme ready for use in large-scale models, which overcomes the limitations of Hogan and Shonk (2013). We refer to it as the SPeedy Algorithm for Radiative TrAnsfer through CloUd Sides (SPARTACUS). We develop the longwave capability of SPARTACUS making use of fully 3D calculations to identify the most important features to represent, as well as introducing improvements that are applicable in both the shortwave and the longwave. Section 2.2

describes the idealised case of an isolated, isothermal, cubic cloud, which is a very useful benchmark for longwave 3D radiation schemes because its known symmetry properties allow us to determine the 3D effect analytically. In Section 2.3, we outline the SPARTACUS scheme and use the results of Section 2.2 to develop a consistent longwave capability. Sections 2.2 and 2.3 were published in Schäfer et al. (2016).

As part of the model development we correct inconsistencies in the treatment of horizontal and vertical fluxes by Hogan and Shonk (2013). The theoretical basis for these improvements is described in Section 2.3 and in Schäfer et al. (2016), while the practical implementation in a large-scale model and evaluation for realistic cases was performed by Hogan et al. (2016). We summarise their implementation and evaluation of SPARTACUS in Section 2.4, as it forms the basis of the radiative transfer scheme we will use for our global experiments in Chapter 4. Hogan et al. (2016) incorporated treatment of cloud inhomogeneity using the Tripleclouds method of Shonk and Hogan (2008) and evaluated SPARTACUS against fully 3D broadband radiative transfer calculations. Apart from 3D radiative transfer through cloud sides which SPARTACUS explicitly resolves, another 3D cloud-radiation effect that can be important (mostly in the shortwave) is horizontal transfer within each region. In Section 1.3 we have discussed the physical mechanism behind this effect and how it is implicitly treated by different 1D and 3D radiation schemes. Section 2.5 summarises our development of the SPARTACUS scheme for use in global experiments.

2.2 Theory for an idealised cubic cloud

In this section, we examine the idealised case of one homogeneous, isothermal, cubic cloud in vacuum that is isolated in a larger model gridbox of surface area A without other clouds (so cloud fraction c is small). In this symmetric case, the 3D effects can be derived analytically, providing an excellent benchmark for 3D radiation schemes (both fully 3D schemes and approximate schemes such as SPARTACUS). As we are interested in the cloud longwave effect, we here consider only thermal radiation emitted from the cloud, without direct solar radiation or emission, reflection or absorption by the ground. More realistic cases including atmospheric and surface emission, absorption and reflection were considered by Hogan et al. (2016).

All properties of a homogeneous, isothermal cubic cloud are symmetric with respect to discrete rotations that exchange the faces of the cube, and therefore so is the radiation emitted at each face. This means that the outward flux through each cloud face is the same, G, shown schematically in Fig. 2.1. Here, "outward flux" is defined as the radiation through a plane parallel to the cloud face, per unit area of the face (we denote fluxes per area of the cloud by G and fluxes per horizontal area of the domain by F).

We can derive the theoretical cloud 3D effect by comparing the different contributions to the total downward flux $F^{\downarrow}$ through a *horizontal* plane, *per unit area of the entire gridbox* (note difference in definition of flux). The fraction of G through a cloud face that contributes to downward flux depends on the orientation of the face. At cloud base, outward is the same as downward, so $F^{\downarrow}_{\text{base}} = cG$, where the cloud fraction $c = A_{\text{base}}/A$ accounts for the difference between flux per area of cloud base A_{base} and flux per total gridbox area A. At a cloud side, on the other hand, radiation can leave the cloud at an upward or a downward angle with equal probability. Therefore half of the radiation from each cloud side contributes to the downward flux: $F^{\downarrow}_{\text{side}} = \frac{1}{2}GA_{\text{side}}/A$, and since $A_{\text{side}} = A_{\text{base}}$, this becomes $F^{\downarrow}_{\text{side}} = cG/2$.

Adding the fluxes from cloud base and the four cloud sides gives

$$F^{\downarrow}_{\text{base+sides}} = F^{\downarrow}_{\text{base}} + 4F^{\downarrow}_{\text{side}} = 3cG, \tag{2.1}$$

As a measure of the 3D cloud side effect, we introduce the cloud side factor $f_{\text{sides}} = F^{\downarrow}_{\text{base+sides}}/F^{\downarrow}_{\text{base}}$. If the cloud is in a vacuum and there is no interaction with the ground, then from (2.1) we see that $f_{\text{sides}} = 3$ at all heights beneath the cloud.

This result gives an idea of the importance of 3D cloud side effects: two-thirds of the downwelling radiation from the cloud comes from the cloud sides, not the cloud base. The theory is independent of the optical depth of the cloud or the particle scattering properties, allowing the following general statement:

Theorem 1 *For an isolated, isothermal, homogeneous cubic cloud in vacuum above a non-reflecting, non-emitting surface, a third of the downwelling radiation beneath the cloud originates from the cloud base and two thirds from the cloud sides, regardless of the optical depth or scattering properties of the cloud. The same holds for upwelling emitted radiation above the cloud: one third originates from cloud top and two thirds from cloud sides.*

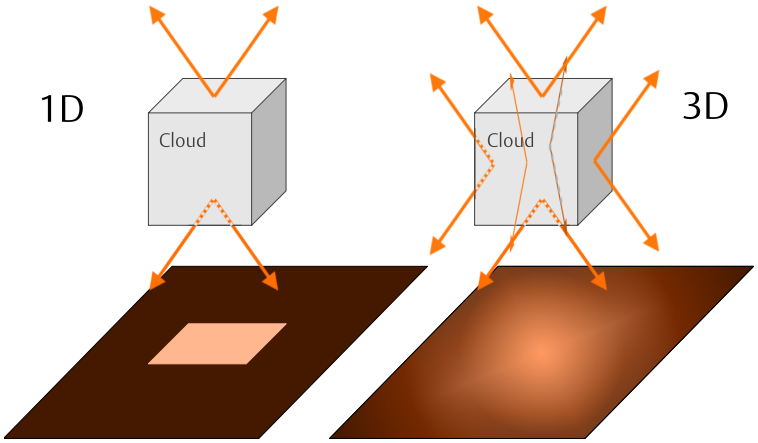

Figure 2.1: Schematic of outgoing fluxes and their contributions to total downwelling flux in 1D and 3D schemes for a cubic cloud. Because of symmetry, the total outward flux G through every cloud face is the same. Every arrow symbolises a flux of $G/2$ through the respective face. At cloud sides, half of the outgoing radiation is at an upward angle, the other half at a downward angle. The distribution of downwelling flux at the surface is shown below: in a 1D scheme, we only see downwelling flux directly underneath the cloud, while in a 3D scheme, cloud side fluxes result in a more spread-out distribution as well as in higher total downwelling flux.

In realistic cases with gaseous absorption and emission, the cloud side factor could be defined as the ratio of *cloud radiative effect* resulting from outgoing fluxes through all faces to that from outgoing fluxes through cloud top and base alone. In these cases, the factor is likely to be somewhat less, partly due to increased gaseous absorption on the longer slanted paths to the ground for radiation from cloud sides, but as we will show, the 3D effect should not be neglected, and always leads to an *increase* in cloud radiative effect, in contrast to the shortwave case, where it can be of either sign.

While the cloud side factor measures the importance of cloud side emission, we are particularly interested in the change in cloud radiative effect relative to the results of current 1D schemes of the type used in weather and climate models. Figure 2.2 shows how radiation encountering cloud sides is treated in 3D and 1D schemes. In 1D schemes, periodic boundary conditions at region boundaries let radiation that encounters a cloud side re-enter at the opposite side and remain within the cloudy region (this is shown schematically in Figure 2.2 as a numerical sink and a numerical source that lets the radiation re-enter the cloud at the opposite side).

For very optically thin clouds (optical depth $\tau \ll 1$), where the chance of absorption or backscattering (scattering from the downward to the upward direction or vice versa) is small; radiation once emitted is essentially unaffected by its passage through the cloud.

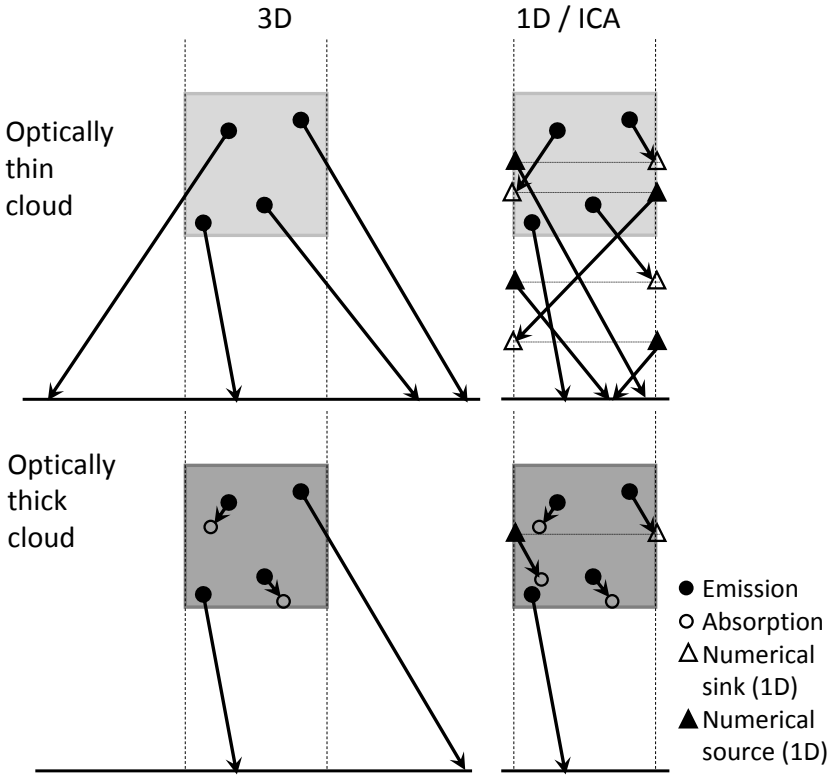

Figure 2.2: Schematic showing the treatment of downwelling radiation encountering cloud sides in 3D and 1D schemes, in the limit of (top row) optically thin and (bottom row) optically thick clouds, for fully 3D radiative transfer (in the left column) and the 1D Independent Column Approximation (ICA; in the right column). In the ICA, cloudy columns have periodic boundary conditions, so that radiation that encounters the side of the column re-enters on the opposite side (shown as numerical sinks and sources in the plot). This makes the radiation's path through the cloud longer than in reality. In the optically thick case increased absorption along the longer ICA path is noticeable, which leads to an underestimation of downwelling flux below the cloud.

Total downwelling flux in the gridbox at any height only depends on the number of emitting cloud particles above. Hence, as using 1D periodic cloud-boundary conditions does not change particle emission, the total downwelling flux in the gridbox beneath the cloud as predicted by a 1D scheme $F^{\downarrow}_{\mathrm{1D}}$ approaches the correct 3D value $F^{\downarrow}_{\mathrm{base\,+\,sides}}$. The spatial distribution of fluxes, however, is different: in reality some radiation leaves the cloudy column and reaches the surface at some horizontal distance from the cloud, but still contributes to the gridbox total of downwelling flux from the cloud. In the 1D calculation this radiation is instead added to the downward flux directly underneath the cloud, which is thereby increased above its real value (as illustrated in Fig. 2.1).

For very optically thick clouds ($\tau \gg 1$), the picture is different. Again, radiation that in reality would escape through cloud sides remains within the cloud in the 1D scheme,

but because of the high optical depth virtually all of it is absorbed or scattered rather than reaching cloud base (see Fig. 2.2). The downwelling flux beneath the cloud $F^{\downarrow}_{1D}$ is approximately equal to the flux out of cloud base in the 3D case $F^{\downarrow}_{base}$, which, as stated above, is lower by a factor of 3 than the correct total downwelling flux. This gives us a limiting benchmark for the underestimation of cloud radiative effects by 1D schemes:

Theorem 2 *For an isolated, isothermal, homogeneous and very optically thick cubic cloud in vacuum above a non-reflecting, non-emitting surface, the downwelling radiation beneath the cloud and upwelling radiation above the cloud are underestimated by a factor of 3 in 1D radiation schemes.*

The factor $f_{1D\,\mathrm{correction}} = F^{\downarrow}_{3D}/F^{\downarrow}_{1D}$ quantifies this error for different cloud cases, but note that $f_{1D\,\mathrm{correction}}$ is only equal to f_{sides} for very optically thick clouds.

2.3 Development of a longwave capability for SPARTACUS

2.3.1 Overview of SPARTACUS

The SPARTACUS scheme modifies the two-stream equations to incorporate horizontal radiative transfer effects by coupling the equations for neighbouring clear and cloudy regions (denoted a and b respectively) through the addition of horizontal transfer gain and loss terms. The cloudy region may optionally be divided into two (denoted b and c) to represent cloud horizontal inhomogeneity following the approach of Shonk and Hogan (2008). The two-region case (clear and cloudy) results in the following equations for up- and downwelling diffuse fluxes $F^{\uparrow}, F^{\downarrow}$ in any individual longwave or shortwave spectral band:

$$\begin{aligned}
\frac{dF^{\downarrow}_a}{dz} &= \beta_a\big(-\gamma_{1,a}F^{\downarrow}_a + \gamma_{2,a}F^{\uparrow}_a + S^{\downarrow}_a\big) \\
&\quad -f_{ab}\varepsilon_a F^{\downarrow}_a + f_{ba}\varepsilon_b F^{\downarrow}_b; \\
-\frac{dF^{\uparrow}_a}{dz} &= \beta_a\big(-\gamma_{1,a}F^{\uparrow}_a + \gamma_{2,a}F^{\downarrow}_a + S^{\uparrow}_a\big) \\
&\quad -f_{ab}\varepsilon_a F^{\uparrow}_a + f_{ba}\varepsilon_b F^{\uparrow}_b;
\end{aligned}$$

$$\begin{aligned}\frac{dF_b^{\downarrow}}{dz} &= \beta_b\big(-\gamma_{1,b}F_b^{\downarrow}+\gamma_{2,b}F_b^{\uparrow}+S_b^{\downarrow}\big)\\ &\quad -f_{ba}\varepsilon_b F_b^{\downarrow}+f_{ab}\varepsilon_a F_a^{\downarrow};\\ -\frac{dF_b^{\uparrow}}{dz} &= \beta_b\big(-\gamma_{1,b}F_b^{\uparrow}+\gamma_{2,b}F_b^{\downarrow}+S_b^{\uparrow}\big)\\ &\quad -f_{ba}\varepsilon_b F_b^{\uparrow}+f_{ab}\varepsilon_a F_a^{\uparrow}.\end{aligned} \tag{2.2}$$

which is analogous to the formalism for diffuse shortwave fluxes in Hogan and Shonk (2013), Equation (11) except for the factors ε that describe spatial distribution of emitted radiation within each region (see below).

Here, the fluxes are radiative power per area of the entire gridbox (in $\mathrm{W\,m^{-2}}$), z is height increasing downward and β is the volume extinction coefficient. The coefficients γ_1 and γ_2 govern extinction by absorption and backscattering, and gain by backscattering respectively, and are given in Equations (12) and (13) of Hogan and Shonk (2013), and elsewhere. There is non-negligible scattering in the longwave (for the droplet size seen in typical cumulus clouds and a wavelength in the atmospheric window region, the single scattering albedo ω is 0.6), which we include in our model. The source terms $S^{\downarrow\uparrow}$ are the internal sources of diffuse radiation in each region. In the shortwave this would be scattering from the direct solar beam, while in the longwave it represents isotropic thermal emission. For region a the longwave source terms are given by

$$S_a^{\downarrow}(z) = S_a^{\uparrow}(z) = c_a\frac{\pi(1-\omega_a)}{\cos\theta_1}B[T(z)],$$

where c_a is the fraction of the domain covered by region a, B is the Planck function, $T(z)$ the temperature at a given height and ω_a is the single scattering albedo (and similarly for regions b and c). For optimum longwave results in atmospheres dominated by gas absorption, we assume the zenith angle of diffuse streams, θ_1, to be 53° (Elsasser, 1942; Fu et al., 1997), although other assumptions are possible. Note that θ_1 also appears in the definitions of γ_1 and γ_2.

The system of differential equations in (2.2) can be solved for the entire multi-layer atmosphere by formulating the terms as vectors and matrices and computing the solution in terms of matrix exponentials, as described in detail in Sections 2 and 3 of Hogan et al. (2016). This approach is more elegant and accurate than the multi-stage method proposed by Hogan and Shonk (2013).

The final two terms on the right-hand-side of each of the expressions in (2.2) represent lateral transport between regions. For example, $f_{ba}\varepsilon_b F_b^{\downarrow}$ is the rate of transport of downwelling radiation from region b (cloud) to region a (clear sky), per unit vertical distance. Naturally, this term is proportional to $F_b^{\downarrow}$, the horizontal-mean flux at a particular height within the cloud. The two coefficients describe the distinct physical processes that determine this rate.

The first coefficient, f_{ab} or f_{ba}, is purely a function of the geometry of the cloud side. It is a measure of the cloud side area, which in vertically homogeneous model layers is equivalent to the product of the layer depth Δ_z and the length of cloud edge in the layer. Hogan and Shonk (2013) showed that f_{ab} may be formulated at a given height in terms of the total length of cloud edge per unit area of the gridbox. However, applying their theory to the idealised cubic cloud described in Section 2.2 reveals an error, which we address in Section 2.3.2. The second coefficient, ε_b, accounts for any systematic difference between the mean fluxes in the cloudy region and fluxes near cloud edge (which determine outgoing fluxes at cloud edge). We choose the symbol ε as this coefficient plays the role of a kind of effective emissivity of the cloud edge. In the shortwave, we find that $\varepsilon_b \simeq 1$ (as assumed by Hogan and Shonk (2013)) works reasonably well, as demonstrated in Hogan et al. (2016) from the good agreement found with fully 3D shortwave calculations. This suggests that there is no systematic increase or decrease of in-cloud shortwave fluxes towards cloud edge. In the longwave, however, emission from within the cloud makes fluxes spatially more variable and ε_b is significantly different from 1. This effect is parametrised in Section 2.3.3.

While the distribution of fluxes in the clear sky also varies, the variance mostly depends on the distance from clouds, as these dominate the emission. We find it satisfactory to include this effect in the parametrisation of cloud geometry (described in detail in Chapter 3), and hence set ε_a to 1.

2.3.2 Effective direction of radiation transported through cloud sides

This section derives an expression for the coefficients f_{ab} and f_{ba} in (2.2), which describe the contribution to the rate of lateral exchange from the geometry of the cloud edge. Hogan and Shonk (2013) showed that if the diffuse radiation is assumed to be travelling in discrete directions with zenith angles of θ_{3D} and $\pi - \theta_{3D}$ (illustrated in Fig. 2.3a), then

the coefficients are given by

$$f_{ab} = \tan(\theta_{3D})\frac{L_{ab}}{\pi c_a}; \qquad f_{ba} = \tan(\theta_{3D})\frac{L_{ab}}{\pi c_b}, \tag{2.3}$$

where c_a and c_b are the fractions of the domain covered by regions a and b respectively, and L_{ab} is the length of cloud edge (i.e. the length of the interface between regions a and b in the horizontal plane) per unit area of the gridbox.

Hogan and Shonk (2013) equated θ_{3D} with the diffusivity angle θ_1 used in the definitions of γ_1, γ_2 and $S^{\downarrow\uparrow}$ and hence used $\theta_{3D} = 53°$. To test this, we appeal to the idealised case described in Section 2.2 and use SPARTACUS to simulate emission from an isothermal, cubic cloud in vacuum. In order to isolate purely the geometric effect, we consider a very optically thick non-scattering cloud so that the effective emissivity of the cloud, ε_b, is unity. The dot-dashed black line in Fig. 2.3b (provided by Robin Hogan) depicts the 3D factor $f_{\text{1D correction}}$ as a function of cloud fraction for $\theta_{3D} = 53°$, and it can be seen that the 3D effect reduces for increasing cloud fraction due to the increased probability of radiation emitted from the side of a cloud being absorbed by another cloud. In the limit of completely overcast skies, SPARTACUS has the correct limit of no 3D effect. However, in the limit of very small cloud fraction, $f_{\text{1D correction}}$ has a value of 2.65 rather than the value of exactly 3 both predicted by Theorem 2 in Section 2.2, and simulated with the fully 3D Monte Carlo radiation model MYSTIC (Mayer, 2009). This means that the isothermal cube is incorrectly emitting less from its sides than from its base in SPARTACUS.

The MYSTIC experiments which we use here and throughout this work to evaluate SPARTACUS, were conducted by Carolin Klinger and Bernhard Mayer at Ludwig-Maximilians-University Munich. MYSTIC has been validated by extensive comparison with other 3D state-of-the-art radiative transfer models (Cahalan et al., 2005) and both shortwave and longwave observations (Mayer et al., 2010; Emde and Mayer, 2007), and showed very good agreement. Klinger and Mayer (2014) showed that completely independent approaches in MYSTIC for calculating thermal heating and cooling rates are consistent with each other. For our experiments, thermal fluxes were calculated using 10^5 photons which resulted in a statistical noise of less than 0.1% for domain-averaged fluxes as shown here.

The red lines in Figure 2.3b show the results for a cubic cloud with an optical depth of 2; it can be seen that $f_{\text{1D correction}}$ is reduced from the value of 3 that is applicable only in

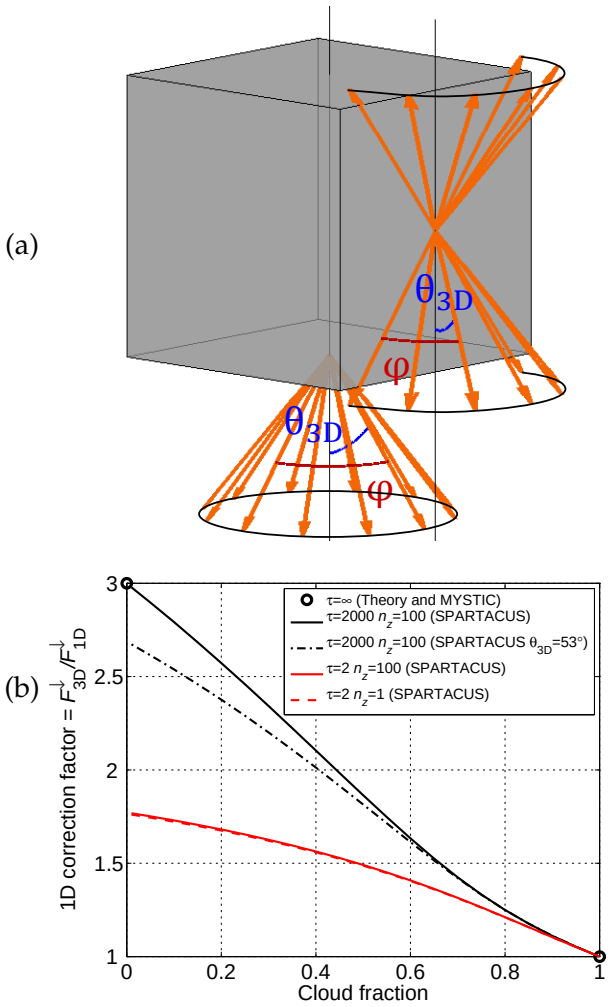

Figure 2.3: (a) Schematic of outward radiances from cloud base and cloud side in the approximation of discrete zenith angles θ_{3D} and $\pi - \theta_{3D}$ for a cubic cloud. (b) Dependence of 3D factor, denoted $f_{1D\,\text{correction}}$ in Section 2.2, on cloud fraction, for an isothermal, cubic cloud in vacuum, where optical depth is denoted in the legend by τ and the number of vertical layers by n_z (figure by Robin Hogan, MYSTIC results by Carolin Klinger and Bernhard Mayer). All SPARTACUS simulations use the effective zenith angle for lateral transport derived in Section 2.3.2 of $\theta_{3D} = 57.52°$, except for the black dot-dashed line that uses a value of 53°. The circles show the theoretical limits of very low cloud fraction and overcast sky for a very optically thick cloud, which agree with MYSTIC calculations.

the optically thick limit. The two red lines also confirm that SPARTACUS is not sensitive to vertical resolution. The details of how SPARTACUS is run with multiple layers were given by Hogan et al. (2016).

We wish to derive new expressions for f_{ab} and f_{ba} that ensure that vertical transport and horizontal transport between clear and cloudy regions are treated consistently. This can be thought of as finding a better value for θ_{3D}, but we need not make the assumption

that diffuse radiation travels only with two discrete zenith angles. We again consider a very optically thick non-scattering cloud, which can now have any shape. In this case, it can be seen from (2.2) that the rate of change of in-cloud fluxes due to lateral escape through the cloud sides is given by

$$\left.\frac{dF_b^{\downarrow}}{dz}\right|_{\text{lat}} = -f_{ba}F_b^{\downarrow}; \qquad -\left.\frac{dF_b^{\uparrow}}{dz}\right|_{\text{lat}} = -f_{ba}F_b^{\uparrow}. \tag{2.4}$$

The flux exiting the cloud sides over a thin layer of depth dz, per area of the entire gridbox, is then

$$-dF_b^{\downarrow} + dF_b^{\uparrow} = f_{ba}(F_b^{\downarrow} + F_b^{\uparrow})dz. \tag{2.5}$$

From this, we can compute the flux exiting a thin layer of the cloud side *per unit area of cloud side*, G_{side}, by dividing the left-hand side of (2.5) by the ratio of cloud side area in the thin layer to the horizontal area of the gridbox, $L_{ab}dz$, yielding: $G_{\text{side}} = f_{ba}(F_b^{\downarrow} + F_b^{\uparrow})/L_{ab}$. Since upwelling and downwelling radiation within the optically thick cloud are in equilibrium (as will be explained in Section 2.3.3.2), we have $F_b^{\downarrow} = F_b^{\uparrow}$ and hence

$$G_{\text{side}} = 2f_{ba}F_b^{\downarrow}/L_{ab}. \tag{2.6}$$

Meanwhile, the flux exiting the cloud base *per unit area of cloud base* is simply the downwelling flux $F_b^{\downarrow}$ (which is per unit area of the gridbox) divided by the cloud fraction:

$$G_{\text{base}} = F_b^{\downarrow}/c_b. \tag{2.7}$$

We require that the outgoing diffuse fluxes out of the base and sides are the same, i.e. $G_{\text{base}} = G_{\text{side}}$, so equating (2.6) and (2.7) yields

$$f_{ba} = \frac{L_{ab}}{2c_b}. \tag{2.8}$$

This may be used as a direct replacement for (2.3).

While the derivation of (2.8) has not assumed that the diffuse radiation travels in discrete directions, it is illuminating to equate (2.3) and (2.8), which reveals that the effective zenith angle to get the correct lateral transport is $\theta_{3\text{D}} = 57.52^{\circ}$. The fact that this value is larger than 53° means that it will lead to a larger 3D effect than in Hogan and

Shonk (2013) and indeed Figure 2.3b shows that when the new value is used, SPARTACUS yields the correct 3D effect (a value of $f_{\text{1D correction}} = 3$) for the isolated optically thick cubic cloud considered in Section 2.2.

As an alternative way to derive this angle, consider the approximation of all diffuse radiation being represented as upward and downward cones at zenith angles θ_{3D} and $\pi - \theta_{3D}$, respectively, both with radiance I, as illustrated in Fig. 2.3a. As each cloud particle's emission is isotropic, it is reasonable to assume that if the cloud's height and width are similar (as fulfilled for a typical cumulus cloud), the downward flux per area of horizontal cloud surface should equal the lateral flux per area of vertical cloud surface. The downward flux is found by integrating over all azimuth angles ϕ of the downward cone:

$$G_{\text{base}} = \int_0^{2\pi} I \cos\theta_{3D}\, d\phi = 2\pi I \cos\theta_{3D}. \tag{2.9}$$

If ϕ represents the azimuth angle of a beam of radiation with respect to the normal to a vertical surface representing part of the cloud side, then the flux through that surface is

$$G_{\text{side}} = 2\int_{-\pi/2}^{\pi/2} I \sin\theta_{3D} \cos\phi\, d\phi = 4I \sin\theta_{3D}, \tag{2.10}$$

Since emission per surface area of cloud base and cloud side should be the same, we set $G_{\text{base}} = G_{\text{side}}$, which also yields $\theta_{3D} = 57.52^\circ$.

2.3.3 Horizontal distribution of fluxes in cloud

In reality, the rate at which radiation escapes through the side of a cloud is proportional to the local value of the up- and downwelling diffuse flux in the cloud very near the cloud edge. This section parametrises the coefficient ε_b in (2.2), which quantifies the ratio of the near-edge fluxes to the mean flux in the cloud. Hogan and Shonk (2013) assumed fluxes to be homogeneous within the cloud, so that $\varepsilon_b = 1$. We can only be sure that this is valid in the longwave for optically thick non-scattering clouds (as assumed in Section 2.3.2).

To test the validity of assuming $\varepsilon_b = 1$ over a wider range of cloud properties, we again appeal to Theorem 1 in Section 2.2, which states that for an isothermal, homogeneous, isolated cubic cloud in vacuum, the outgoing lateral flux from each side face G_{side} equals the flux from top or base, G_{base}. Fully 3D calculations using MYSTIC have con-

firmed the ratio $G_{\text{side}}/G_{\text{base}} = 1$ for a range of scattering properties. We have computed this ratio with SPARTACUS assuming $\varepsilon_b = 1$ for various optical depths and single scattering albedos ω, shown as dashed lines in Figure 2.4. It is clear that $\varepsilon_b = 1$ performs poorly in general: in optically thin clouds the side flux is underestimated for all values of ω, because in reality lateral fluxes due to internal emission accumulate toward the edges of the cloud, making cloud edge fluxes just before escape larger than the mean in-cloud values. For optically thick clouds the side flux is overestimated, but only for strongly scattering clouds; this is because larger ω reduces the emissivity of the cloud edge, an effect not captured by SPARTACUS.

It should be stressed that these two phenomena also affect the outgoing fluxes at cloud top and base. The difference is that there they are fully represented in SPARTACUS via its use of the classical two-stream equations including explicit representation of the vertical exchange of radiation between upwelling and downwelling streams. Since SPARTACUS does not similarly resolve horizontally oriented fluxes and the exchange between radiation travelling towards and away from a cloud edge, these two phenomena are not simulated automatically so must be parametrised via the specification of ε_b in order to obtain consistent behaviour at cloud sides as at cloud base and top.

Our approach to parametrising ε_b is to use the two-stream equations to describe how outgoing horizontal fluxes at cloud sides relate to the cloud-average fluxes, depending on the cloud's optical properties. In the limiting cases of very optically thin or very optically thick clouds, the equations simplify enough to be solved analytically (Sections 2.3.3.1 and 2.3.3.2, respectively) and in Section 2.3.3.3 we combine these findings to obtain a parametrisation that may be used over the full range of optical depth.

2.3.3.1 Optically thin limit

As the two-stream scheme in SPARTACUS already calculates fluxes out of cloud top and base correctly, we can ask the question what value of ε_b results in the same lateral as vertical outgoing cloud edge fluxes, for the case of the isothermal homogeneous cubic cloud in vacuum. We denote the value in the limit of very low optical depth as $\varepsilon_{0,b}$. The fact that the bias at low optical depth shown in Fig. 2.4 is insensitive to ω suggests that $\varepsilon_{0,b}$ will be independent of ω. A limitation of this section is that our use of a cubic cloud means that strictly the result will only be applicable for clouds with a vertical-to-

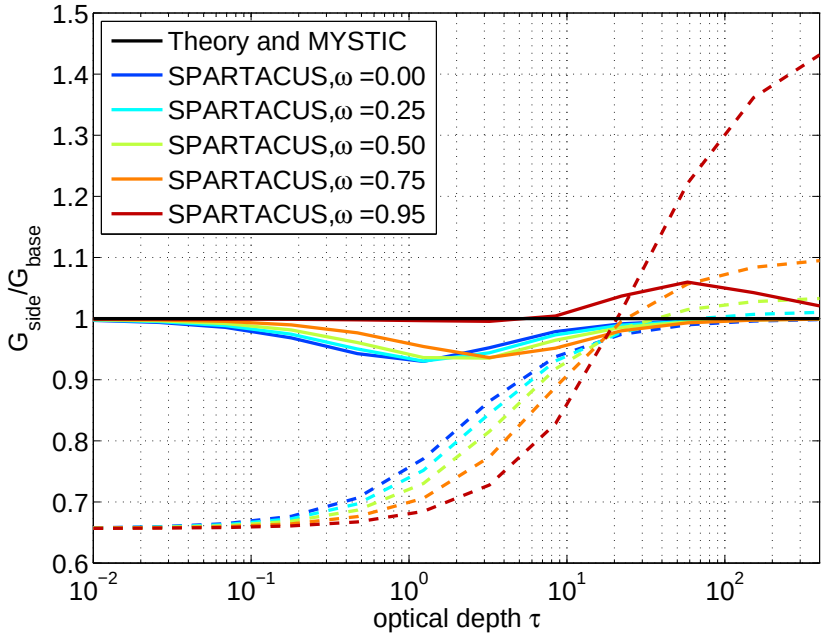

Figure 2.4: Ratio of horizontal to vertical outgoing fluxes $G_{\text{side}}/G_{\text{base}}$ from an isothermal homogeneous cubic cloud in vacuum at wavelength $\lambda = 10.7\mu$m (asymmetry factor $g = 0.85$) in SPARTACUS assuming $\varepsilon_b = 1$ (dashed lines) and with a full parametrisation of ε_b (solid lines), versus the logarithm of optical depth τ for different values of single scattering albedo ω. Both theory and fully 3D calculations using MYSTIC (by C. Klinger and B. Mayer) predict a value of unity for this ratio, shown by the black horizontal line.

horizontal aspect ratio of around unity, although we note that 3D effects get weaker as optical depth decreases, so this is not expected to have a strong impact on our estimate of the global impact of 3D radiative effects.

In the optically thin limit, radiation emitted from one cloud particle is very unlikely to encounter another before it leaves the cloud, so we can neglect the scattering and absorption terms in (2.2) and the upwelling and downwelling streams decouple. Thus the equation for the downwelling in-cloud flux becomes

$$\frac{dF_b^{\downarrow}}{dz} = \beta_b S_b^{\downarrow} - f_{ba}\varepsilon_{0,b} F_b^{\downarrow}, \tag{2.11}$$

which has a general solution

$$F_b^{\downarrow}(z) = X \exp(-f_{ba}\varepsilon_{0,b} z) + \frac{\beta_b S_b^{\downarrow}}{f_{ba}\varepsilon_{0,b}},$$

where X is a real number. Since we are concerned with radiation originating from within

the cloud, we insert the boundary condition of no downward flux at cloud top, i.e., $F_b^{\downarrow}(z=0)=0$, which gives $X=-\beta_b S_b^{\downarrow}/f_{ba}\varepsilon_{0,b}$, and therefore

$$F_b^{\downarrow}(z)=\frac{\beta_b S_b^{\downarrow}}{f_{ba}\varepsilon_{0,b}}\left[1-\exp(-f_{ba}\varepsilon_{0,b}z)\right]. \tag{2.12}$$

Similarly, the equation for downwelling clear-sky flux due to emission from cloud sides (i.e., without internal clear-sky sources) reduces to

$$\frac{dF_a^{\downarrow}}{dz}=f_{ba}\varepsilon_{0,b}F_b^{\downarrow}=\beta_b S_b^{\downarrow}\left[1-\exp(-f_{ba}\varepsilon_{0,b}z)\right]. \tag{2.13}$$

The solution, again using the zero upper boundary condition $F_a^{\downarrow}(z=0)=0$, is

$$F_a^{\downarrow}(z)=\beta_b S_b^{\downarrow}\left[z+\frac{\exp(-f_{ba}\varepsilon_{0,b}z)-1}{f_{ba}\varepsilon_{0,b}}\right]. \tag{2.14}$$

We consider a cloud with a vertical depth of Δz; hence at the level of cloud base, $F_b^{\downarrow}(\Delta z)$ is the radiation emerging from cloud base and $F_a^{\downarrow}(\Delta z)$ is the radiation that originated from the cloud sides. From Theorem 1 in Section 2.2, we know for a cubic, isothermal cloud that

$$F_a^{\downarrow}(\Delta z)=2F_b^{\downarrow}(\Delta z). \tag{2.15}$$

Substituting in (2.12) and (2.14) and simplifying yields the following implicit equation for $\varepsilon_{0,b}$:

$$3\exp(-\varepsilon_{0,b}f_{ba}\Delta z)+\varepsilon_{0,b}f_{ba}\Delta z=3 \tag{2.16}$$

For a cubic cloud with depth Δz in a gridbox of area A, the cloud fraction is $c_b=\Delta z^2/A$ and the cloud edge length per unit area is $L_{ab}=4\Delta z/A$. Combining with the definition of f_{ba} in (2.8) indicates that $f_{ba}\Delta z=2$. The numerical solution in this case is $\varepsilon_{0,b}=1.4107$. Equation (2.16) for $f_{ba}\Delta z=2$ actually has an analytical solution: $\varepsilon_{0,b}=\left[W\left(-3\mathrm{e}^{-3}\right)+3\right]/2=1.4107$, where W is the Lambert W function (Lambert, 1758; Euler, 1783). As expected, $\varepsilon_{0,b}>1$, to represent the accumulation of outward emission towards the cloud edge that results in a higher flux than the in-cloud average.

2.3.3.2 Optically thick limit

In the interior of a very optically thick cloud, the radiance in any direction is equal to the Planck function at the temperature of the cloud, but if the cloud particles have a non-zero single scattering albedo then the flux emitted by the cloud will be less than the Planck value, i.e. its emissivity will be less than 1. This is because the presence of scattering particles gives the cloud a non-zero reflectance, and if there is no transmission, the absorptivity (equal to the emissivity) must be 1 minus the reflectance. In the limit of very large optical depth, ε_b becomes the actual emissivity of the cloud, which we write as $\varepsilon_{\infty,b}$.

Two-stream computations (including SPARTACUS) correctly reduce the vertically up- and downwelling longwave fluxes out of the top and base of an optically thick cloud from the Planck value, corresponding to an emissivity of less than 1.

For SPARTACUS to capture this effect at cloud sides as well, we need to specify the emissivity $\varepsilon_{\infty,b}$ directly. This quantity may be calculated from the two-stream equations by treating the optically thick cloud as semi-infinite. In this particular case, we neglect horizontal transport terms, because for the thin layers at cloud edges that are relevant to this calculation, the lateral gain and loss terms are dominated by the γ_1 and γ_2 terms. The two-stream equations in this case have been solved by various authors, such as Petty (2006) whose Eq. (13.45) described the albedo of a semi-infinite cloud, r_∞. The emissivity is then

$$\varepsilon_{\infty,b} = 1 - r_\infty = \frac{2\sqrt{1-\omega}}{\sqrt{1-\omega g} + \sqrt{1-\omega}}, \tag{2.17}$$

where g is the asymmetry factor of the medium in region b.

2.3.3.3 Parametrisation depending on optical depth

For general optical depth, the correct parametrisation of the edge flux is more complicated, due to the interaction of several effects that partially compensate each other, and cannot be analytically solved. We find that a satisfactory empirical approximation of ε_b is

$$\varepsilon_b(\tau, \omega, g) = \frac{\varepsilon_{0,b} - \varepsilon_{\infty,b}(\omega, g)}{\tau(1-\omega)+1} + \varepsilon_{\infty,b}(\omega, g). \tag{2.18}$$

This distribution has limiting values that agree with the analytical results for $\tau \to 0$ (found in Section 2.3.3.1) and $\tau \to \infty$ (found in Section 2.3.3.2). Note that in terms of practical application of (2.18) in the SPARTACUS radiation scheme, τ is the *horizontal* optical depth of a typical cloud in a given layer, which can be estimated by multiplying the extinction coefficient by the typical cloud diameter. In the implementation of SPARTACUS, we use as a measure of this the similar *effective cloud scale* (discussed in Chapter 3) that we also use for characterising cloud edge length, as outlined by Hogan and Shonk (2013) and Jensen et al. (2008).

To check that treatment of lateral and vertical cloud edge fluxes is consistent, we repeat the SPARTACUS calculations shown in Fig. 2.4 for a homogeneous, isothermal, cubic cloud in vacuum, but this time with the new parametrisation for ε_b (shown by the solid lines). This time the ratio $G_{\text{side}}/G_{\text{base}}$ is much closer to the value of 1 expected from theory and found from fully 3D calculations using MYSTIC, and constitutes a significant improvement on the results without the parametrisation.

2.4 Implementation and evaluation of SPARTACUS

For large-scale or global experiments, we need an efficient implementation of SPARTACUS in the context of a global model's radiation code. Based on the theory and experiments discussed in Sections 2.2 and 2.3 and the MATLAB version of SPARTACUS we developed, Robin Hogan has provided an efficient SPARTACUS implementation using Fortran. As detailed by Hogan et al. (2016), this implementation utilises a reformulation of the radiative transfer equations (shown in Equation (2.2) for the longwave diffuse fluxes) for both direct and diffuse fluxes, for all regions and all vertical layers simultaneously as matrix differential equations (Hogan et al., 2016, Equations (2)-(7) in the shortwave and (35)-(38) in the longwave). The matrix differential equations can then be solved using matrix exponentials, a more elegant, accurate and efficient method than iteratively solving the equations for each region and radiation stream separately, as done by Hogan and Shonk (2013). The complete solution for the multi-layer atmosphere is found by first passing up through the atmosphere and determining the directional overlap matrices that control the partition of up- and downwelling radiation between regions at layer boundaries and the albedo of the entire atmosphere below, then passing back

down through the atmosphere and computing the profile of flux solutions, as described by Equations (20), (32) and (34) in Hogan et al. (2016).

Using the solution method discussed above, Robin Hogan has implemented a modular Fortran version of SPARTACUS for use in global models such as the ECMWF's Integrated Forecast Scheme (IFS) model. We have tested and debugged this code before applying it in our global experiments. It employs the Rapid Radiative Transfer Model for General Circulation Models (RRTM-G; Mlawer et al., 1997) for computing gas optics, which uses a correlated-k distribution method for calculations in each of 30 spectral bands. Cloud inhomogeneity is represented with the Tripleclouds method of Shonk and Hogan (2008), which splits the cloudy region into an optically thick and an optically thin sub-region. The sub-regions' optical depths are scaled so as to represent the inhomogeneity (measured by the fractional standard deviation, or standard deviation divided by the mean, of optical depth) while preserving average in-cloud optical depth. We can run this radiation scheme using the SPARTACUS solver with 3D effects (3D), without cloud-side effects but including in-region horizontal transport in the shortwave only (1D) or without both of these 3D effects in ICA and McICA modes.

As cloud geometry input, SPARTACUS requires the cloud fraction in each layer, and a parameter describing overlap of the regions in different vertical layers. The Tripleclouds implementation offers the option to control overlap between the two cloudy regions and between clear and cloudy regions separately. Additionally, for the 3D calculations, we need to provide a measure of the cloud edge length in each layer, as this controls how much cloud side and therefore how much cloud side transport there is. This parameter has to describe the cloud edge length *relevant for radiative transfer*, which is not necessarily the same as the cloud edge length measured in a high-resolution field of physical cloud properties. We will address this question in detail in Chapter 3, discussing the best parameter to use, how to derive the radiatively relevant cloud edge length from a given cloud field and how to parametrise it generally for each cloud type. We find from both theoretical considerations and evaluation of SPARTACUS's performance using different inputs against MYSTIC in idealised cases that for cumulus clouds, as we consider here, the edge length of a convex approximation to each cloud's layer cross section by an ellipse is a good measure of the radiative effective cloud edge length. For exact results, we also need to account for cloud clustering (which enhances intercep-

tion of radiation leaving each cloud's sides by neighbouring clouds), which we find can be done by decreasing the effective cloud edge length.

In order to evaluate how well SPARTACUS performs for realistic cases, Hogan et al. (2016) again compared against fully 3D MYSTIC calculations by Carolin Klinger and Bernhard Mayer. In the 1D case the 6-stream DISORT solver was used as the reference, which produces nearly identical results to MYSTIC in 1D but is much cheaper. Both MYSTIC and DISORT belong to the 'libRadtran' library (Mayer and Kylling, 2005), hence Hogan et al. (2016) denoted both these models by "libRadtran". In this thesis, we also refer to all these calculations as MYSTIC calculations (even though that is not precisely correct). The comparison was conducted for a realistic large-eddy-simulation (LES) of continental shallow cumulus cloud by Hinkelman et al. (2005), also used in the Intercomparison of 3D Radiation Codes (I3RC) project (Cahalan et al., 2005). Clouds are described by their liquid water content and effective cloud particle radius in a periodic domain measuring 6.4 km in each horizontal dimension with a resolution of 67 m in the horizontal and 40 m in the vertical. The atmospheric temperature profile is that of the mid-latitude standard atmosphere, with a temperature of 21° at the surface and 16° at cloud base, and we set surface shortwave albedo to 0.08 and longwave emissivity to 0.98.

Table 2.1 gives an overview of cloud radiative effect (CRE) results in the 1D codes, and the change in CRE due to 3D effects in libRadtran and SPARTACUS. Shortwave CRE is strongest, but in the shortwave the sign of the 3D effect depends on the solar zenith angle. In the longwave, CRE is always positive, and 3D effects always enhance this effect. Longwave 3D effects are strongest at the surface, at about 30% of CRE, both because longwave CRE itself is strongest at the surface, and because the strongest 3D effects are caused by small broken clouds low in the atmosphere. When we use the appropriate cloud geometry input and account for cloud clustering, SPARTACUS agrees well with fully 3D MYSTIC calculations in both longwave and shortwave, and accurately captures the 3D effect.

3D cloud effects in the shortwave and hence the shortwave differences between the various models change with the angle of solar illumination. Figure 2.5 shows how reflected broadband shortwave flux at TOA, direct solar flux and the shortwave 3D effect in both libRadtran and SPARTACUS depend on the solar zenith angle. SPARTACUS 3D calculations reproduce the SZA-dependence in 3D libRadtran well, while the results

Table 2.1: Cloud radiative effects (CRE) simulated by libRadtran (MYSTIC) and SPARTACUS for the cumulus cloud field discussed in Section 2.4: top-of-atmosphere (TOA) shortwave CRE at solar zenith angles of 0° and 75°, and longwave CRE at both surface and TOA. The first column presents the results when all 3D effects are neglected (ICA), while the remaining columns show the change to CRE due to including 3D effects, in $\mathrm{W\,m^{-2}}$ and %. The longwave 3D effects for SPARTACUS are computed after the radiatively effective cloud edge length has been multiplied by a factor of 0.69 to approximately represent the effects of cloud clustering; the numbers in parentheses indicate the results when this effect has not been accounted for. Table from Hogan et al. (2016).

Spectral region/location	Model	ICA CRE ($\mathrm{W\,m^{-2}}$)	3D effect ($\mathrm{W\,m^{-2}}$)	3D effect (%)
Shortwave TOA (0°)	libRadtran	−98.1	+24.1	−25%
	SPARTACUS	−97.3	+24.5	−25%
Shortwave TOA (75°)	libRadtran	−31.5	−15.3	+49%
	SPARTACUS	−30.1	−9.7	+32%
Longwave surface	libRadtran	13.1	3.8	29%
	SPARTACUS	14.1	4.6 (6.3)	32% (45%)
Longwave TOA	libRadtran	2.9	0.25	9%
	SPARTACUS	2.8	0.39 (0.69)	14% (25%)

of SPARTACUS using an ICA solver closely follow those of the libRadtran ICA scheme. There is a noticeable difference in reflected TOA flux between ICA and 3D calculations in libRadtran and SPARTACUS, especially for overhead sun, while the results of SPARTACUS 1D are closer to the 3D libRadtran and SPARTACUS results. The different behaviour of the 1D schemes strongly suggests that this bias in the ICA schemes is a consequence of neglecting in-region horizontal transport. The treatment of horizontal in-region transfer by assuming completely homogeneous fluxes in regions as implicit in region-based two-stream schemes like SPARTACUS 1D could potentially overestimate the effect. We have seen in Section 2.3.3 that assuming completely homogeneous fluxes in the cloud causes errors in cloud side fluxes in the longwave, which we compensate through our cloud side flux parametrisation. We also adopt a longwave solver that does not include in-region transport in the longwave in the SPARTACUS 1D model, since the effect is negligible anyway in the longwave.

The fact that SPARTACUS 1D upwelling shortwave flux is close to the upwelling

flux in the 3D calculations in Figure 2.5a for high sun indicates that in-region horizontal transport is not significantly overestimated by the shortwave flux homogeneity assumption. This might be partly because the SPARTACUS solver uses the Tripleclouds method to represent cloud inhomogeneity by two cloudy regions. This means that fluxes in the SPARTACUS solver are not in fact homogenised throughout the whole cloudy area, but only within each region, which reduces the estimate of the in-region horizontal transfer effect. The reflectivity reduction due to cloud side leakage for high sun could potentially hide a small overestimation of in-region horizontal transport and also exacerbate the difference between ICA and 3D results, but as we will see in Section 4.3.1, this effect is not very strong compared to other 3D cloud effects. The underestimation of upwelling fluxes at low sun in all 1D schemes is explained by the 3D cloud side illumination effect they neglect. The flux results of McICA calculations show that this method is indeed unbiased with respect to other ICA calculations, although McICA adds a noticeable amount of noise.

2.5 Conclusions on SPARTACUS development

Three-dimensional radiative effects systematically and significantly increase the longwave cloud radiative effect of cumulus clouds, an effect that has been largely neglected in the literature. Hogan and Shonk (2013) presented an idea for how to capture 3D shortwave cloud effects in a two-stream radiation scheme at a numerical cost suitable for use in a global model. We provide many improvements to their method, and we refer to the resulting radiation scheme as SPARTACUS. This chapter has developed the longwave capabilities of SPARTACUS. We have first proposed a benchmark case: an isolated, homogeneous, isothermal, cubic cloud in vacuum, for which the 3D effect is known theoretically. In the optically thick limit, 3D effects increase its cloud radiative effect by a factor of exactly 3. This benchmark has been used to ensure consistent treatment of horizontal and vertical fluxes at every step of the method, since the flux out of each of the six faces of the cube should be the same. It is shown that if diffuse radiation is assumed to be travelling in two discrete directions, then in computing fluxes out of cloud sides, a zenith angle of $\theta_{3D} = 57.52^\circ$ must be used, rather than the $\theta_1 = 53^\circ$ most often used for vertical transport calculations in the longwave. We also find that in the longwave, the spatial distribution of fluxes within the clouds is important, and develop

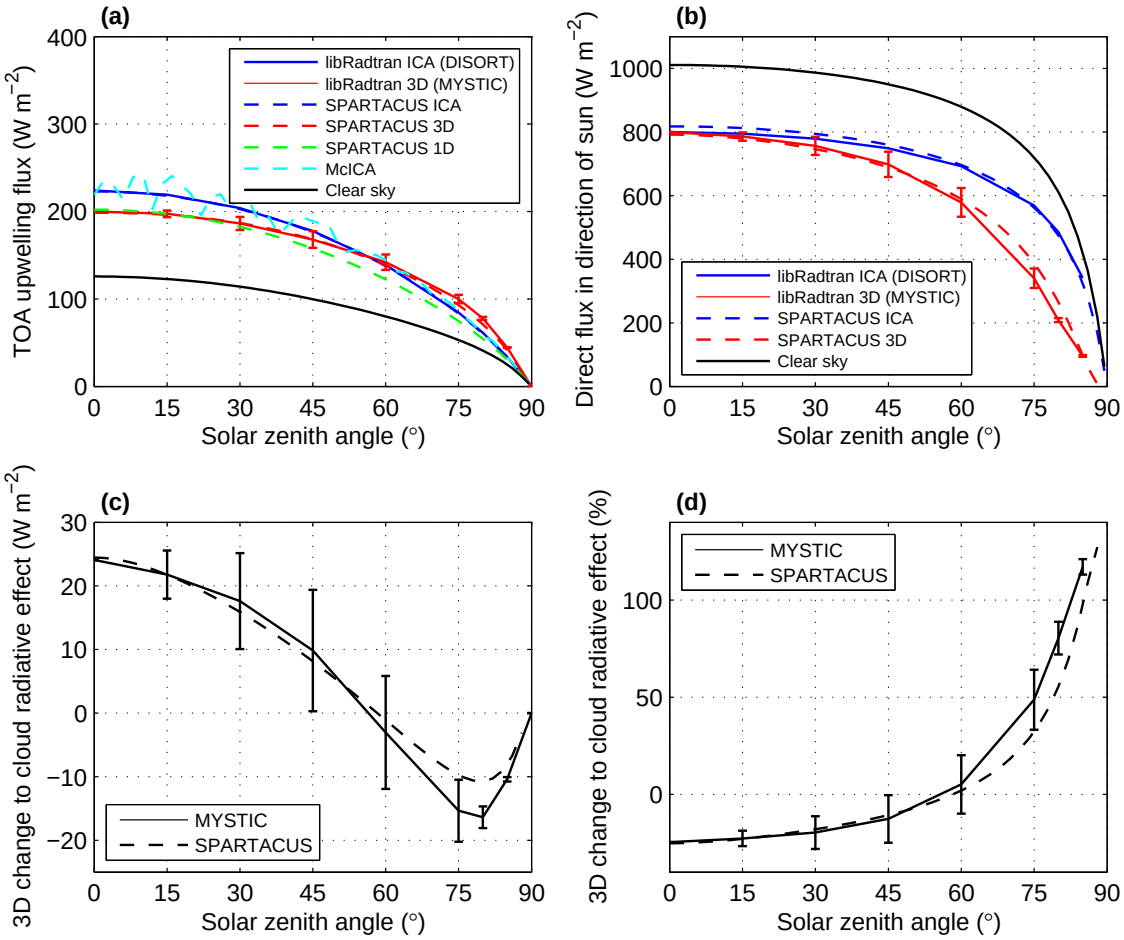

Figure 2.5: Comparison of simulated broadband shortwave fluxes from libRadtran (using the libRadtran or MYSTIC Monte Carlo solver for 3D calculations) and SPARTACUS for the I3RC cumulus test case, versus solar zenith angle. (a) Top-of-atmosphere (TOA) upwelling fluxes for the two models both including lateral transport (3D) and excluding it (ICA), along with values for clear skies. (b) As panel a but comparing the direct component of surface solar flux into a plane perpendicular to the sun. (d) The change to TOA cloud radiative effect due to the inclusion of 3D effects. (d) As panel c but as a percentage. The libRadtran 3D results are averaged over four calculations with steps of solar azimuth angle 90° apart, and the error bars in each panel represent the standard deviation of these four simulations. Figure by Robin Hogan, based on Hogan et al. (2016), Figure 4, but with additional lines in Panel a) showing the results of SPARTACUS 1D with in-region horizontal transport (dashed green line) and SPARTACUS in McICA mode (dashed cyan line).

a parametrisation for the flux values at cloud sides that represents the build-up of fluxes towards cloud edge in the optically thin case and cloud-edge emissivity in the optically thick case. The decisive cloud geometry parameter for determining the cloud side fluxes correctly is the effective cloud edge length relevant for radiation, which will be derived in detail in Chapter 3.

Hogan et al. (2016) described much of the further work needed to prepare SPARTACUS for use in a large-scale atmospheric model. They introduced an elegant method for solving the two-stream equations modified to include 3D effects, and incorporated full representation of gas absorption and surface effects, enabling them to perform a realistic comparison between SPARTACUS and fully 3D broadband radiative transfer calculations for cloud fields in both the shortwave and longwave, in which they find good agreement. We are hence satisfied that SPARTACUS performs well when provided with the appropriate cloud geometry input (discussed in Chapter 3), and is suitable for use in large-scale experiments to estimate 3D cloud-radiation effects on larger scales than can be easily investigated with fully 3D models. Comparison to different 1D models that treat in-region horizontal transport differently allows us to distinguish the separate 3D effects.

Chapter 3

Characterising cloud geometry from observations and high-resolution models

3.1 Introduction and motivation

Describing cloud geometry is a challenge. If we want to be exact, it is not even a priori clear where a cloud begins and ends: it is a collection of small ice and water particles slowly falling in space, surrounded by "clear sky" that also contains such particles at a lower concentration, and often surrounded by other clouds. We usually define as cloudy any volume with particle concentration over a chosen threshold. This definition is sensitive to the choice of threshold and does not represent the full variability of droplet concentration within the cloud and in the neighbouring area (the so-called "twilight zone"; e.g. Koren et al. 2007). In cases where cloud edges are not sharp, this can lead to retrieval and calculation errors.

The division into cloud and clear sky also opens up a new question: how to geometrically describe the clear and cloudy regions and the edge separating them. Any precise answer would need three-dimensional cloud observations on scales down to those of individual cloud particles, which are not available. However, in the context of large-scale models' radiation calculations of spatially and angularly averaged quantities like radiative fluxes and heating rates not all of this information is necessarily relevant.

So, which aspects of a cloud's geometry do we need to capture in order to calculate the cloud's interaction with radiation correctly? All radiation schemes need information about the fraction of the domain that is covered with cloud at each vertical level, and on how the clouds in different layers overlap. For traditional region-based two-stream radiative transfer schemes based on the plane-parallel assumption, these two cloud ge-

ometry parameters are sufficient. However, as discussed in Section 1.2, real clouds do not fulfil this assumption, both due to their finite extent and to internal variability, and the errors caused by the plane-parallel assumption amount to around 14% of the global cloud radiative effect (Shonk and Hogan, 2010). In reality, horizontal transfer between regions with different properties changes the radiation's subsequent behaviour noticeably. All real clouds are of finite size, and many cloud fields are broken and contain many cloud edges, meaning cloud edge effects can not simply be dismissed. As we have seen in Chapter 2, the length of cloud edge controls the amount of radiative transport through cloud sides. In trying to establish how large the radiative effect of horizontal transport through cloud edges truly is, we hence need additional information on the size and edge length of individual clouds, as well as on their spatial distribution, since this determines to what extent radiation leaving one cloud is intercepted by other clouds.

In this chapter, we are searching for a simple way to characterise cloud edge as relevant to radiation, consisting of few enough variables to be practical for use in SPARTACUS in a global context. The characterisation should depend solely on globally available parameters like cloud fraction, geographic position, height and meteorological conditions. We base our parametrisation on analysis of high-resolution 3D cloud cases from both observations and cloud-resolving models. Section 3.2 summarises previous work on the analysis of cloud geometry. As the geometry characterisation methods we find in the literature are not exactly suited to providing geometry input for SPARTACUS, we devise our own geometry description in Sections 3.3 and 3.4. Section 3.3 quantifies the physical effects that cause cloud edge as seen by radiation to be smoother than the cloud edge apparent in high-resolution cloud water fields, and presents a method to account for these effects. This section was published as Schäfer et al. (2016). Section 3.4 derives a geometry variable, the *effective cloud scale*, that only depends on cloud type and together with the cloud fraction, which is available from global satellite observations and in global models, captures the radiative effective cloud edge length in each cloud layer. In Section 3.5, we analyse high-resolution cases of various cloud types, in both observations and cloud-resolving simulations, to estimate typical values of effective cloud scale for each cloud type. Section 3.6 summarises our findings, and describes what input range for global SPARTACUS experiments we choose based on the case studies.

3.2 Previous work on cloud size, shape and spatial distribution

Measures of cloud shape and cloud distribution are relevant in contexts other than radiation: turbulent mixing at cloud edges, vital for determining the cloud's dynamic development and role in energy and moisture transport, is also determined by the scales of clouds and the distances between them. Hence, cloud size distributions have been extensively studied for various cloud types in a variety of data sources: they have been estimated from one-dimensional cross-sections seen in in-situ measurements from aircraft (Davis et al., 1999), or at any given height in a vertically pointing instrument's time-height section of measurements (Cahalan and Snider, 1989), or in in two-dimensional images like aircraft photographs (Plank, 1969) or satellite snapshots including Landsat (e.g. Wielicki and Welch, 1986; Cahalan and Snider, 1989) and MODIS data (e.g. Jensen et al., 2008; Wood and Field, 2011). Cloud-resolving models (CRM) and large-eddy simulations (Neggers et al., 2003a) offer three-dimensional cloud fields, as can the comparatively new scanning cloud radar. Comparisons between studies can be challenging, due to the different dimensionality, sensitivity and resolution of the data sources, but also because of different definitions of "cloud size" and "cloud spacing".

In radiative transfer, the first approach has been to approximate clouds by simple geometric shapes like cubes or cylinders, in various spatial distributions. For example, Welch and Wielicki (1984) investigated the impact of the shape assumptions, while Heidinger and Cox (1996) summarised different spatial distributions. While the results of radiation calculations with these assumptions can agree with observations reasonably well (Heidinger and Cox, 1996, e.g. Figure 4), the cloud geometry assumptions themselves are obviously not realistic.

Investigations into cloud structure have found (e.g. Lovejoy, 1982) that a more realistic way to describe the irregular shape of clouds and their boundaries is through fractal models, as suggested by Mandelbrot (1977) and Mandelbrot (1983). Fractal geometry describes objects with irregular structure on a range of scales, whose geometric parameters can be related to spatial scale by power laws over several orders of magnitude. For physical objects, any description will only hold for a limited range of scales, since data resolution and total size of the domain impose minimum lower and maximum upper bounds on the scales. Geometric descriptions that utilise several relations for the same parameter, each of which is relevant for parts of the geometric space or on a particular

range of spatial scales are often termed "multi-fractal" (e.g. Falconer, 1990, p. 254-255). In particular, in many cases one parameter can be described by a sequence of power laws with different exponents for different scale ranges, separated by "scale breaks". The most common way of characterising fractal geometry is by the exponents of the various power laws. These are often termed dimensions, although this nomenclature can be confusing, as power laws for different geometric variables can behave differently for the same object, so a general "fractal dimension" is not well-defined (Falconer, 1990). Many mathematical definitions of "fractal dimensions" are based on the asymptotic behaviour of power laws at infinitely fine scales (e.g. Falconer, 1990), which cannot be tested for physical data. However, the various power law exponents (or "dimensions") have in common that they measure geometric irregularity, where increasing exponents correspond to more irregular structures; so for many structures the different fractal dimensions correlate and might change at similar scale breaks (if these represent changes in geometry that affect several parameters). There are formulae that relate various power law exponents for specific classes of structures (e.g. Mandelbrot, 1983).

With regards to our question of determining the edge length of a cloud in a horizontal plane, the irregular cloud structure (as described by fractals) means that the perimeter measured in any cloud data set depends on the spatial resolution. With finer resolution, more small details are visible and cloud edges appear more irregular, increasing the measured edge length. This question is similar to one of the first problems for which a fractal description was considered: how the edge of an area on a map depends on the spatial resolution of the measurement. Mandelbrot (1967) suggested that (for coastlines) a good empirical law to describe the dependence of the measured edge length p on resolution Δx was

$$p(\Delta x) \propto \Delta x^{1-D_d}, \tag{3.1}$$

where D_d can be termed the "divider fractal dimension", as it is derived from measuring perimeter at various resolutions, equivalent to using dividers of various sizes. Thus we have a fundamental observational problem: Cloud edge length is not a well-defined quantity, but depends on resolution. In order to derive cloud edge length for radiation calculations, we need to decide what scale is appropriate for measuring the edge length in a radiation context.

The scaling of perimeter with resolution has not commonly been investigated for

real clouds, but other power laws of geometric variables have been analysed, like the dependence of perimeter on the square root of the cloud's area (yielding the "perimeter fractal dimension" D_p as the power law exponent) by Lovejoy (1982) for a variety of clouds and rain, by Cahalan and Snider (1989) for marine cumulus and stratocumulus in Landsat radiance fields and by Siebesma and Jonker (2000) for liquid water fields of simulated cumulus. The perimeter and divider fractal dimensions coincide in some cases (although not in general), meaning in the absence of other information this gives us some idea of how the edge length might vary with resolution. Studies have found a perimeter fractal dimension of about $4/3$ for shallow cumulus for both observed (e.g. Cahalan and Joseph, 1989) and simulated clouds (Siebesma and Jonker, 2000). Another relationship described through power laws is that of the number distribution of clouds to the square root of their area, analysed by Cahalan and Snider (1989) and Cahalan and Joseph (1989) for marine stratocumulus, cumulus and deep convection. This power law is termed "Korčák's law", and its exponent B can be linked to perimeter fractal dimension by $B = D_p/2$ for a number of fractal objects (Cahalan and Joseph, 1989; Mandelbrot, 1983, pp.117-118).

Another common method of analysis is in Fourier space, relating the amplitude of the wavenumber Fourier spectrum to the wavenumbers by a power law. This spectrum also measures irregularity, as smooth geometries do not have any contributions from high wavenumbers (corresponding to small spatial scales), while fields containing small-scale irregularity do. This method takes into account the full variability of the cloud field instead of the binary distinction between cloud and clear area (like area and perimeter investigations do), and hence it is more appropriate for analysing scenes with high cloud fraction, which may not have many separate clouds and edges, or for studies that are also interested in in-region inhomogeneity. Wavenumber spectra were analysed in Landsat radiance data at 30 m spatial resolution by Cahalan and Snider (1989), Marshak et al. (1995), Davis et al. (1997) and Barker and Davies (1992) for marine cumulus and stratocumulus. These studies consider one-dimensional Fourier spectra of data lines extracted from the two-dimensional image, which facilitates comparison with one-dimensional data sources like vertically pointing radar data of total column water, or in-situ aircraft measurements. Barker and Davies (1992) also investigated the two-dimensional Fourier spectra of the image and found that the clouds were not completely

isotropic, and hence results of one- and two-dimensional Fourier analysis could differ.

Based on the observed statistics of cloud geometry stochastic cloud models have been developed that reproduce these statistical properties of cloud geometry; their complexity ranges from highly idealised one-dimensional cascade models like those by Marshak et al. (1994) and Cahalan (1994) to more specialised models that also incorporate meteorological information and aim to produce realistic 3D cloud fields of a particular cloud type, such as cirrus (Hogan and Kew, 2005), stratocumulus (Di Giuseppe and Tompkins, 2003a) or cumulus (Evans and Wiscombe, 2004; Prigarin and Marshak, 2009). In the absence of high-resolution 3D cloud observations, such models have been used for studies of the effects of cloud shape (Hinkelman et al., 2007), cloud inhomogeneity (Cahalan et al., 1994a) and 3D cloud-radiation (Di Giuseppe and Tompkins, 2003a).

Many of the Fourier analysis studies found breaks in scaling behaviour. Typical scale breaks mentioned are between 200 m and 2 km for marine clouds, but can vary depending on the type of analysis even for the same scene (e.g. Cahalan and Joseph, 1989). Fourier analysis of radiances, the most widely used method, suggests one scale break at $\approx$ 200 m for stratocumulus, and another at several kilometres. Marshak et al. (1995) and Davis et al. (1997) explained these as follows: while they associated the break at the larger scales with the size of the largest clouds, they argued that the smaller scale break at $\approx$ 200 m is specific to radiative measurements, and caused by three-dimensional radiative transfer: radiation spreads out horizontally from its point of origin, and is subsequently scattered into the direction of the receiver. Net radiative transport is directed from areas with high to those with lower radiation density, so this effect smooths out some of the variability of the cloud water field in radiance measurements at scales up to the spatial range of horizontal radiative transport (especially at highly scattering wavelengths). Radiative flux fields that are also integrated over a range of angles should appear even smoother.

An indication that this scale break is indeed due to radiative effects is that it does not appear in the spectrum of the liquid water path derived from microwave radiometer data shown in Cahalan and Snider (1989). Marshak et al. (1995) and Davis et al. (1997) found that the irregularities of radiance fields for fractal cascade model cloud scenes, calculated with radiation models that do and do not include 3D radiation, diverge for scales smaller than a "radiative smoothing scale" $\eta_{rad} \approx 200$ m, and also derived this scale theo-

retically for stratocumulus clouds using a diffusion approximation. They found that the average size of the diffusion region was $\langle\rho\rangle = \Delta_z / \sqrt{(1-g)\tau}$ for reflected and $\langle\rho\rangle \approx \Delta_z$ for transmitted radiation, and the radiative smoothing scale η_{rad} was 2–3 times $\langle\rho\rangle$. Here, Δ_z is the height of the cloud layer, τ the optical depth and g the single scattering albedo. Radiative smoothing is most pronounced in the shortwave spectral region, where multiple scattering leads to isotropic diffuse fluxes, but the effect also occurs for isotropic emission in the longwave.

This is relevant to our problem as we aim to determine the cloud edge length *relevant for radiative transfer*, which corresponds to the cloud edges seen in radiation fields. When analysing fields of cloud water content we need to account for smoothing up to the radiative smoothing scale (leaving larger-scale features unchanged) before determining the cloud edge length. Another important question is how clustered the clouds are, as this determines the distance between clouds and therefore how much of the radiation from each cloud is intercepted by its neighbours. We will address and quantify these effects and their impact in Section 3.3.

The Fourier analysis method has the advantages of avoiding the issue of distinguishing cloud from clear sky and being able to represent internal cloud inhomogeneity, which make it useful in determining the impact of effects like radiative smoothing on total cloud variability. However, for studies of cloud edge, this method is not well-suited, since the spectrum does not separate variability due to cloud edges from internal variability. To resolve the cloud side effect explicitly in SPARTACUS, we require a measure of cloud edge per horizontal area. As discussed above, this should be measured at a resolution of about the radiative smoothing scale in order to represent the right amount of edge detail relevant for radiative transfer. We aim to parametrise the amount of cloud edge depending on the cloud information available in a large-scale model, which is geographic location and height of the clouds and cloud fraction and water content at each vertical level.

The dependence of cloud edge in a cloud field on cloud fraction has previously been studied by Jensen et al. (2008), who studied the dependence on cloud fraction of the fraction of cloud perimeter to cloud area in scenes of marine boundary layer clouds measured by MODIS aboard NASA's Terra satellite. Morcrette (2012) investigated the dependence of normalised cloud perimeter on cloud fraction in both idealised cloud

distributions and cloud mask images based on Meteosat Second Generation's infrared imager. While these studies provide helpful ideas on the best parameters to describe cloud edge amount per area, the observations they use are both horizontally projected and at coarse resolutions of 1 km or larger. As we have reasoned above, the appropriate edge length for use in SPARTACUS should be derived at each vertical level and at a resolution of around the radiative smoothing scale of $\eta_{rad} \approx 200\,\mathrm{m}$. We therefore find it necessary to conduct our own analysis of high-resolution 3D case studies for a range of cloud types, which will be discussed in Section 3.5, after we derive the best parameter to describe effective edge length depending on cloud type and cloud fraction in Section 3.4.

3.3 Quantifying the importance of radiative smoothing and cloud clustering

As discussed in Section 3.2, both radiative smoothing and cloud clustering that increases interception by neighbouring clouds have been found to influence how 3D cloud-radiation interaction depends on cloud edge length. In order to derive the appropriate cloud edge input parameter for use in SPARTACUS for a given cloud field, we need to understand and account for these effects. We conduct experiments (described in Section 3.3.2) to separate the different effects of cloud clustering and radiative smoothing and determine the radiatively relevant edge length in a high-resolution 3D field of realistic cumulus by comparing SPARTACUS performance for different cloud geometry inputs to that of fully 3D radiation calculations. This analysis was published in Schäfer et al. (2016). The results provide guidance for the use of observations to quantify the cloud geometry variable needed by SPARTACUS when applied to realistic cloud fields.

3.3.1 Theory

SPARTACUS assumes that the flux between clear and cloudy regions is proportional to the length of the cloud edges in the horizontal plane. In Sections 2.2 and 2.3 of Chapter 2, it was found that this parametrisation works well for idealised clouds with smooth edges, such as cubes. We will see in this section that for realistic clouds with irregular edges finding the appropriate edge length for input in SPARTACUS is less straightforward, as using our parametrisation with cloud edge lengths measured in high-resolution

cloud fields overestimates the 3D effect. It appears that the "effective" cloud edge length for radiation is less than the measured cloud edge length, which we hypothesise is due to two effects:

1. *Radiative smoothing of irregular cloud edges.* Realistic cloud edge length is determined by cloud geometry on a range of scales from the overall cloud size down to the distance between cloud particles. In practical scenarios, we only have model or observation data down to a finite grid resolution, which is at best tens of meters, so some structure is missing. Cloud geometry is fractal, meaning that the measured edge length L is sensitive to small-scale features, and increases with decreasing grid spacing Δx as seen in Equation (3.1). On the other hand, due to the 3D radiative transport effects that we are including, the radiation fields are much smoother than the cloud water fields.

   In particular, small-scale concave features of the cloud edge are smoothed out in flux fields. For purposes of radiative transfer between cloudy and clear regions, these small concave features of cloud edge do not matter, because nearly all radiation emitted at these parts of the cloud edge will travel across the clear-sky area enclosed by the concave cloud edge and re-enter the cloud on the other side. As the horizontal extent of these features is much smaller than the depth of the cloud layer, the amount of radiation that travels vertically through them to escape at cloud top or base without being intercepted by cloud sides is negligible. Hence, the effective cloud edge length we are seeking should not include the added length contributed by these small concave features, but should instead follow the edge of an approximation to the cloud that is smooth and convex up to the same scale that the flux field is. In this case, approximating each cloud's cross section by a smooth convex shape that preserves as much as possible of the original geometry should be a good method to determine the radiatively relevant edge length: we know that the details that are smoothed out are not radiatively important, and further smoothing would not change these shapes (as long as separate clouds are not merged), so we know that this method provides both justified and sufficient smoothing.

   This effect explains why the assumption of flux $\propto L$ works well for idealised Euclidean clouds such as cubes with $D = 1$ in Chapter 2, but for realistic clouds at high resolution the measured edge length is higher than the radiative effective edge

length of the flux field, and hence using the measured edge length in the radiative transport parametrisation leads to an overestimation of the 3D transport.

2. *Cloud clustering.* Another effect that can reduce the impact of 3D radiative transport in cloud fields with multiple clouds is that radiation leaving the side of one cloud can be intercepted by another cloud. SPARTACUS allows this to happen, but assumes that the clouds are randomly spaced throughout the domain. In realistic cloud fields, groups of clouds may tend to cluster together, making the chance of radiation from one cloud's sides being intercepted by other clouds higher than if they were randomly spaced. Underestimating this reduction of 3D transport in SPARTACUS would add to the overestimation of 3D effects.

3.3.2 Experiments

In order to separate, quantify and account for these effects, we have designed a set of experiments based on a realistic LES simulation of shallow cumulus by Hinkelman et al. (2005), the same one as used for the broadband evaluation of SPARTACUS in Section 2.4, in a periodic domain of 6.4 km×6.4 km, with a resolution of 67 m in the horizontal and 40 m in the vertical and a realistic temperature profile taken from a radiosonde sounding at the Atmospheric Radiation Measurement (ARM) programs Southern Great Plains site in Oklahoma, USA (Hinkelman et al., 2005). In order to isolate cloud effects, we do not include atmospheric gases, aerosol or surface emission or reflection.

We start with the full cumulus cloud water field (depicted in Fig. 3.1a), centred within the domain. In order to clearly isolate differences due to treatment of 3D effects, we remove cloud internal inhomogeneity effects by assuming constant effective droplet radius throughout, and constant averaged liquid water content within each layer, making the 3D calculations directly comparable to SPARTACUS with two regions, clear and cloudy. We label the pixels belonging to each individual cloud in the cloud field using an algorithm based on the object labelling code of Stein et al. (2014). This algorithm considers two pixels to be part of the same object if they share an edge face, but not if they just share a corner. In Experiments a and c, we consider the full cloud field containing 55 clouds, showing the cloud clustering effect. For Experiments b and d, we select one isolated cumulus cloud and remove all others. Without neighbouring clouds there is no cloud clustering effect, allowing us to observe the radiative smoothing effect alone.

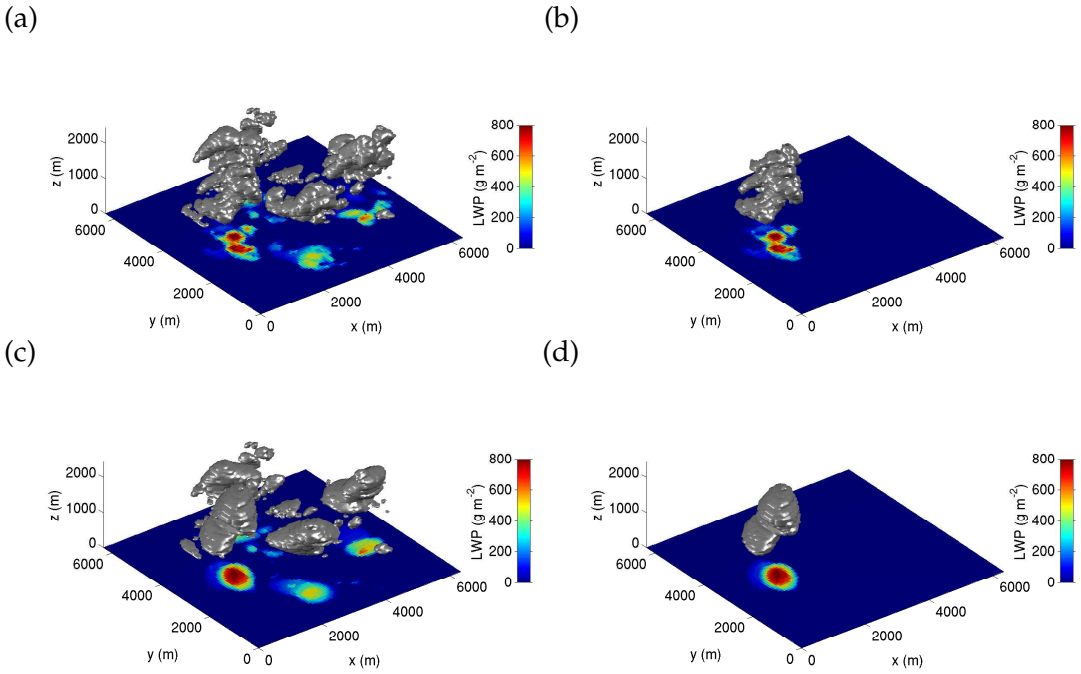

Figure 3.1: Cloud fields of the four experiments described in Section 3.3.2: (a) cumulus cloud field, (b) isolated cumulus cloud, (c) ellipsified cloud field, and (d) isolated ellipsified cloud. The grey shapes are 3D contours of cloud liquid water content larger than 0.001 g m^{-3}, while the colour field shown below is the liquid water path of each vertical column. The domain measures 6.4 km by 6.4 km, grid resolution is 67 m in the horizontal and 40 m in the vertical, and a realistic temperature profile based on a radiosonde sounding is used (Hinkelman et al., 2005).

We estimate the radiative smoothing effect by using two different cloud edge lengths as input for SPARTACUS: In Experiment a and b, we calculate the cloud edge length from high-resolution cloud contours, found by reducing the cloud field at each height to a 2D field of ones (cloud present) and zeros (no cloud present) and computing the length of the 0.5 contour. As these contours include cloud edge structure at scales likely too small to impact the radiation field, we expect an overestimation of 3D fluxes in SPARTACUS with this input, the radiative smoothing effect discussed in Section 3.3.1 (and in Experiment a also overestimation due to cloud clustering).

For Experiments c and d, we calculate the edge lengths by fitting an ellipse to each horizontal cross-section of each cloud of Experiments a and b respectively, using the method of Hogan et al. (2012), which ensures that the fitted ellipse preserves cross section area, horizontal aspect ratio between the ellipse half-axes a and b and orientation in the horizontal plane as much as possible given the finite pixel size. The method is illustrated in Figure 3.2, where the colour field shows the original cloud water distribution of part of our cloud field at height $z = 600\,\mathrm{m}$, and the red outlines show the ellipse ap-

proximation. The yellow arrows symbolise outward radiative fluxes from the cloud and show how radiative fluxes in small concave features of the cloud edge are intercepted by neighbouring parts of the cloud edge, while outward fluxes from convex parts of cloud edge travel into the clear region, a behaviour well described by outgoing fluxes from the cloud's convex ellipse approximation.

The field's ellipse cloud edge length is the sum of the exact ellipse perimeters of all the ellipses in each slice. We refer to this process as "ellipsification". The idea is to estimate the radiative effective cloud edge length for use in SPARTACUS by maintaining the largest-scale properties of cloud geometry, but excluding the influence of smaller-scale features irrelevant for radiation. Thus, the difference between SPARTACUS and MYS-

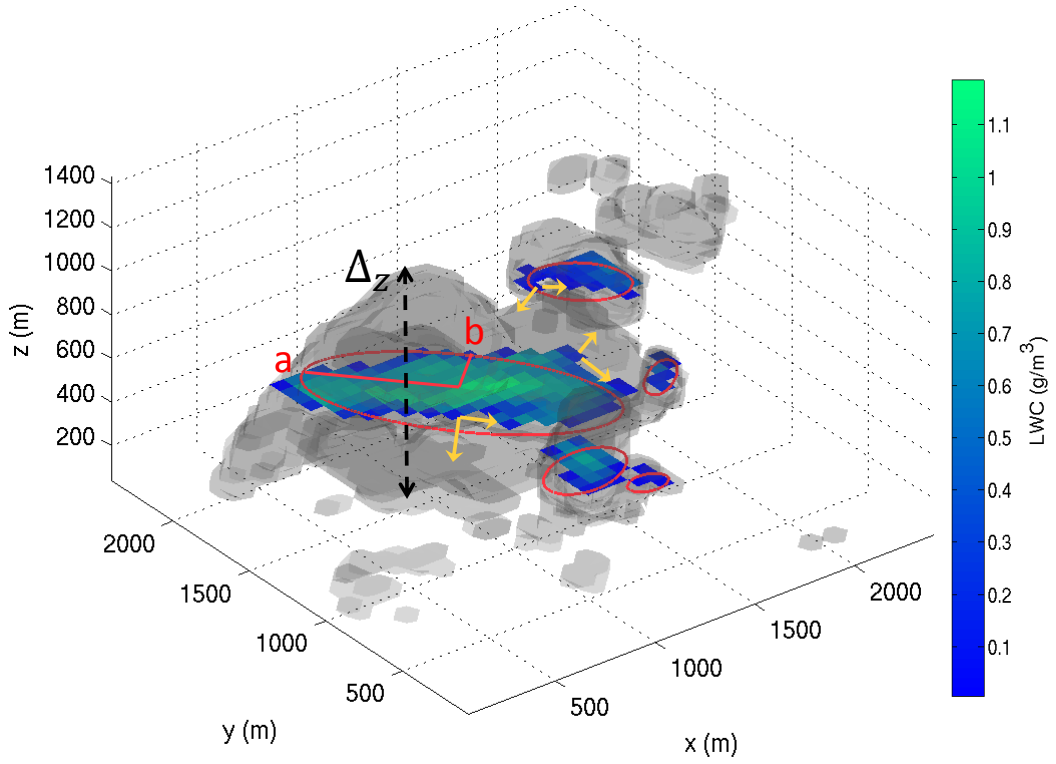

Figure 3.2: Approximation of horizontal cross sections of a cumulus liquid water field by ellipses. The grey contours show three-dimensional cloud outlines, while the blue and green coloured field shows the distribution of liquid water at height $z = 600\,\mathrm{m}$. The approximation of the clouds' outline by ellipses is shown in red. The yellow arrows symbolise radiative fluxes and illustrate how outward flux from a small-scale concave section of the cloud edge is intercepted by neighbouring parts of the cloud, while outward flux from the convex parts of the cloud edge travels into the clear region, the same behaviour as for outward flux from the convex ellipse cloud approximation. Δ_z denotes the vertical depth of the cloud layer, and a and b the half-axes of an ellipse.

TIC in Experiment c includes the cloud clustering effect but not the radiative smoothing effect, while Experiment d excludes both effects. Ellipse cloud edges are shorter than detailed contour cloud edges by a (vertically averaged) factor of 1.9 for the isolated cloud and 1.5 for the cloud field — the reduction is less for the full cloud field because it contains small clouds of only a few gridboxes, which do not show irregular features at the given resolution; therefore, ellipsification has less impact.

For each cloud field, we choose the optimum height-independent cloud overlap parameter for SPARTACUS's cloud overlap scheme (Shonk et al., 2010) so as to give the correct total cloud cover. We compare the results of SPARTACUS, including the edge flux parametrisation described in Section 2.3.3.3 and with the cloud edge length inputs discussed above, to fully 3D MYSTIC calculations for the original cloud field (Experiments a and c) and original isolated cumulus cloud (Experiments b and d), provided by Carolin Klinger and Bernhard Mayer.

3.3.3 Results for cloud geometry description

As seen in Figure 3.3, SPARTACUS's results agree well with MYSTIC in the 1D case (without horizontal transport). In 3D, MYSTIC and SPARTACUS with ellipse edge length agree well for the single cloud. When using contour edge length or in the presence of neighbouring clouds, the effects discussed in Section 3.3.1 lead SPARTACUS to overestimate the 3D flux. To test how representative this particular cloud is, we have run analogous single-cloud calculations for every cloud in the cloud field that is larger than four gridboxes, using SPARTACUS with ellipse edge length and MYSTIC. Figure 3.4 shows a comparison of the 3D factor $f_{\mathrm{1D\,correction}} = F^{\downarrow}_{\mathrm{3D}}/F^{\downarrow}_{\mathrm{1D}}$ at the surface between SPARTACUS and MYSTIC for each single cloud, where each symbol's colour indicates the cloud's total cloud cover. The two codes' results agree quite well, especially for the largest clouds in the field (in dark blue colours), which dominate the total cloud field results. The cloud selected for the single cloud experiment above is typical of these large clouds. For the smallest clouds (in pale cyan), results agree less closely due to numerical noise (the three clouds that show a 3D factor larger than 3 in MYSTIC are the three smallest clouds in the ensemble). The agreement between MYSTIC and ellipsified SPARTACUS in single-cloud cases confirms that SPARTACUS's overestimation of 3D effects for the full cumulus field is due to a combination of the two effects suggested in Section

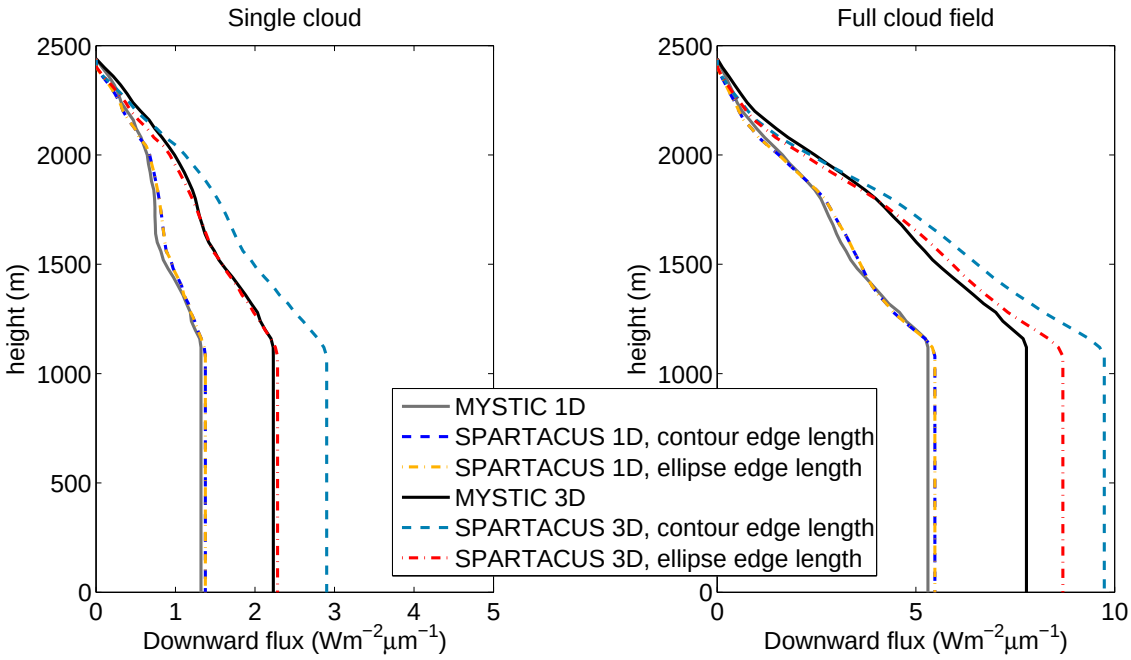

Figure 3.3: Downward domain-averaged monochromatic fluxes at wavelength $\lambda = 10.7\,\mu$m, from MYSTIC and from SPARTACUS using contour edge length, and ellipsified edge length. The left-hand figure shows profiles for the single-cloud case, the right-hand figure profiles for the whole cloud field. Note that in the 1D calculations, the cloud edge length does not matter, so the 1D profiles with contour edge length and ellipse edge length coincide.

3.3.1 and that our ellipsification method succeeds in removing the error due to small-scale irregular cloud edges. This is important: it suggests that for cumulus clouds, the *radiatively effective cloud edge length* is well represented by the perimeter of an ellipse fitted to the cloud edge at each height.

This still leaves the error caused by cloud clustering. To determine how clustered the cloud field is, we calculate the average horizontal distance between centres of mass of each cloud and its nearest neighbour $\overline{d_{\text{next}}}$, allowing for periodic boundary conditions at domain boundaries, as do the radiation calculations. In the full cloud field with 55 clouds, $\overline{d_{\text{next}}}$ is 276.4 m. Distributing the same number of clouds randomly in a domain of the same size results in a mean nearest neighbour distance of $\overline{d_{\text{next,rand}}} = 432.7\,\text{m}$ (averaged over 10^5 random distribution realisations to ensure representative sampling). This shows that in reality, our cloud field is significantly more clustered than in SPARTACUS's random distribution assumption, therefore intercepting more of the outgoing flux from cloud sides than SPARTACUS accounts for. We can compensate for this by reducing the cloud edge length and thereby also the cloud side flux. By running SPAR-

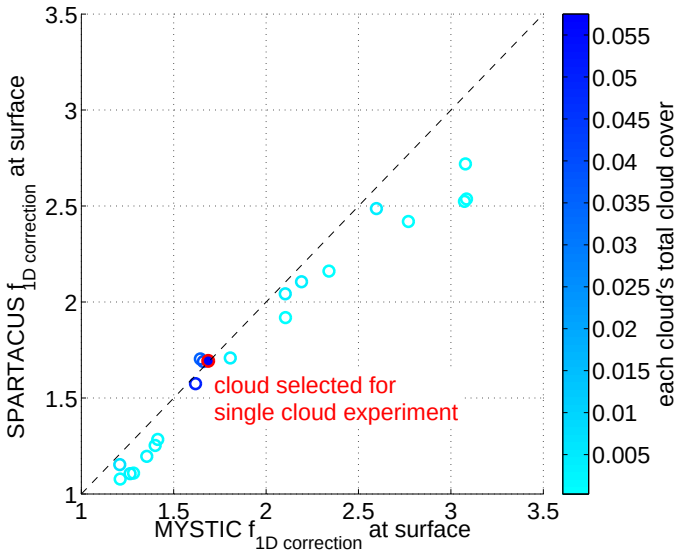

Figure 3.4: The 3D factor $f_{1\mathrm{D\ correction}} = F^{\downarrow}_{3\mathrm{D}}/F^{\downarrow}_{1\mathrm{D}}$ at the surface for the fluxes from each single cloud larger than four gridboxes in the cloud field, using SPARTACUS with ellipse cloud edge length, plotted against the same factor seen in MYSTIC results. The symbols' colours show each cloud's total cloud cover. The filled, red-edged symbol denotes the cloud used in the single cloud experiment discussed above. The 1-to-1 line is shown dashed in black.

TACUS repeatedly with a range of reduction factors, we can determine the optimum reduced edge length resulting in exact agreement between SPARTACUS and MYSTIC in each case. For the isolated cloud, without any cloud clustering to compensate, the optimum input edge length is about the ellipse edge length (at 0.94 times the ellipse edge length), while for the cloud field it is 0.69 times the ellipse edge length. This shows that using the ellipse edge length and multiplying by a factor of 0.69 to correct for clustering is a good estimate for the radiatively effective cloud edge length in this cumulus field. Further work would be needed to see how typical this value is for cumulus clouds and to determine the appropriate reduction factor depending on degree of clustering for any cloud type.

3.4 Describing cloud geometry in terms of an effective cloud scale

In order for SPARTACUS to represent cloud-radiation interaction as correctly but as simply as possible, we are looking to describe cloud geometry as relevant for radiation in as few variables as possible, and parametrise these depending on the quantities provided in a global model: cloud fraction and water content at each height, as well as the overlap

of clouds in different layers.

Since cloud side fluxes are expressed as proportional to cloud edge length in SPARTACUS (see Equations (2.2) and (2.8) in Chapter 2), this is the parameter we consider foremost. More precisely, we are interested in the ratio of cloud edge length to horizontal area of each region, as we use this as a description of the corresponding ratio of fluxes across the cloud boundary to vertical fluxes in the region. This ratio is also more likely than the perimeter itself to be independent of the choice of clouds to analyse in a given cloud scene (since the perimeter and area are correlated). Following Jensen et al. (2008), we can consider the "effective cloud diameter":

$$C_D = \frac{4 \sum_{\text{cloud } i} A_i}{\sum_{\text{cloud } i} p_i} = \frac{4 A_{\text{cloudy}}}{p}.$$

Here, A_i and p_i are the area and perimeter of the individual clouds in a gridbox, and A_{cloudy} is the total horizontal cloud area. The effective cloud diameter is a measure of the relation of cloud edge length to cloud area A_{cloudy}, as we desire. The parameters in SPARTACUS's radiative transfer equations (see Equation (2.2)) relate to C_D via $f_{\text{cloudy, clear}} = (\frac{1}{4} C_D)^{-1}$ and $f_{\text{clear, cloudy}} = (\frac{1}{p} - \frac{1}{4} C_D)^{-1}$. We can picture the effective cloud diameter in the following way: if the cloud field consisted entirely of cylinders of uniform radius, with the same ratio of edge length to cloud area as the actual field, the cylinders' diameter would be C_D.

However, while the effective cloud diameter gives a good measure of the ratio of cloud edge length to cloud area in one particular scene, it will vary between different cloud scenes, as it has been found observationally to depend on the cloud fraction (as seen in Jensen et al., 2008, Figure 6 a for marine boundary layer clouds observed with MODIS). The reason is that if the scene is either mostly clear or mostly covered with cloud, there is not much cloud edge - the highest amount of cloud edge is found in scenes that have similar amounts of cloud and clear sky, or a cloud fraction of around 0.5. This behaviour was illustrated by Morcrette (2012), who analysed cloud perimeter length for regularly and randomly spaced cloud elements depending on cloud fraction, and found a functional form to describe the dependence of perimeter length p on cloud fraction c_{cloudy} in both idealised and real cloud data, as shown in Figure 3.5, taken from Morcrette (2012).

Figure 3.5A shows examples of spatial distributions of regularly and randomly

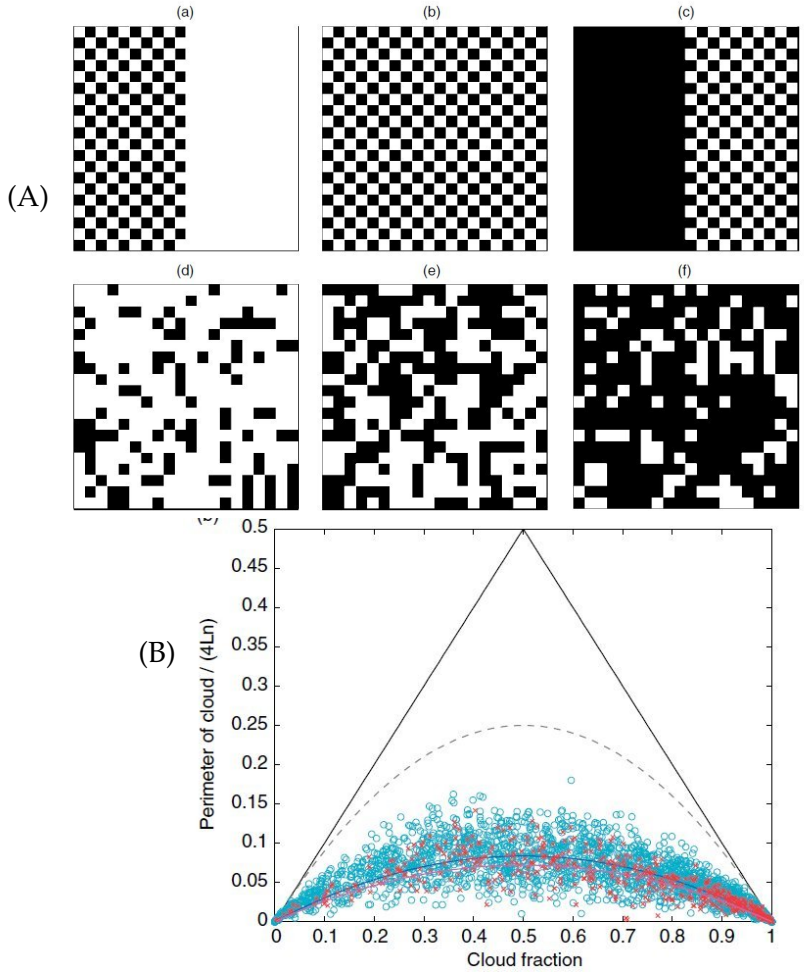

Figure 3.5: A) Idealised fields of cloudy sub-elements, arranged regularly so as to maximise perimeter in (a–c) and randomly in (d–f), for cloud fractions of 0.25 in (a, d), 0.5 in (b, e) and 0.75 in (c, f). B) Normalised cloud perimeter as a function of cloud fraction, for regular spacing (maximum possible perimeter; black solid line), random spacing (grey dashed line) and as seen in an analysis of Meteosat Second Generation cloud-mask images using $5^\circ \times 5^\circ$ scenes (red crosses and magenta line) and $2.5^\circ \times 2.5^\circ$ scenes (cyan circles and blue line). The normalised perimeter shown on the ordinate axis is the cloud perimeter p divided by 4 times the product of domain-side length (referred to as L) and number of grid boxes along each domain dimension n. This is equal to $\frac{p\Delta x}{4A_{domain}} = \frac{c_{\text{cloudy}}\Delta x}{C_D}$ in our notation, where Δx is the horizontal resolution, A_{domain} the domain's total horizontal area, c_{cloudy} the cloud fraction and C_D the effective cloud diameter. Both figures from Morcrette (2012).

spaced cloud sub-elements for several cloud fractions. Regular spacing is the distribution with maximum perimeter length for any given cloud fraction. Figure 3.5B shows the dependence of perimeter length p (normalised by 4 times the product of domain-side length L and number of grid boxes along each domain dimension n) on cloud fraction, in the idealised regular and random distributions and in an analysis of real clouds in Meteosat Second Generation (MSG) cloud mask scenes. It is clear that the cloud perime-

ter peaks at intermediate cloud fractions, that the regular distribution always has the longest total cloud perimeter, and that the real clouds' perimeter functional form closely follows that of the random distribution perimeter, albeit with a lower peak value - which might indicate either that individual clouds are on average larger than MSG pixels, or that the real cloud fields are more clustered than random.

The MSG cloud mask is based on infrared Spinning Enhanced Visible and Infrared Imager (SEVIRI) data. The resolution depends on where in SEVIRI's field of view a particular pixel is, ranging from 3 km at satellite nadir [1] to more than 11 km at the edges of the field of view. Average resolution is around 4 km for SEVIRI data and the MSG cloud mask [2]. The cloud mask describes horizontally projected total cloud cover, and includes all types of ice and water clouds.

The normalised perimeter plotted here is equal to $\frac{p\Delta x}{4A_{domain}} = \frac{c_{\text{cloudy}}\Delta x}{C_D}$ in our notation, where Δx is the horizontal resolution, A_{domain} the domain's total horizontal area, c_{cloudy} the cloud fraction and C_D the effective cloud diameter. Morcrette (2012) described the relationship of normalised perimeter to cloud fraction by

$$\frac{p\Delta x}{4A_{domain}} = \frac{c_{\text{cloudy}}\Delta x}{C_D} = \alpha c_{\text{cloudy}}(1 - c_{\text{cloudy}}), \tag{3.2}$$

and found a proportionality constant of $\alpha \approx 0.3$ for the total sample of different cloud scenes in the half-global snapshot he considered.

Knowing how cloud edge length and cloud effective diameter depend on cloud fraction, we can define a new variable, the typical *cloud scale*

$$C_S = (1 - c_{\text{cloudy}})C_D = \frac{4c_{\text{cloudy}}(1 - c_{\text{cloudy}})A_{domain}}{p} = \frac{\Delta x}{\alpha},$$

which should be independent of cloud fraction according to (3.2). We hope that this parameter only depends on the type of cloud and hence provides a simple way of estimating the length of the cloud edges in any cloud scene with known cloud type and cloud fraction. In Morcrette's data, the cloud scale is on average around 12–13 km (using the average MSG resolution for the calculation). However, the coarse and spatially variable resolution, the two-dimensional projection of clouds, the global averaging and the

[1] http://www.eumetsat.int/website/home/Data/MeteosatServices/0DegreeService/index.html
[2] https://climatedataguide.ucar.edu/climate-data/seviri-cloud-mask-dataset-very-high-resolution

mixture of different cloud types lead to significant uncertainty as to how representative this value is for cloud scenes of particular types on the scale of the gridboxes of global models.

For developing an idea of what cloud scales occur for different types of clouds, Michael Jensen and Andrew Vogelmann have provided us with a data set of cloud geometry parameters derived from globally distributed MODIS measurements of marine boundary layer clouds, at a resolution of 1 km in 38550 scenes of 300 km by 300 km (the same data set discussed by Jensen et al., 2008). We derive the normalised perimeter as defined by Morcrette (2012), the effective cloud diameter C_D, the proportionality constant α in Equation (3.2), and the cloud scale C_S. Jensen et al. (2008) attempted to capture the variation of effective cloud diameter C_D with cloud cover by separating their scenes into categories based on how organised the clouds were, but the functional dependence on cloud fraction in Equation (3.2) and the cloud fraction-independent effective cloud scale C_S offer a much more satisfactory description.

Figure 3.6 shows these cloud geometry parameters as a function of cloud fraction. We also calculated the best piecewise fit of the proportionality constant α and the effective cloud scale C_S, in cloud fraction intervals of 0.05 ranging from 0.3 to 0.9 (higher and lower cloud fractions are poorly sampled in this data set). As hoped, these parameters remain roughly constant with varying cloud fraction, at $\alpha \approx 0.1$ and $C_S \approx 10\,\text{km}$. The proportionality constant α depends on data resolution, therefore the cloud scale C_S is a much more useful value for comparison of cloud geometry between different data sets. As we will see in our detailed investigations of separate cloud types in Section 3.5, boundary layer clouds tend to be smaller, with a smaller effective cloud scale, than high ice clouds. It is therefore easily explained why the cloud scale C_S we find in Morcrette's data, which includes high clouds, is somewhat larger than than that found in Jensen et al.'s boundary layer cloud data, especially given the uncertainties in both cloud scale results due to limited resolution.

As far as we have seen so far, the cloud scale C_S seems to work excellently as a cloud fraction-independent parameter to characterise cloud geometry and cloud edge. However, all of the analyses discussed so far have been at fairly coarse resolutions, mixing different types of clouds, and on two-dimensional fields of total horizontal cloud cover, which adds uncertainty and precludes inclusion of small clouds and investigation of

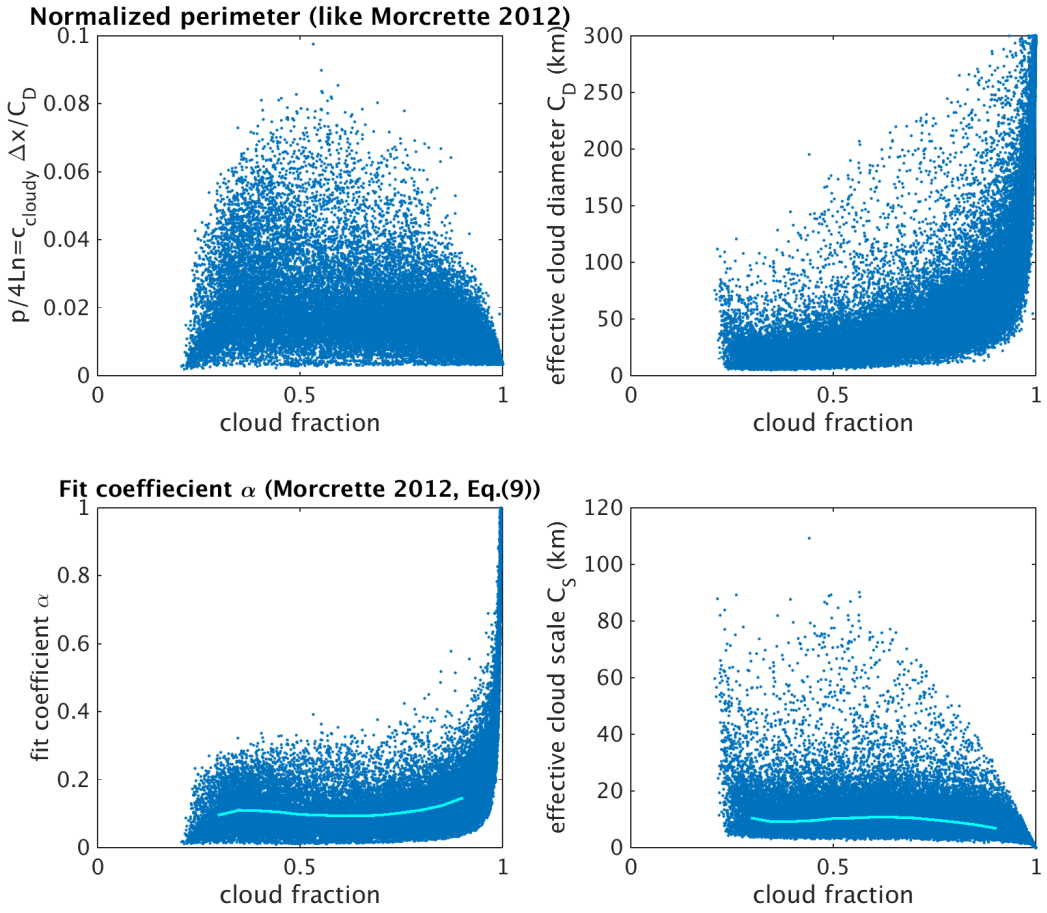

Figure 3.6: Geometry parameters for marine boundary layer clouds in Jensen et al.'s data set, as a function of cloud fraction. a) Normalised cloud perimeter, as defined in Morcrette (2012) b) Effective cloud diameter C_D. c) Proportionality constant α in Equation (3.2) d) Effective cloud scale C_S. The blue scattered dots show the values for each scene, the cyan lines in plots c) and d) show piecewise fits of the proportionality constant α and the cloud scale C_S.

how the parameter depends on cloud type and height. In order to obtain cloud scale values that we are confident represent the significant cloud types in the global atmosphere, we need more detailed investigation at higher resolution and at each height. We hence now turn to more high-resolution three-dimensional cloud fields of specific cloud types to analyse more exactly how the geometry parameters depend on cloud type and height, and what is the most appropriate spatial resolution to employ.

3.5 Analysis of 3D cloud fields

3.5.1 Cloud data sources

As the basis of our analysis, we use cases of high-resolution 3D cloud fields of different cloud types from a variety of sources, both large-eddy simulations (LES) and real-world scanning cloud radar observations.

3.5.1.1 LES cases

Using LES cases has a number of advantages: We can work directly with the cloud water fields, which are known to a high precision and at high and consistent spatial resolution. Some of the cases we investigate have also been used for previous studies of three-dimensional radiation, providing the possibility of comparing results. The drawback is that we have to trust that the simulations capture realistic cloud geometry adequately. Unlike the dynamical properties of LES simulations and some cloud statistics like the cloud size distribution that are often validated against observations (e.g. Neggers et al., 2003b), properties of three-dimensional cloud geometry are usually not (partly because high-resolution three-dimensional cloud observations are a relatively new development). Hence there remains some uncertainty on how realistic the three-dimensional geometry parameters derived only from the simulations are — which is why we include both LES cloud fields and radar observations in our study. Future, more extended studies including more 3D observations could further reduce uncertainty in LES cloud geometry.

3.5.1.2 Cloud radar observations

Observations from a scanning cloud radar can provide us with real three-dimensional cloud observations, a great opportunity to study true cloud geometry, and also to judge how well it is represented in LES simulations. However, as a real measurement, these data also present some uncertainties: the finite sensitivity of the radar means we always miss some clouds. As the radar's sensitivity to droplets varies with their diameter D like D^6, any rain or drizzle dominates the radar signal, and attenuation by moderate or heavy rain degrades the radar's sensitivity. In order to avoid these problems, we restrict

ourselves to non-raining cases here.

The spatial resolution of the measurements is unevenly distributed in three-dimensional space, depending on the scanning pattern we choose and on wind speed, and the largest gaps can be relatively coarse. Fielding et al. (2013) discussed a variety of possible scanning patterns (illustrated in Fielding et al., 2013, Figure 2). They concluded that the errors are lowest for "plan position indicator" scans (a sequence of scans over azimuth angles at constant heights; PPI) for low winds and for cross-wind "range height indicator" (RHI) scans (horizon-to-horizon scans through elevation angles at constant azimuth in a plane perpendicular to the wind, while the clouds move across the field of view with the wind) for higher winds. PPI biases are higher for all wind speeds if the air mass is polluted, and hence the cloud droplets small. Spatial resolution is easier to estimate with the cross-wind RHI scanning pattern, where the movements of the radar and of the clouds are perpendicular to each other. In this case, the coarsest spatial resolution occurs between subsequent turning points on one side of the scanning plane, and is estimated as the time needed for the back-and-forth scan t, which is 360° divided by the radar's scanning speed (in degrees per second), multiplied by the wind speed.

We choose a cross-wind RHI scanning pattern for the observations, because of the lower errors at high wind speeds, because resolution and hence interpolation errors are easier to estimate and because executing a high-resolution PPI scan at realistic radar scanning rates can take up to 15-20 minutes. Small cumulus clouds (which are important for our study, as 3D cloud radiation effects are most important in broken cloud fields, and these are the most commonly occurring broken clouds) can easily develop or disperse in that time span. While the clouds also change during the course of cross-wind scanning, in that case areas of the cloud field that are close together in space will be scanned at closer times than in the case of PPI scanning, which makes it more likely that any single cloud will be scanned completely before it has evolved too much.

Mark Fielding has provided a case of scanning cloud radar data from the ARM site at the Azores. Table 3.1 summarises the properties of the instrument. The data have been interpolated according to the method described by Fielding et al. (2013) onto a regular spatial grid with resolution 50 m.

Location	Azores
Frequency	95.04 GHz
Wavelength	3.17 mm
Pulse repetition frequency	7.4 kHz
Antenna beam width	0.37°
Maximum sensitivity at 1 km	−37.5 dBZ

Table 3.1: Specifications of radar instrument at ARM Azores site (adapted from Fielding, 2014).

3.5.2 Analysis methods

As discussed in Section 3.2, we need to account for radiative smoothing in order to find the edge length relevant for radiation, which helps to decide on the most appropriate scale for the edge length measurement. In the investigation of the most appropriate measure of cloud edge length in Section 3.3, we found that in order to derive the correct *radiatively relevant cloud edge length* as seen by radiative fluxes, we need to correctly account for radiative smoothing by smoothing high-resolution data at scales up to the scale of radiative smoothing η_{rad}. As we have seen in Section 3.3, for cumulus cloud fields at low cloud fractions, approximating each cloud's cross section in each layer by a smooth convex shape (we use ellipses), gives a good measure of the reduced cloud edge length for radiation due to radiative smoothing.

Our ellipsification method for the cumulus cases labels any cloudy gridboxes that share a face in 3D as part of the same cloud (but not if they only share a corner). This method works well for cumulus cloud scenes with one reasonably distinct cloud layer. In multi-layer cloud fields, the method can sometimes lead to unexpected results if clouds of several types and vertical extensions touch in one layer, as they are then regarded as the same cloud, an effect that is exacerbated if cloud fraction is high and spatial resolution is too coarse to show small separations between different clouds. This is why in cases with those characteristics (where ellipsification does not give very appropriate results for radiative effective cloud edge anyway, and is only computed as a comparison) we use layerwise labelling and ellipsification in 2D instead. Again, two gridboxes in the same layer are counted as part of the same cloud if they share an edge, but not if they only share a corner. Some of the cloud cases we investigate also have a very high number of very small clouds — if we counted these all as separate clouds for the determination of

ellipse cloud edge length, they would dominate the resulting edge length, but this is not appropriate since these small clouds contribution to total cloud emission (or scattering) is quite small. This effect becomes even stronger when 2D labelling and ellipsification is used, as fewer clouds are joined up, and therefore more very small clouds are counted. In cloud scenes where this effect would distort the results, we only consider clouds over a chosen minimum size in the calculation of ellipse cloud edge length. We perform both 3D and 2D ellipsification for the cumulus cases, to show that in these scenes results agree closely between the two methods.

Broken cumulus fields are typically composed of small clouds of horizontal extent from less than 100 m up to 1-2 km, with largely convex horizontal cross sections and concave parts of the clouds edge that are usually less than 150 m across. Ellipses are a good approximation for the smoothed shape of these clouds as seen by radiative fluxes, because the concave features eliminated in the ellipses are of a size below the radiative smoothing scale, and since the original cloud shape is close to convex, the large-scale geometry is preserved. This approach is less viable for other cloud types whose shapes are less well described as isolated convex objects, such as near-overcast clouds. So, we need a more general method for determining the radiatively relevant cloud edge length.

As discussed in Section 3.2, the difference between high-resolution measured cloud edge length and radiatively effective cloud edge length is that radiative smoothing eliminates details of the cloud water distribution smaller than the critical "radiative smoothing scale" η_{rad} in radiation fields, and that radiative transport is determined by the edges of the smoother field. Studies on scale breaks in Fourier fractal statistics of Landsat images discussed in Section 3.2 find radiative smoothing at scales smaller than $\eta_{rad} \approx 200$ to 400 m (Davis et al., 1997); at larger scales, the scale statistics of radiative and physical cloud properties look very similar. This suggests that smoothing to a scale of about 200 m in order to measure the radiatively relevant cloud edge length is appropriate, at least for clouds similar to those in the Landsat images (small tropical cumulus and stratocumulus). We can account for this effect by smoothing the cloud water field through mathematical convolution with a smoothing kernel $s(x, y)$ before determining the edge length: if $w(x, y)$ is the function describing the water content at each point of the hori-

zontal cross section, the smoothed convolved field is

$$w_{conv}(x,y) = w(x,y) * s(x,y) = \int\int w(x',y') \cdot s(x-x', y-y')dx'dy',$$

where "$*$" denotes convolution. We use a smoothing kernel of Gaussian shape: $s(x,y) = \exp(-\frac{x^2+y^2}{2\sigma^2})$, with standard deviation $\sigma > 0$. The convolution is executed in Fourier space, extending the cloud field with zeroes and then truncating the result to the original size so as to avoid contamination of one side of the domain with values from the other side by the Fourier transformation's inherent assumption of periodicity.

The cloud edge length is determined as the length of contours of $w_{conv}(x,y)$ at a contour value t_{cont} chosen so that the area in the contours (the cloud area in the smoothed field) is equal to the layer's original cloud area. This means that scales smaller than the width of the smoothing kernel at the height of the contouring threshold are smoothed. The largest scale at which detail is completely smoothed is the distance from each chosen point within which lie the values that dominate the smoothed field at that point - this is somewhat smaller than the standard deviation, which describes the *mean* distance of data points that contribute to the smoothed field values from the central point. The standard deviation describes the mean scale of smoothing. As we intend the smoothing process to represent radiative smoothing, the standard deviation σ should be equal to around half the radiative smoothing scale η_{rad} of 200 m to 400 m (which, as found by Marshak et al. (1995) and Davis et al. (1997), is about 2 to 3 times the mean displacement width of radiation through radiative smoothing). We would therefore expect smoothing with a Gaussian kernel with standard deviation σ between 70 m and 200 m to best represent radiative smoothing.

This convolution method to represent radiative smoothing is somewhat similar to that of the Nonlocal Independent Pixel Approximation of Marshak et al. (1998) and Marshak et al. (1995), an approximate method to account for radiative smoothing in radiance fields calculated with the Independent Pixel Approximation. This method represents radiative smoothing by convolving the resulting radiance fields with a smoothing kernel of Gaussian shape. Our algorithm differs in that we smooth not the radiation results but the cloud water field from which we determine the radiative cloud edge length, but as this edge length is proportional to the flux between clouds and clear sky in our formulation, the effect extends to the radiative flux distribution. Both methods hence follow the

same idea, although implemented for very different radiation schemes.

With the convolution method, we can calculate radiative effective cloud edge length for any cloud field. The results depend on the choice of standard deviation σ. We conduct sensitivity tests with a range of standard deviations to see which choice produces effective edge lengths that agree best with the results of the ellipse method for cumulus clouds, where we established in Section 3.3 that ellipse approximations were a good estimate of the radiative effective edge length. We also compare the corresponding smoothing scales to radiative smoothing scales reported in the literature. Some uncertainty in the approach and the best standard deviation to choose remains and leads to uncertainty in the resulting values of cloud edge length and cloud scale.

Neither the ellipse nor the convolution method compensates for enhanced interception of radiation by separate neighbouring clouds that is determined by how clustered the clouds are. We account for this effect in a separate step. Since a detailed investigation of cloud clustering is outside the scope of this thesis, we adjust for cloud clustering by reducing the effective cloud edge length by a factor of 0.7, as derived in Section 3.3 for the I3RC cumulus cloud scene, and correspondingly increasing effective cloud scale. This ad-hoc adjustment based on one cloud scene introduces some uncertainty, since it is not clear how representative it is for other cloud fields, especially of different cloud type. Further work would be needed to represent typical degrees of cloud clustering and their effect on effective cloud edge length in a more rigorous manner. Meanwhile, we include this uncertainty due to the clustering treatment in the uncertainty range of our effective cloud scale estimates. We will represent these uncertainties in our global experiments in Chapter 4.

3.5.3 Cloud cases and results

3.5.3.1 Cumulus

We first test the two radiative edge length calculation methods for two cumulus cases, one of LES data and one of cloud radar data. The LES cumulus scene is one of two cases of liquid water boundary layer clouds that were used in Phase II of the International Intercomparison of 3D Radiation Codes (I3RC; Cahalan et al., 2005), a simulation of continental shallow cumulus at the ARM Southern Great Plains site in Oklahoma, provided

to the I3RC by Laura Hinkelman and described in Hinkelman et al. (2005). This is the same case we used for evaluation of SPARTACUS and the ellipse cloud edge length in Sections 2.4 and 3.3. For our analysis, we exclude the duplicated rows and columns provided for periodic boundary conditions, and centre the domain on the clouds so as to avoid clouds intercepting the domain boundaries. The cloud field has a domain size of 6.4 km×6.4 km×2.44 km once duplicated rows and columns at horizontal boundaries used to create the simulation's horizontal periodic boundary conditions are excluded (6.67 km×6.67 km×2.44 km if all rows and columns are included). The cloud layer is located between heights of $z = 1.02$ km and $z = 2.44$ km, the horizontal resolution is 66.7 m and the vertical resolution is 40 m in the cloud layer.

Our second cumulus case is a cloud field observed by a scanning cloud radar at an ARM observation site deployed in the Azores on 21st November 2009 at 14:20 UTC. The details of the radar instrument, scanning pattern and interpolation method are discussed in Section 3.5.1. The data has been interpolated onto a regular grid with a resolution of 50 m in both the horizontal and the vertical, in a domain of size 5.05 km×5.05 km×3 km

As horizontal resolution in these cases of $\Delta x = 66.7$ m and $\Delta x = 50$ m respectively is below both the size of the clouds and the critical scale for radiative smoothing, using high-precision contour edge length instead of radiative effective edge length leads to a sizeable overestimation of the 3D effects (seen in Figure 3.3). Comparison of flux fields and liquid water fields as well as comparison of radiation results for various edge length inputs with fully 3D Monte Carlo results in Section 3.3.3 have shown that approximating each cloud's cross section in each layer by an ellipse (thus assuming convex clouds) provides a good estimate of the effective edge length for cumulus clouds. We also perform the convolution edge length calculation for a range of smoothing kernel widths ranging from from $\sigma = 50$ m to $\sigma = 500$ m (representing the largest spread we consider plausible) with one additional calculation at $\sigma = 1$ km to approximate how the results might change if seen at coarse resolutions like that of MODIS, in order to estimate the sensitivity and uncertainty range of the results, and compare the resulting edge lengths and cloud scales to those of the ellipse method.

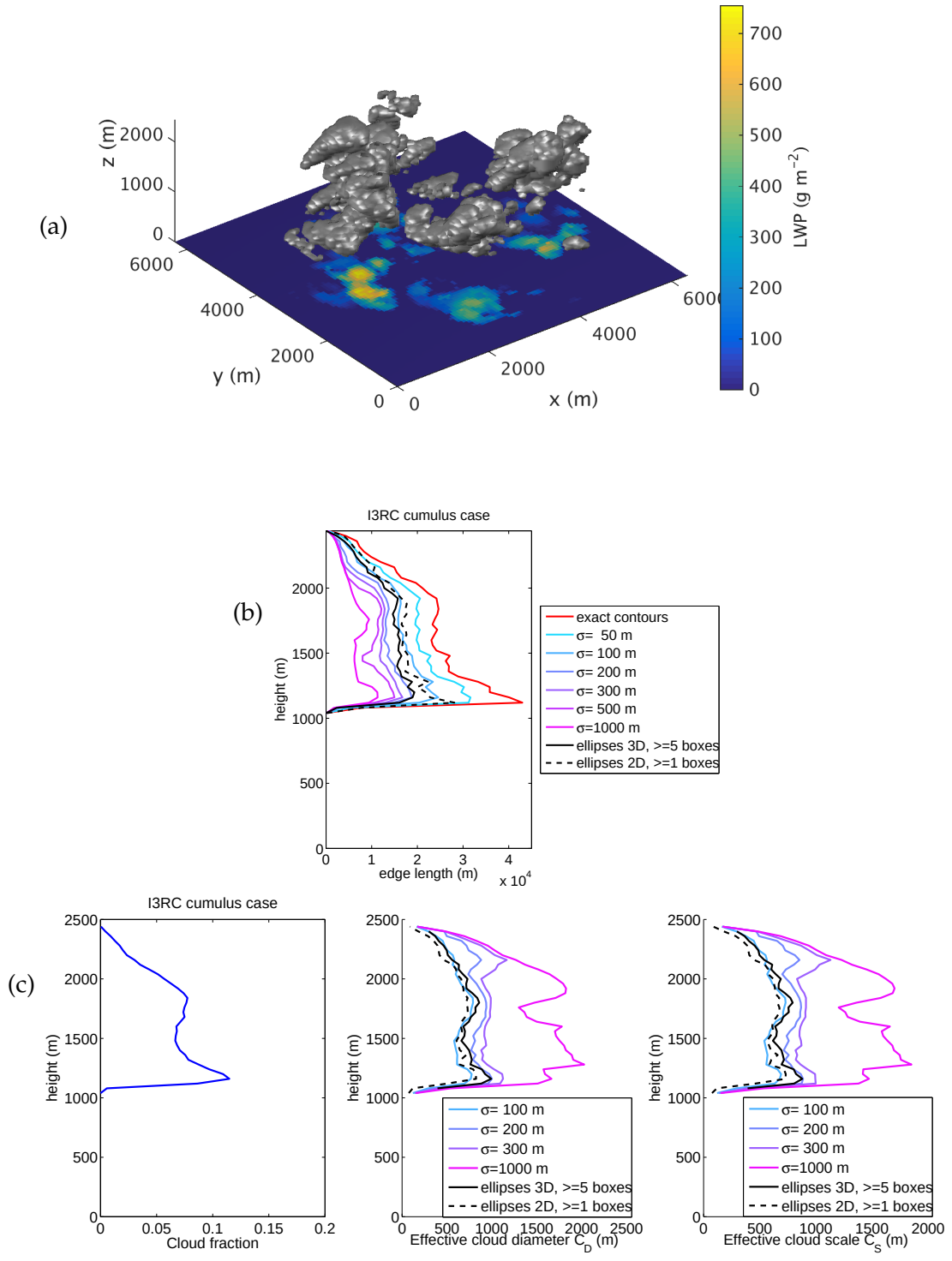

Figure 3.7: Cloud geometry of the I3RC cumulus field, centred on the clouds. a) Three-dimensional outlines (grey contours) of cloud liquid water over a threshold of 0.001 g m^{-3} with a colour plot of each column's liquid water path shown underneath. b) Height profile of cloud edge length in each layer as computed by simply contouring the original cloud water field, with the convolution method with various smoothing kernel standard deviations σ, and with the ellipse method. c) Cloud edge parameters calculated with the same methods (results are shown for a selection of smoothing kernel standard deviations). Total cloud cover in this case is 0.23.

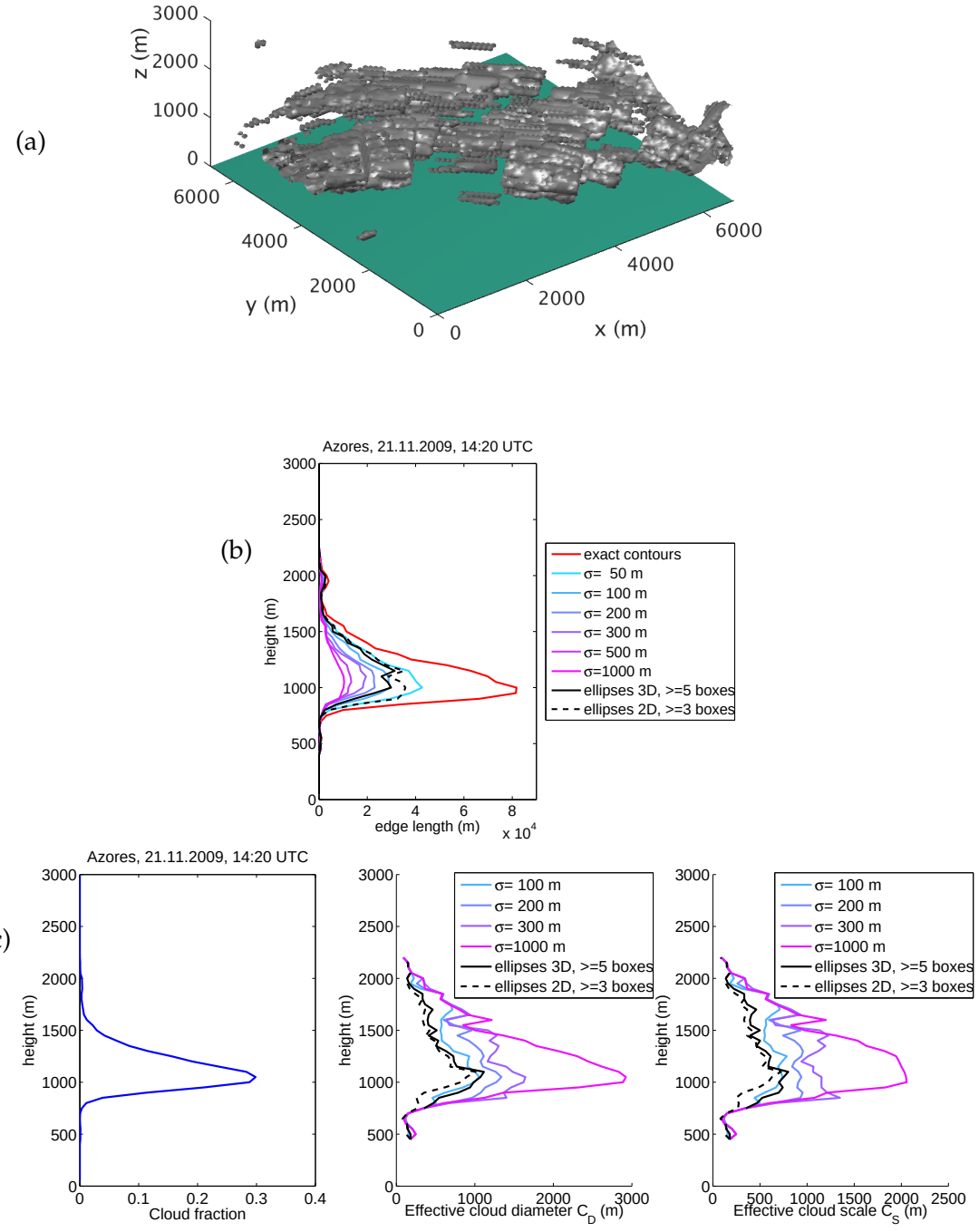

Figure 3.8: As in Figure 3.7, for the cumulus cloud field from the Azores scanning cloud radar, except that the cloud field investigated is of radar reflectivity instead of liquid water. The three-dimensional outlines (grey contours) in Panel a) show radar reflectivity over a threshold of -50 dBZ and no liquid water path is plotted. Only clouds that contain at least 5 grid boxes are considered in this analysis. Total cloud cover in this case is 0.45.

Figures 3.7 and 3.8 show the cloud fields and the cloud geometry variables computed with our different methods, as well as by simply contouring the original cloud fields, in the two cumulus cases. The cloud fields investigated are liquid water in the I3RC LES case and radar reflectivity in the Azores case. As the Azores cloud field contains a huge number (nearly 600) of tiny clouds of less than 5 grid boxes that are too optically thin to have much impact on radiation, we have restricted analysis to clouds of at least 5 grid boxes in this case.

Profiles of geometry parameters in both cases show reasonable agreement between the ellipse method and the convolution method with $\sigma = 100\,\mathrm{m}$ at most heights. Neither effective cloud diameter nor effective cloud scale C_S are exactly constant with height, but peak in the layers with most cloud (which is to be expected, as clouds in marginal layers tend to be very small). These are the layers most important for the radiation calculation, as they also contain the highest cloud water content and optical depth; and the sample of cloud shapes is most representative in these layers. We therefore weight our estimate of typical C_D and C_S for each cloud field towards the most cloudy layers. C_S is roughly constant in those layers.

In order to determine more precisely at which smoothing kernel width the convolution method agrees best with the ellipse method, we have plotted height-averaged 3D labelling ellipse and convolution cloud edge lengths for a range of smoothing kernel widths for the two cumulus cases against the smoothing kernel standard deviation σ in Figure 3.9. Height averaging was done using both cloud-fraction weighted and linear averaging. While the height-averaged value of cloud edge length depends on the averaging method (as we would expect), the smoothing kernel width at which ellipse and convolution cloud edges coincide barely changes. This occurs for a convolution smoothing scale of $\sigma \approx 100\,\mathrm{m}$ in the Azores case and $\sigma \approx 150\,\mathrm{m}$ in the I3RC case. These smoothing kernel standard deviations corresponds to a radiative smoothing scale η_{rad} of 200 m to 450 m, which agrees with the radiative smoothing scale of 200 m to 400 m found for stratocumulus in the literature. This indicates that a standard deviation σ between 100 m and 150 m is an appropriate smoothing kernel width for high-resolution fields of boundary layer clouds.

This analysis did not include any effects of cloud clustering, which decrease the effective edge length and correspond to a smoother field (a larger smoothing scale). We

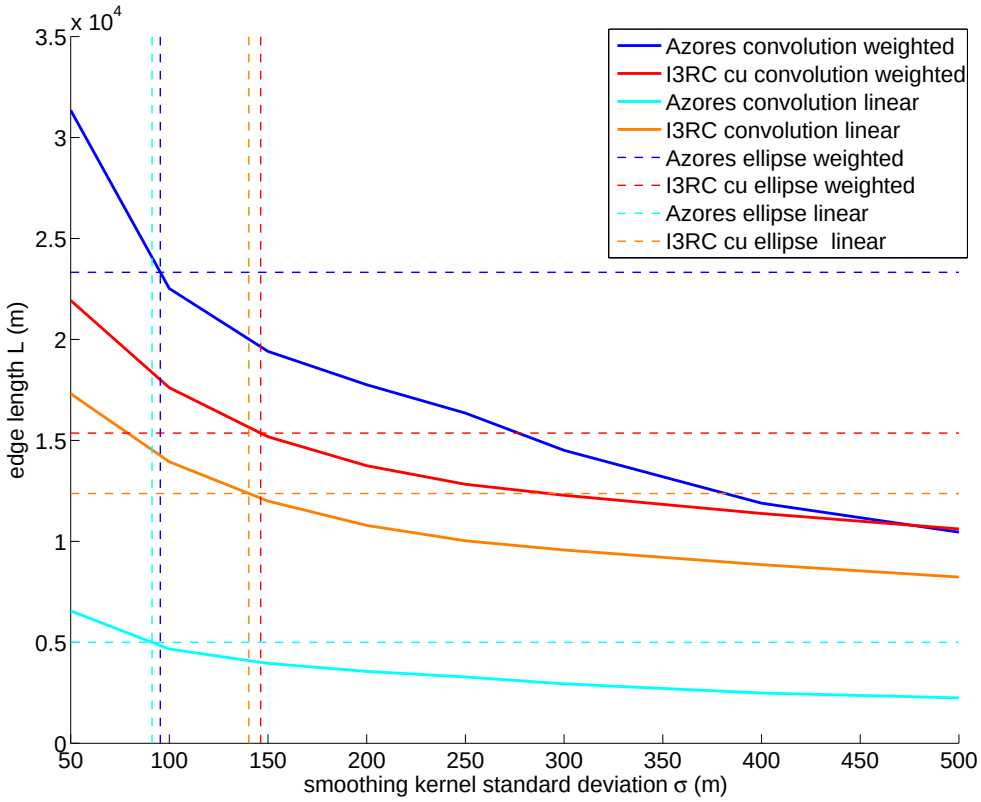

Figure 3.9: Height-averaged cloud edge lengths resulting from the convolution and 3D labelling ellipse methods, plotted against standard deviation of the smoothing kernel, for the I3RC LES and Azores scanning cloud radar cumulus cases, using both cloud fraction-weighted and linear averaging between vertical layers. The vertical lines indicate the smoothing kernel standard deviation for which convolution kernel edge length and ellipse edge length coincide for each case, which is around $\sigma = 100$ m in the Azores case and $\sigma = 150$ m in the I3RC case.

account for this effect by applying an empirical clustering reduction to effective cloud edge length, a method that includes some uncertainty. Hence, in order to ensure we do not overestimate 3D effects, we should represent cloud scale results at somewhat larger smoothing kernel width, as well as the general uncertainty inherent in our cloud scale derivation. Cloud scale results at smoothing kernel widths $\sigma = 100$ m, $\sigma = 200$ m and $\sigma = 300$ m should provide an appropriate uncertainty range of cloud geometry, leaning toward conservative estimates of 3D effects.

In spite of the different meteorological conditions of the two cloud fields (continental versus maritime cumulus), the different sources (simulation versus cloud radar observations), the different cloud fields we have used (liquid water versus radar reflectivity) and the different total cloud cover, the effective cloud scales (of the most cloudy layers and for $\sigma = 200$ m) are remarkably similar, at $C_S \approx 800$ m in the I3RC case and $C_S \approx 900$ m

in the Azores case. This suggests that in the effective cloud scale we have successfully found a geometry parameter that describes the amount of radiatively relevant cloud edge length in a cloud field and does not depend on cloud fraction or the specifics of each cloud scene, but only on the cloud type. The uncertainty range in cloud scale C_S due to the different smoothing kernel widths we consider is ± 200 m, again similar for the two cases in spite of the differences in cloud structure. Analysis of more cumulus cases in future would be beneficial to reduce the uncertainty of the results. In this work, we represent that uncertainty by repeating the convolution edge length calculations in each case with a range of smoothing kernel widths.

Having determined a convolution smoothing kernel width that agrees both with the results of the ellipse method and with literature values of the radiative smoothing scale, the convolution method provides us with a working method to determine radiative effective cloud edge length that does not require that cloud fraction is low and that the clouds are small and distinct from each other, like the ellipse approximation. We can now apply this method to cloud scenes of other cloud types.

3.5.3.2 Stratocumulus

We next apply the convolution method to stratocumulus cloud scenes. Here, the ellipse method breaks down as isolated convex clouds are no longer a good approximation of the cloud field, but we still calculate ellipse edge lengths for comparison. We investigate the second cloud case used in I3RC, a scene of night-time maritime stratocumulus case simulated by Moeng et al. (1996) in conditions based on observations off the coast of California (Duda et al., 1991). The domain size is $3.5\,\text{km} \times 3.5\,\text{km} \times 0.79\,\text{km}$, with the cloudy layer between $z = 0.41$ km and $z = 0.79$ km height, the horizontal resolution is 55 m and the vertical resolution 25 m in the cloud layer.

Figure 3.10 shows the cloud field and the cloud geometry variables computed with the different methods. Effective cloud scale C_S is more nearly constant with height than in the cumulus cases, and peaks at a similar value of $C_S \approx 700\,\text{m} \pm 200\,\text{m}$. This is an encouraging result, as it implies that in the parametrisation of cloud geometry through effective cloud scale we are aiming at, we may not need to divide shallow boundary layer cloud into cumulus and stratocumulus, as similar values of $C_S = 0.7$ to 1.0 km hold for both.

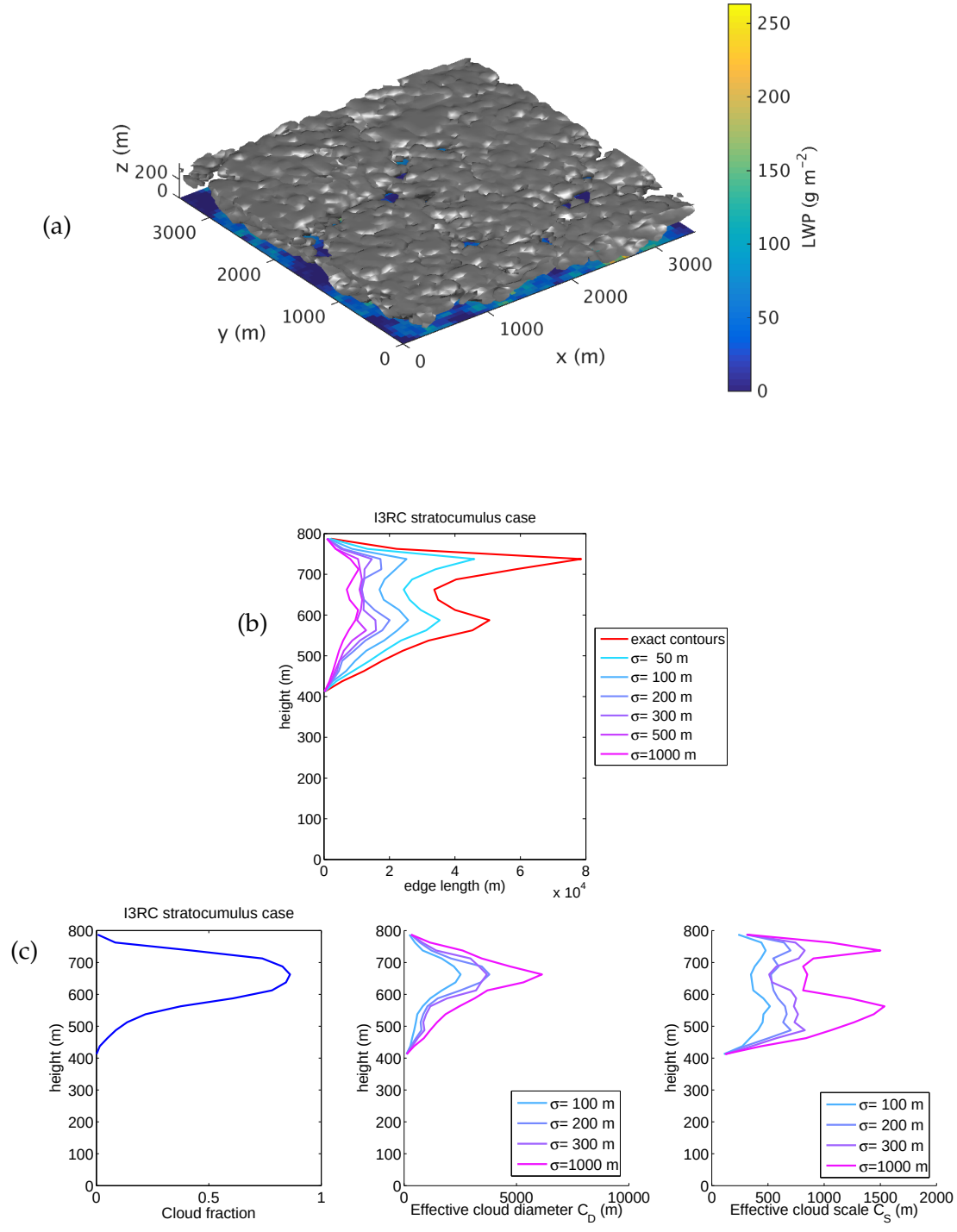

Figure 3.10: As in Figure 3.7, for the I3RC marine stratocumulus field. Total cloud cover in this case is 0.92.

However, the cloud scale values for both cumulus and stratocumulus we find are starkly different from the cloud scale of C_S =10 km seen for marine boundary layer clouds in Jensen et al.'s data set investigated in Section 3.4. This is explained by the fact that much of the cloud structure retained even in our smoothed cloud field is not resolved at the coarse MODIS resolution of 1 km, much larger than both our smoothing scale and the resolution of the cloud-resolving model or cloud radar. The scenes are also much larger than our 3D cases, at 300 km$\times$300 km. Both these effects increase the average cloud size (coarse resolution increases the minimum cloud size and large domain size the maximum cloud size). The clouds may also appear larger in the MODIS data because it is an analysis of two-dimensional horizontally projected cloud cover — so clouds that are separate in three dimensions can appear joined. All these increases in average cloud size decrease the amount of cloud edge per cloud area, and increase the effective diameter C_D and the cloud scale C_S. As many of the marine boundary layer clouds considered are at heights of less than 1 km above the ocean, cloud structure at scales below 1 km will likely have an impact on the surface radiation, so the cloud geometry parameters derived from high-resolution 3D cloud fields should yield more exact radiation results than those derived from MODIS data.

Figures 3.7 to 3.10 also show results for our fields when smoothed with a very large smoothing kernel with standard deviation $\sigma = 1$ km. This is still somewhat less smooth than if the field's original resolution was 1 km, but gives a first impression of results when the fields are smoothed to the order of magnitude of MODIS resolution. We see a marked increase in cloud scales C_S, though they are still lower than the $C_S = 10$ km seen in Jensen et al.'s MODIS data. This might be because smoothing does not represent the full effect of coarsening resolution, and we have not represented the merging effect when projected two-dimensional cloud fields are analysed. It is also possible that the LES stratocumulus case we consider here does not represent the full range of stratocumulus clouds in nature. More investigation of different cases would be needed to clarify this issue, and put the results on a better statistical basis. We will represent the uncertainty in our global experiments in Chapter 4 by including an experiment run using an input cloud scale value of $C_S = 10$ km as in Jensen et al.'s data for boundary layer clouds.

3.5.3.3 Cumulonimbus

We consider a cumulonimbus case provided by Tobias Zinner at Ludwig-Maximilians-University Munich (LMU) and by Stephen Lang and Dr. Wei-Kuo Tao at NASA Goddard Space Flight Center (GSFC) and discussed in Zinner et al. (2008). The simulation was done with the Goddard Cumulus Ensemble cloud-resolving model (Tao and Simpson, 1993; Tao et al., 2003) that provides 3D fields of cloud properties. This case has a somewhat coarser resolution than the previous LES cases: $\Delta x = 250\,\mathrm{m}$ in the horizontal and 200 m in the vertical within the cloud layer. The domain is also larger, at $64\,\mathrm{km} \times 64\,\mathrm{km} \times 117.5\,\mathrm{km}$ in order to accommodate the whole anvil. Clouds extend up to $z = 18\,\mathrm{km}$. The scene contains both water and ice, which we analyse both separately and together, and has three distinct cloud layers, allowing analysis of mixed-type cloud geometry: a layer of small cumulus below $z = 5\,\mathrm{km}$, a layer of mixed-phase stratiform stratocumulus between $z = 5\,\mathrm{km}$ and $z = 8\,\mathrm{km}$ and the cumulonimbus convection cores and anvil reaching from $z = 5\,\mathrm{km}$ to $z = 18\,\mathrm{km}$.

In the stratiform layer, this field contains a high fraction of grid boxes with very low water content. As these have negligible optical depth (and also may be an artefact of the simulation that generated the cloud field), we choose not to consider them in our analysis, and impose a minimum cloud water content threshold of $0.001\,\mathrm{g\,m^{-3}}$. This reduces the maximum cloud fraction in this layer to 0.35 (from 0.74 if we consider every grid box with positive water content as cloudy — a higher threshold of $0.01\,\mathrm{g\,m^{-3}}$ would reduce the maximum cloud fraction even further to 0.17). For comparison, we have calculated geometry parameters with the ellipse method, although this method is only really appropriate for those parts of the cloud field that are well approximated by single convex clouds: the boundary layer cumulus, the convective cores where they do not merge with the stratiform layer and the anvil. We use cloud labelling in each layer separately for this case, so as to avoid merging clouds of different extent and type that may touch in just one of the layers.

Figure 3.11 shows the cloud field and the cloud geometry variables for the full cloud field (containing both water and ice). The separate results for liquid water and ice are similar (not shown here). In the small cumulus layer below $z = 5\,\mathrm{km}$, the cloud scale C_S is larger than in the boundary layer cases previously considered, at $C_S \approx 2\,\mathrm{km} \pm 200\,\mathrm{m}$. This is to be expected as a result of the larger domain and coarser model resolution.

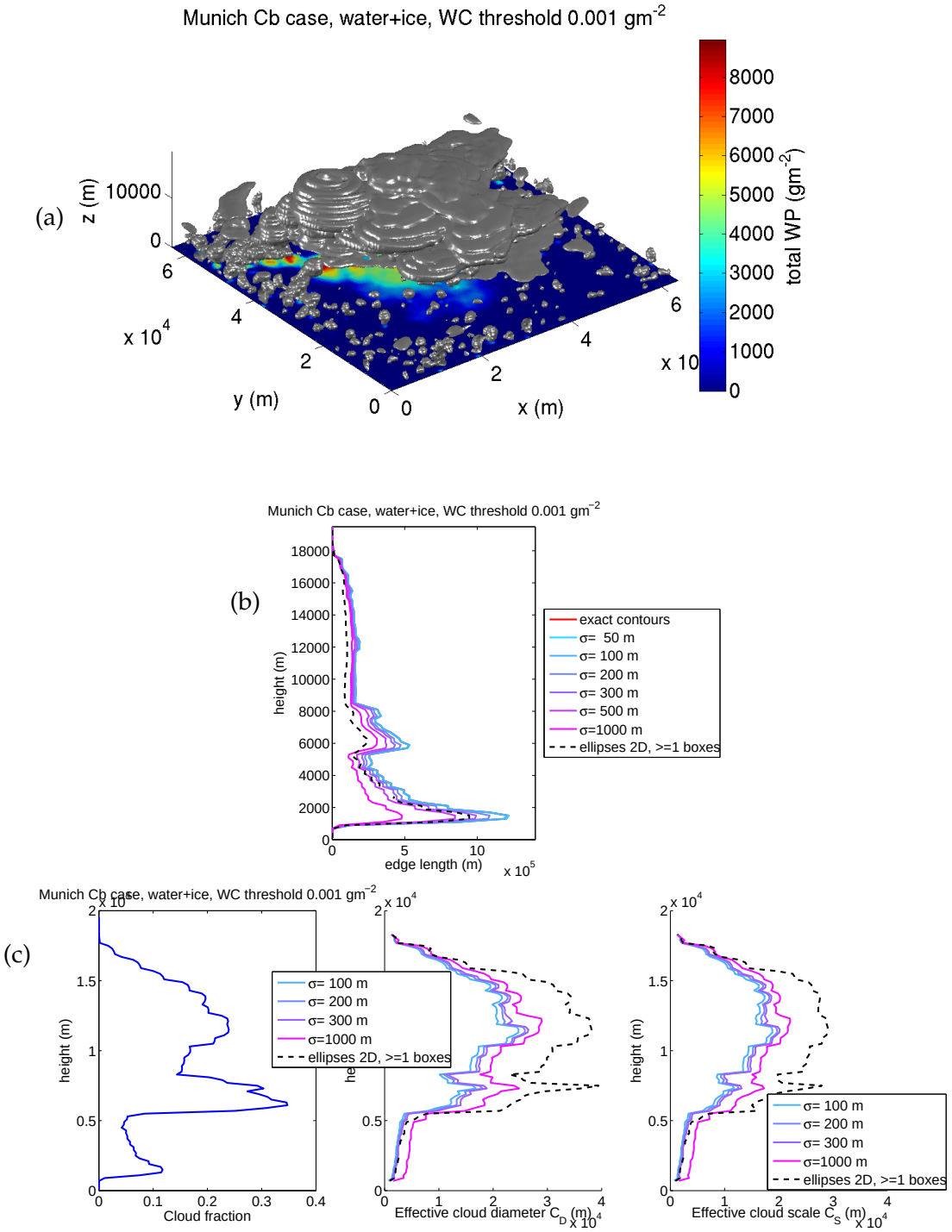

Figure 3.11: As in Figure 3.7, for the Goddard Space Flight Center / LMU cumulonimbus cloud case. Ellipse results (using labelling in each cloud layer) are shown for comparison, although the method is not necessarily appropriate for all cloud types in this field. Total cloud cover in this case is 0.57.

Close visual inspection of the cloud field in Figure 3.11a also shows that the clouds appear very like disks, suggesting that model numerics may have smoothed out some of the small-scale cloud structure. The cloud scale results do not vary much for the different smoothing-scale standard variations σ from 100 m to 300 m, likely because these scales are similar to the resolution Δx and hence smoothing does not strongly change the cloud structure. On the other hand, the cumulus layer is deeper than in the previous cases and transitions into the stratiform layer, and the cloud scale increases from $C_S \approx 820\,\mathrm{m} \pm 180\,\mathrm{m}$ at the base of the boundary layer to $C_S \approx 3\,\mathrm{km} \pm 300\,\mathrm{m}$ at the top, just below the stratiform layer. This increases our estimate of the uncertainty range for the best cloud scale for the boundary layer clouds in this case to $C_S \approx 2\,\mathrm{km} \pm 1\,\mathrm{km}$. In the layer between $z = 5\,\mathrm{km}$ and $z = 10\,\mathrm{km}$ that contains stratiform cloud and convective cores, the cloud scale increases to $C_S \approx 9\,\mathrm{km} \pm 2\,\mathrm{km}$, and to even higher values of $16\,\mathrm{km} \pm 4\,\mathrm{km}$ for the anvil layer above. Cloud scale values for the convective cores, stratiform layer and anvil layers are all of the same order of magnitude (although not the same). The larger uncertainty range compared to boundary-layer clouds is due to the inclusion of more different cloud types.

We can compare our values of cloud scale and effective cloud diameter to the area-equivalent radius of storms in 3D radar images of 5–10 km found by Stein et al. (2014), corresponding to a cloud diameter of 10 to 20 km. This value is not really the same as our effective cloud diameter C_D, because our method of deriving effective cloud diameter from the ratio of cloud area to cloud edge length would tend to result in a lower effective cloud diameter than area-equivalent diameter in cases where the cloud has a highly non-circular shape or high amount of small-scale structure and the cloud edges are hence longer than those of a cylinder of the same area even after smoothing. In effect, however, our effective cloud diameter C_D in the GSFC/LMU cumulonimbus case is between 15 km and 20 km in the deep convective region above $z = 5\,\mathrm{km}$ and therefore on the large side of the diameters measured by Stein et al. (2014). It is possible that limited radar sensitivity could decrease the measured size of the storm in the radar data, or mixture with stratiform clouds between $z = 5\,\mathrm{km}$ and $z = 8\,\mathrm{km}$ in the GSFC/LMU cumulonimbus case let the convective cores appear larger than they would be on their own. As already mentioned, the disk-like appearance of clouds in the GSFC/LMU simulation also raises the possibility that smaller features of cloud shape are suppressed by

the numerics of the simulation. In the cloud-resolving deep convection simulation of Tompkins (2001), analysed in Di Giuseppe and Tompkins (2003b), geometric diameters of the anvils were 15 km to 30 km, with lower diameters around 5 km for the convective cores below the anvils. Future analysis on more cloud cases will be needed to decrease the uncertainty in effective cloud scale for deep convective clouds.

3.5.3.4 Cirrus

As another example of high clouds, we consider a cirrus case, modelled with the "Cloudgen" stochastic fractal model of Hogan and Kew (2005) (also discussed in Zhong et al., 2008). This model statistically generates realistic 3D cloud shapes for given horizontal wind components, ice fall speed and mean, standard deviation and slope of the spatial power spectrum of the logarithm of the ice water content distribution. This is achieved by constructing an appropriate spectral power matrix with the desired properties in 3D discrete Fourier space. The effects of horizontal wind on ice fall streaks and turbulent mixing are taken into account by horizontal displacement and smoothing due to mixing. Inverse Fourier transformation then yields the cloud ice water field. The simulation's input quantities are derived from vertically pointing cloud radar time-height sections. We analyse a simulation for June 24th 1999 at Chilbolton Observatory, UK, the first case discussed in Hogan and Kew (2005). We have rerun the simulation at a higher resolution than in Hogan and Kew (2005) to enable detailed geometry analysis. Our cloud field has a domain size of 50 km$\times$50 km$\times$7 km and a resolution of 48.8 m in the horizontal and 109.4 m in the vertical. Again, we show results using the ellipse method for comparison (with layer-wise labelling in order to avoid merging different clouds due to wind-induced shear), although the clouds may not be distinct enough from each other for this method to perform well.

Figure 3.12 shows the cloud field and the cloud geometry results for the Cloudgen cirrus case: the cloud scale is $C_S \approx 4\,\text{km} \pm 1.5\,\text{km}$. This is smaller than the cloud scale of 9 km to 16 km seen for deep convective and stratiform clouds in the GSFC/LMU cumulonimbus case, indicating that cirrus streaks are smaller than deep convective cores, and have a more complex structure. The facts that horizontal resolution is finer in the Cloudgen cirrus case, the cloud layer is geometrically thinner and more homogeneous and does not contain very large clouds like the stratiform layer and the anvil in the

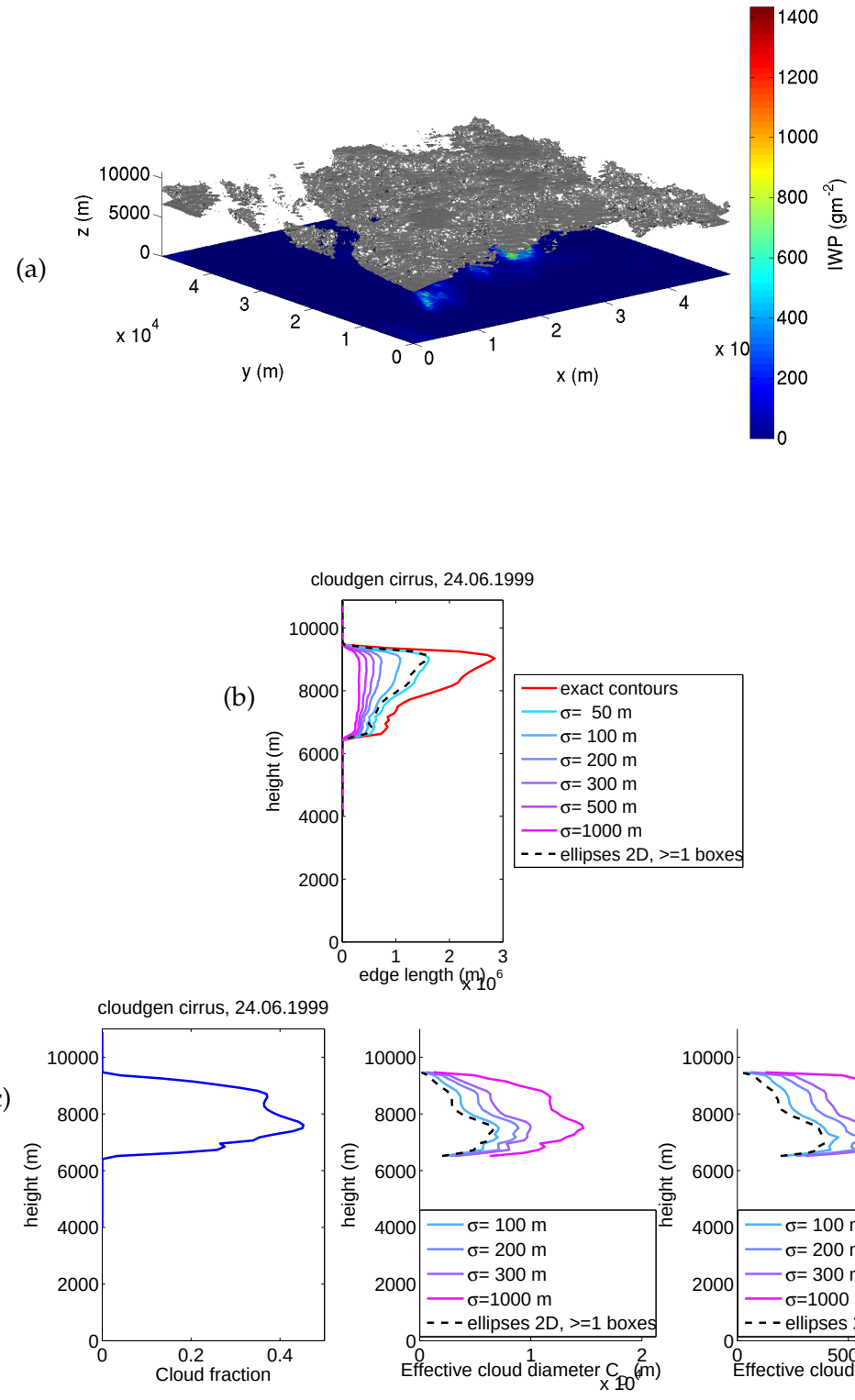

Figure 3.12: As in Figure 3.7, for the Cloudgen cirrus case. Ellipse results (using labelling in each cloud layer) are shown for comparison, although the method is not necessarily appropriate for cirrus cloud. Total cloud cover is 0.57.

GSFC/LMU case, and the GSFC/LMU simulation might not have enough small-scale structure could potentially exaggerate this difference. Cirrus clouds like those seen here are fairly common and can have a strong impact particularly on longwave radiation, so it is worth taking their cloud scale into account when we decide on a representative cloud scale for non-boundary-layer clouds.

3.6 Discussion of radiatively relevant cloud edge length and cloud scale

The decisive cloud geometry parameter for determining cloud side fluxes correctly in SPARTACUS is the effective cloud edge length relevant for radiation. For idealised clouds such as cubes, this is simply the geometric edge length. For realistic high-resolution cloud fields, we find that this length is lower than the measured cloud edge length for two reasons. First, the radiation field is smoother than the high-resolution cloud water field, so small-scale fluctuations of cloud water are irrelevant for radiation. We find that for cumulus clouds, a good approximation of the radiatively effective cloud edge length at a given height is the perimeter of an ellipse fitted to the cloud boundary such that area and aspect ratio are preserved. For other cloud types, this approximation is not practical, but we can use smoothing by convolution with a Gaussian smoothing kernel of standard deviation $\sigma = 100$ to 300 m for general cloud fields. We have compared the performance of both methods for cumulus cases, for which they yield very similar cloud edge results.

Second, clouds tend to be more clustered than would result from the random distribution assumed by SPARTACUS, enhancing the chance of radiation emitted from a cloud side being intercepted by a neighbouring cloud, and therefore reducing the effective length of cloud sides from which radiation escapes. To determine this reduction correctly, we would need to consider how strongly the clouds cluster. We have not analysed this effect extensively, but evaluation of geometry input parameters for SPARTACUS in Section 3.3 shows that multiplying the effective cloud edge length that accounts for radiative smoothing by 0.7 as an empirical clustering edge reduction produces radiative fluxes that best agree with fully 3D calculations. We are aware that this value is uncertain, as it is an empirical value derived from one case study of cumulus clouds that need

not be globally representative, but we will use it in our experiments as a best estimate and include the uncertainty in the effective cloud scale estimates. Further studies of cloud clustering for a number of cloud fields would be required to quantify the extent to which clouds cluster in reality and its impact on 3D radiative transfer more rigorously.

Cloud edge length in a given cloud field depends on the amount of clouds, and is hence hard to compare between different cloud scenes, even of the same type. We have derived a geometric parameter, the radiative effective cloud scale, that is independent of cloud fraction and only depends on cloud type. The known dependence of cloud edge length on cloud scale and cloud fraction (which is diagnosed in a global model) will allow us to compute radiative effective cloud edge for each gridbox in a global model if only the effective cloud scale for the cloud types in the gridbox is provided.

Table 3.2 summarises values for effective cloud scale we found in our own case studies and in the literature. Remarkably, we find very similar cloud scale values for boundary layer (BL) clouds between cumulus and stratocumulus, and between LES and cloud radar cases. All boundary layer cloud scales in our high-resolution case studies agree within their errors, at $C_S \approx 800\,\mathrm{m}$. Data at lower resolution like the cumulus in the GSFC/LMU case or the Jensen et al.'s MODIS data show larger cloud scales of $C_S = 2\,\mathrm{km}$ and $C_S = 10\,\mathrm{km}$, likely because the coarse resolution neglects fine cloud structure. Considering that cloud structure above the radiative smoothing scale η_{rad} of 200 m to 400 m is relevant for radiative transfer in boundary layer clouds, we consider the cloud scale derived from the high-resolution cases a better estimate.

To represent uncertainty in the method and the best smoothing kernel width, we will conduct experiments using BL cloud scales ranging from $C_S = 700\,\mathrm{m}$ to $C_S = 1.4\,\mathrm{km}$, with a best estimate of $C_S = 1\,\mathrm{km}$ that tends towards large cloud scale and therefore a conservative estimate of 3D effects. The reason we choose a cloud scale estimate on the large side is that we only approximately account for the reduction of effective cloud edge length and increase in effective cloud scale due to cloud clustering in our experiments and aim to avoid overestimating 3D effects.

For high clouds, the uncertainties in cloud scale are much larger, since this category includes more different cloud types and we have only considered two case studies, which is insufficient to fully determine the effects of each cloud type. High clouds also tend to be deeper and can be multi-layer and therefore have a larger range of cloud scales

at various levels. The cloud scale results vary between 4 km and 20 km. Effective diameter of the deep convective clouds in the GSFC/LMU cumulonimbus case was 15 km to 20 km, and thus similar to the geometric diameter of deep clouds in observations by Stein et al. (2014, 2015a) and the cloud-resolving model analysed by Di Giuseppe and Tompkins (2003b). We would expect radiative effective cloud diameter to be somewhat smaller than geometric diameter. Cloud diameter results from studies where we could not calculate the effective cloud scale are summarised in Table 3.3.

Based on the information we have available, we cannot really distinguish the effective cloud scale of various high cloud types outside of the level of uncertainty due to the small number of case studies. We therefore opt for using the same cloud scale value for all non-boundary layer clouds, with a best estimate of $C_S = 10\,\text{km}$ and representing the large uncertainty by conducting additional experiments using minimum and maximum high cloud scale values of $C_S = 5\,\text{km}$ and $C_S = 20\,\text{km}$. Future further analysis of different cloud types would be helpful in reducing uncertainty, ensuring our cloud scale results are globally representative and investigate if the cloud scales for different cloud types are systematically different enough that parametrising them separately would improve radiation results.

Another potential topic for future studies would be if the cloud scale depends on whether the clouds are precipitating. The cloud diameter values found by Stein et al. (2014) for precipitating deep convection were larger than the ones we found for non-precipitating shallow convection, but not systematically different from other high clouds (at the level of uncertainty of our investigations). Determining any systematic differences between precipitating and non-precipitating stratiform clouds would require additional data.

Case name	Data type	Cloud types	Resolution Δx	Boundary layer C_S	Non-BL C_S
I3RC Cu	LES	cumulus	66.7 m	800 m $\pm$ 200 m	-
Azores Cu	3D Cloud radar	cumulus	50 m	900 m $\pm$ 200 m	-
I3RC Stcu	LES	stratocumulus	55 m	700 m $\pm$ 200 m	-
GSFC/LMU Cb	LES/CRM	cumulus, stratus, cumulonimbus	250 m	2 km $\pm$ 1 km	13 km $\pm$ 6 km
Cloudgen Ci	Fractal model	cirrus	48.8 m	-	4 km $\pm$ 1.5 km
Jensen et al. (2008)	2D MODIS spectral radiometer	cumulus, stratocumulus	1 km	9.8 km $\pm$ 1.7 km	-
Morcrette (2012)	2D SEVIRI infrared imager	all	$\geq\approx$ 4 km	-	$\approx$ 13 km (large uncertainty)

Table 3.2: 3D cloud cases and literature analysed and respective effective cloud scale results.

Case name	Data type	Cloud types	Resolution Δx	BL cloud diameter	Non-BL cloud diameter
Stein et al. (2014)	3D 3-GHz radar	cumulonimbus	333 m	-	14 km $\pm$ 6 km
Di Giuseppe and Tompkins (2003b)	CRM	cumulonimbus	350 m	-	5 km to 30 km

Table 3.3: Literature studies without available cloud fraction to determine effective cloud scale and their respective geometric cloud diameter results.

Chapter 4

Global impact of 3D cloud-radiation interactions

4.1 Introduction

There have as yet been no comprehensive studies on the global impact of 3D cloud-radiation interactions, and the errors caused by neglecting them. The reasons such studies are challenging are that fully 3D calculations to use as benchmarks are not possible on a global scale, both due to their prohibitively high computational cost and the lack of global 3D cloud observations to use as input. One approach to tackle this challenge has been the use of "superparametrisations", cloud-resolving models embedded in a large-scale model, as suggested by Randall et al. (2003). Cole et al. (2005) used this approach to estimate a change of -5 to $+5$ $\mathrm{W\,m^{-2}}$ (depending on latitude) in zonally averaged shortwave CRE and an increase of less than $1\,\mathrm{W\,m^{-2}}$ in zonal averages of longwave CRE. These numbers are lowered by taking the zonal means, but are also likely underestimated due to the use of 2D approximations, which neglect one dimension of horizontal radiative transfer, and the coarse spatial resolution of 4 km, which neglect some of the cloud structure. Barker et al. (2016) suggested truly 3D global radiation calculations using a fully 3D Monte Carlo model with reduced photon number on stochastically generated 3D cloud fields, based on globally available cloud information. However, in spite of the reduced photon numbers, this approach remains highly computationally expensive, and has therefore not yet been used for a global estimate of 3D effects.

In this chapter, we will provide such a global estimate of 3D effects, applying the SPARTACUS radiation model to one year of climate reanalysis data. Due to its simplifications, SPARTACUS does not need exact 3D cloud geometry information as input, but only the effective cloud edge length in each layer. For more precise results, this should be modified to represent cloud clustering. We have found in Section 3.4 in Chapter 3 that

cloud edge length is well described as a simple function of cloud fraction, depending on one parameter, the typical cloud scale C_S, which in turn only depends on cloud type. Here, we will first describe the model setup, atmospheric variable and cloud geometry input we use in our global experiments (in Section 4.2). Section 4.3 will then present the results on the global impact of 3D cloud-radiation effects on radiative fluxes and heating rates, the annual cycle of the effects and their sensitivity on effective cloud scale. Our conclusions are presented in Section 4.4.

4.2 Experiment design and atmospheric input

As detailed in Hogan et al. (2016) and summarised in Section 2.4, Robin Hogan has implemented SPARTACUS in a modified version of the ECMWF's radiation scheme. We have configured this scheme for offline radiation calculations using as input atmosphere and surface data from the ECMWF Interim reanalysis (ERA-Interim, Dee et al., 2011). The ERA-Interim reanalysis is calculated with the ECMWF Integrated Forecast System (IFS), using four-dimensional data assimilation (4D-Var) of satellite and conventional (e.g. surface, aircraft and radiosonde) observations. Clouds are represented by a bulk method in each gridbox (ECMWF, 2007), with contributions for stratiform cloud and for convective cloud which is represented as a single pair of entraining and detaining plumes (Tiedtke, 1993). The cloud scheme provides cloud fraction and cloud ice and water content in each model layer. In the version of the IFS used for ERA-Interim, no satellite observations of clouds are assimilated, so the clouds in the model are simulated based on atmospheric conditions. The version of radiation code used for the radiation calculations in ERA-Interim was described by Morcrette et al. (2007). Although there are some differences in cloud structure (Jiang et al., 2011), ERA-Interim evaluation has shown that the data set reproduces observations of atmospheric variables, including cloud occurrence and cloud radiative effect and the Earth's radiation budget, and their variation over time remarkably closely both globally (Dee et al., 2011; Allan, 2011) and on regional scales (Szczypta et al., 2011; Zygmuntowska et al., 2012; Zib et al., 2012), given the uncertainties in comparisons of different data sets.

We conduct radiation calculations on global ERA-Interim scenes at 0 UTC, 6 UTC, 12 UTC and 18 UTC each day for the whole of 2001. Data resolution is $1.5^\circ \times 1.5^\circ$ with 60

vertical layers. In order to decrease computational cost, we sub-sample the gridboxes by a factor of 2 in both longitude and latitude. The ERA-Interim data provides temperature, relative humidity and pressure as well as cloud fraction, cloud water and cloud ice at each model level. We do not include aerosol in the calculations. We include ozone with variable mass mixing ratio taken from ERA-Interim, but treat the volume mixing ratios of other atmospheric gases as constant, at 0.2095 for O_2, 3.790×10^{-4} for CO_2, 1.774×10^{-6} for methane, 3.190×10^{-7} for N_2O, 2.510×10^{-10} for CFC_{11} and 5.380×10^{-10} for CFC_{12}. The shortwave albedo of the surface is provided by ERA-Interim, while surface longwave emissivity is set to a constant value of 0.98. Incoming total solar irradiance is assumed to be $1366\,\mathrm{W\,m^{-2}}$. The solar zenith angle in each gridbox is computed from the day of the year and time of day, and we sample the 6 hour timestep by adding a time increment randomly chosen in the interval from $-3\,\mathrm{h}$ to $+3\,\mathrm{h}$. This time sampling introduces no bias but some noise in the instantaneous results; however, this noise is reduced when we average the results for each month.

Cloud optical properties are determined from a look-up table pre-computed with the UK Met Office's "SOCRATES" (Suite of Community Radiative Transfer codes based on Edwards and Slingo) radiation package (J. Manners, personal communication, 2014) using a Padé-approximant fitted to Mie calculations for each of the 30 spectral bands of RRTM-G and including longwave scattering for cloud liquid water and the weighted ice crystal habit mixture model of Baran et al. (2014) for ice. Effective radius of cloud particles is assumed to be $10\,\mu\mathrm{m}$ for liquid droplets and to depend on atmospheric conditions as described by Baran et al. (2014) for ice particles. Except in the McICA experiments, cloud horizontal inhomogeneity is treated with the Tripleclouds method of Shonk and Hogan (2008), dividing the cloud into optically thick and thin regions as detailed in Hogan et al. (2016) and using a constant fractional standard deviation of cloud water of 0.75, as in Shonk et al. (2010). Vertical overlap between layers is treated using overlap matrices as described by Shonk and Hogan (2008) and Hogan et al. (2016), with a cloud vertical decorrelation length of 2 km, as found by Barker (2008).

For each scene we perform a set of radiation experiments using different radiation solvers and cloud geometry inputs, listed in Table 4.1. To determine the change due to each 3D effect, we conduct two separate 1D experiments as control: the first is a 1D run using the SPARTACUS 1D solver, which excludes any radiative transfer through

cloud sides (assuming the effective cloud scale C_S to be infinite), but still allows some horizontal transport via the effect of horizontal in-region transport in the shortwave, as discussed in Section 1.3. As this effect is mainly caused by multiple scattering in multiple cloud layers, it is much less pronounced in the longwave where scattering is less important. This experiment is representative of a typical region-based two-stream scheme. The second 1D experiment uses a McICA solver (Pincus et al., 2003), as is used in many current global models, like the current version of the IFS. This setup excludes any horizontal transfer between different regions. Except for some numerical noise introduced by the sampling of spectral bands in the McICA setup (and removed when averaging over multiple calculations), it is unbiased with respect to the ICA approximation. As discussed in Section 1.3, in schemes using the ICA approximation, including McICA, clouds are systematically more reflective than in region-based two-stream schemes, representing the spread in existing 1D schemes. We also perform 3D experiments using our new SPARTACUS 3D solver with different cloud scale inputs representing the range of our case study results, in order to sample the uncertainty due to the cloud geometry parametrisation (summarised in Table 4.1). Results are calculated for the shortwave and longwave spectral regions (abbreviated sw and lw) separately, and for the total spectral region. Each radiation calculation also includes an equivalent calculation assuming clear sky, in order to determine the cloud radiative forcing (CRF, the difference between fluxes with and without cloud). Based on our experiments in Chapter 3, we use different effective cloud scale inputs for low boundary-layer clouds and for middle and high clouds. Clouds are classified as low clouds if they are located between 1 and 0.8 times the surface pressure, in line with the ECMWF diagnostic system (which classifies cloud at pressures less than 0.45 times the surface pressure as high and between 0.8 and 0.45 times the surface pressure as middle clouds [1]).

4.3 Results

4.3.1 Instantaneous 3D cloud side effects

We first consider instantaneous radiative fluxes in a global scene at a given time. The example scene we show here is on April 1st 2001 at 12 UTC. Figure 4.1 shows the total

[1] http://www.ecmwf.int/en/faq/how-are-low-medium-and-high-cloud-cover-defined

Run name	Boundary layer C_S	Non-boundary layer C_S
1D SPARTACUS (allows 3D horizontal in-region transport in shortwave)	∞	∞
1D McICA (no 3D effect)	∞	∞
3D control	1 km	10 km
3D maximum C_S	1.4 km	20 km
3D minimum C_S	700 m	5 km
3D Jensen C_S	10 km	10 km
3D BL only	1 km	∞

Table 4.1: Global experiments and cloud scale input.

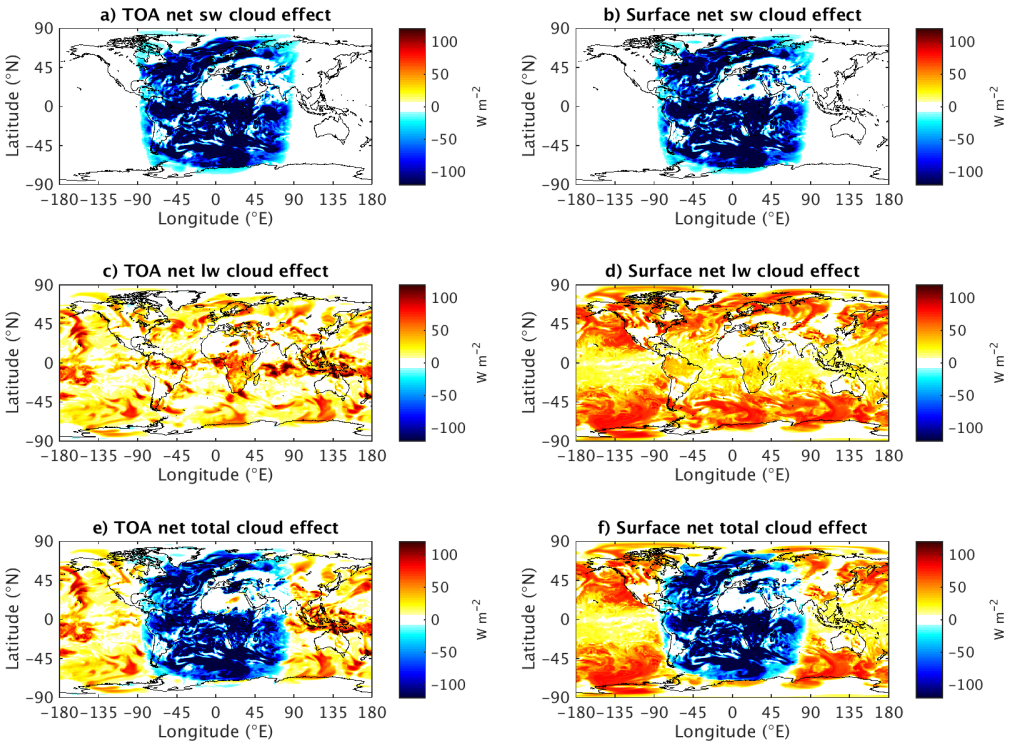

Figure 4.1: Cloud radiative forcing (CRF) on total net (downwelling - upwelling) radiation at top-of-atmosphere (TOA, left-hand column) and at the surface (right-hand column), for shortwave, longwave and total spectral regions in the 3D control run on April 1st 2001 at 12 UTC.

cloud radiative forcing in the 3D control run at this time. We can see that on the day-time side of the globe, strongly negative shortwave cloud effects dominate (except for a small area over the Sahara for TOA CRF), while on the night-time side, interaction with

longwave radiation causes a positive cloud effect. The strongest effects are seen over oceans and tropical rain forest in the shortwave, at the Inner-Tropical Convergence Zone (ITCZ) and the storm tracks for the longwave TOA effect and the storm track regions for the longwave surface effect. The effects also depend on cloud occurrence.

Figure 4.2 shows the change in cloud radiative forcing caused by 3D interaction with cloud sides (calculated as the difference between the 3D control and 1D SPARTACUS runs, which both include in-cloud horizontal transfer and only differ by the 3D cloud side effect). We can distinctly see the action of the two different shortwave cloud side effects: for overhead sun (SZA $< 30°$), the dominant effect is cloud side leaking which reduces the negative shortwave cloud effect and hence warms, while for low sun ($30° <$ SZA $< 90°$), the dominant effect is cloud side interception which increases the negative shortwave cloud effect and thereby cools. Longwave cloud side effects are always positive, increasing the positive longwave cloud effect, but on the day-time side of the globe, they are overcome by the stronger shortwave effects.

4.3.2 Annual mean cloud radiative forcing

For judging the impact of 3D effects on global weather and climate, long-time averages are more relevant than instantaneous 3D effects in one scene. We here consider annual mean results for 2001. Figure 4.3 shows global maps of annual mean CRF for the various spectral regions at top-of-atmosphere (TOA) and surface, in the control run including 3D effects. Shortwave CRFs are negative, since clouds reflect incoming solar radiation back up. The strongest shortwave CRFs are seen in regions of frontal clouds or marine stratocumulus, particularly in the North Pacific, but also over higher-latitude oceans (like the Southern Ocean), regions of tropical rain forest and the Maritime Continent. Generally, apart from tropical rain forest regions, shortwave CRFs are stronger over oceans than over land. This is explained partly by moister air and more clouds over the ocean, but also because both ocean and tropical rain forest have very low surface albedo, increasing the contrast with the albedo of clouds and hence shortwave cloud radiative effects. Conversely, the regions with lowest shortwave cloud radiative forcing are those with highly reflective surfaces and few clouds (Greenland and Antarctica) or negligible cloud occurrence (Sahara, Arabic Peninsula, Pakistan, Antarctic interior).

Longwave CRFs are always positive, as clouds decrease the amount of outgoing

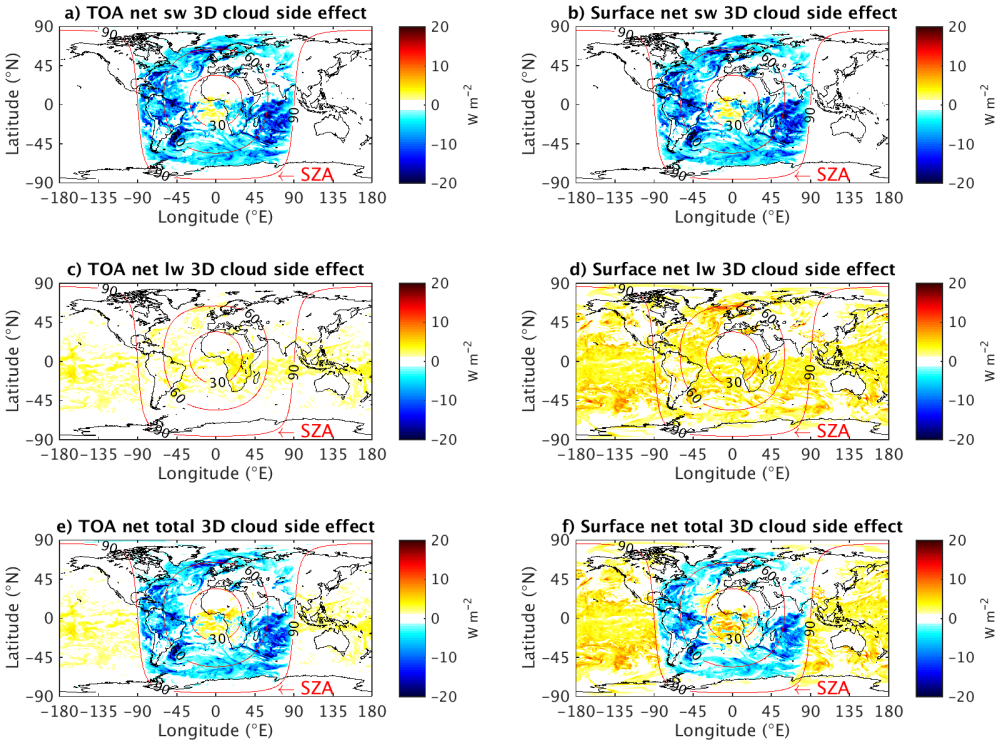

Figure 4.2: 3D cloud side effects (calculated as difference between the 3D control run and the 1D SPARTACUS run) on total net (downwelling - upwelling) radiation at top-of-atmosphere (TOA, left-hand column) and at the surface (right-hand column), for shortwave, longwave and total spectral regions in the 3D control run on April 1st 2001 at 12 UTC.

longwave radiation and radiate down towards the surface. At TOA, longwave CRFs are strongest over the Maritime Continent, with weaker peaks over tropical rain forest and the maritime storm tracks, correlating strongly with regions of deep convection. Other than in the shortwave, surface longwave effects are markedly different from those at TOA. Surface longwave CRF is generally somewhat higher than at TOA, with the highest values seen in marine stratocumulus regions and over mid- and high-latitude oceans (poleward of $\pm 45°$N). High values over land occur in Norway and Siberia, the Himalayas, the northern Rocky Mountains and the highest parts of the Andes; high values of longwave cloud radiative forcing are generally seen in regions where many low clouds occur, as these emit longwave radiation down towards the surface. The only areas of the globe without significant positive longwave CRF at the surface are those with very low cloud cover.

At TOA, shortwave cloud effects are generally stronger than longwave effects, with

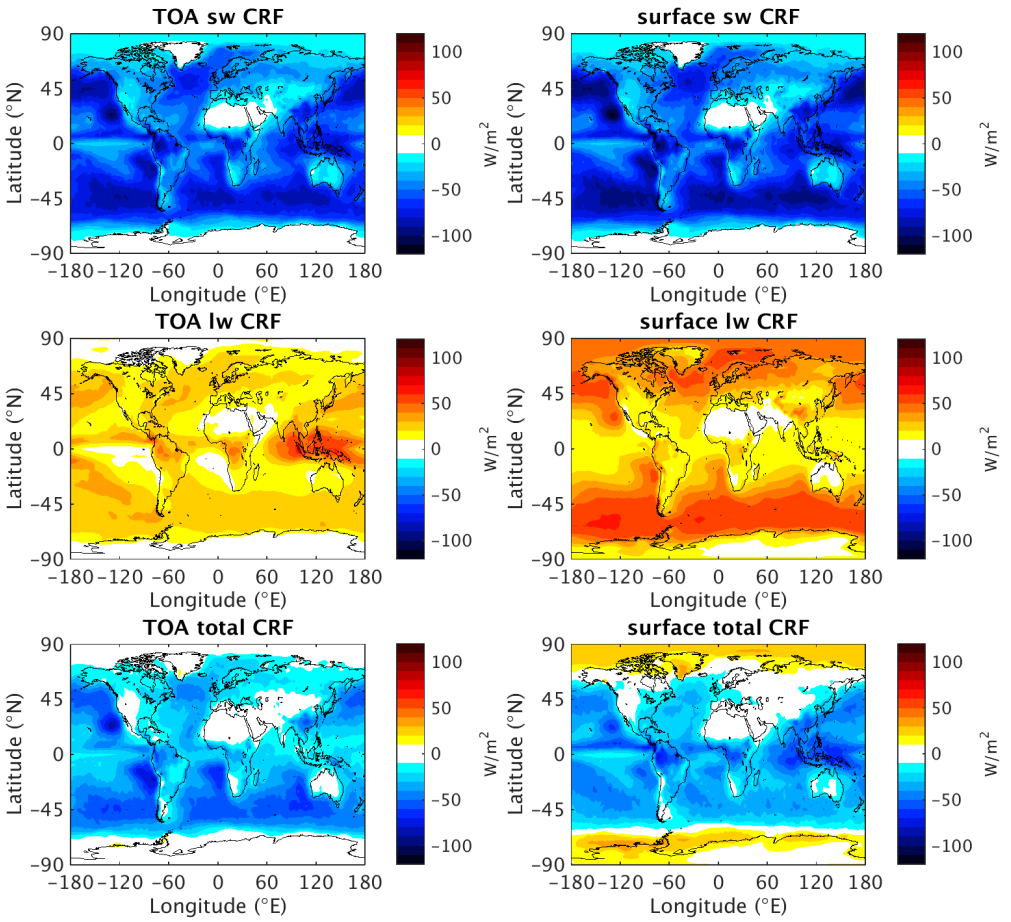

Figure 4.3: Global annual mean cloud radiative forcing (CRF) on total net (downwelling - upwelling) radiation at top-of-atmosphere (TOA, left-hand column) and at the surface (right-hand column), for shortwave, longwave and total spectral regions in the 3D control run.

a global annual average CRF of $-49.68\,\mathrm{W\,m^{-2}}$ in the shortwave versus $+21.92\,\mathrm{W\,m^{-2}}$ in the longwave, leading to negative total TOA CRF everywhere except for small cloudy regions over snowy surfaces in southern Greenland and the Antarctic Peninsula and a global average total CRF of $-27.76\,\mathrm{W\,m^{-2}}$. In the tropics, particularly the Maritime Continent, and over high-latitude oceans, longwave CRF partly compensates shortwave CRF, leaving the marine stratocumulus regions, northern Pacific and Southern Ocean west of Australia as the regions with strongest overall negative CRF.

At the surface, on the other hand, the sign of total CRF is zonally dependent: in the tropics, subtropics and most of the temperate zone (especially oceans), shortwave effects dominate, leading to negative total CRF which is strongest at the ITCZ, the Maritime

Continent, tropical rain forest and stratocumulus regions in the Pacific. Over much of the Northern Hemisphere land area, shortwave and longwave effects nearly cancel each other. At high latitudes poleward of around $\pm 65^\circ$ however, longwave effects dominate, leading to positive total surface CRF (except for Central Antarctica, which has very little cloud). The global annual average surface CRF is $-53.44\,\mathrm{W\,m^{-2}}$ in the shortwave, $+28.99\,\mathrm{W\,m^{-2}}$ in the longwave and $-24.45\,\mathrm{W\,m^{-2}}$ in total (global average values are summarised in Table 4.2).

Run name	TOA sw	TOA lw	TOA total	surface sw	surface lw	surface total
control 3D	−49.68	21.92	−27.76	−53.44	28.99	−24.45
1D McICA	−52.69	20.98	−31.71	−55.73	26.92	−28.81
CERES data	−47.27	26.19	−21.08	-	-	-

Table 4.2: Global annual mean cloud radiative forcing CRF (in $\mathrm{W\,m^{-2}}$) in the 3D control experiment, the McICA experiment and in CERES data.

As a comparison, Figure 4.4 shows the TOA CRF in shortwave, longwave and in total as derived from average CERES Energy Balanced And Filled (EBAF) data [2] for the years 2000 to 2011. Global mean values (adjusted for the variable area of gridboxes over the globe) for both the 3D control and McICA experiments and the CERES data are compared in Table 4.2. We can see that both the magnitudes of the CRF results in each spectral region and their spatial distribution are similar in the 3D control experiment results and the CERES observations. CERES shortwave CRF is slightly less negative in the northeastern Pacific, south Pacific, Southern Ocean south and southwest of Australia, and tropical rain forest in South America and Africa, while CERES longwave CRF is higher in the regions where it is high anyway, like the storm tracks and the ITCZ. Together, these differences lead to CERES total CRF that is somewhat less negative, or more positive, than in the 3D experiment. In the global average, the total difference is $6.68\,\mathrm{W\,m^{-2}}$ or 24% of the CRF in the 3D control experiment, mostly due to longwave differences. These differences partly occur because CERES derives the clear-sky values used to determine CRF from clear sky at some distance from clouds, while the model uses a calculation for identical conditions to reality except without cloud (Allan and Ringer, 2003). This means that on average, there is less water vapour in the clear sky in the CERES CRF derivation, which would tend to lead to an underestimation of clear-

[2] http://ceres.larc.nasa.gov/products.php?product=EBAF-TOA

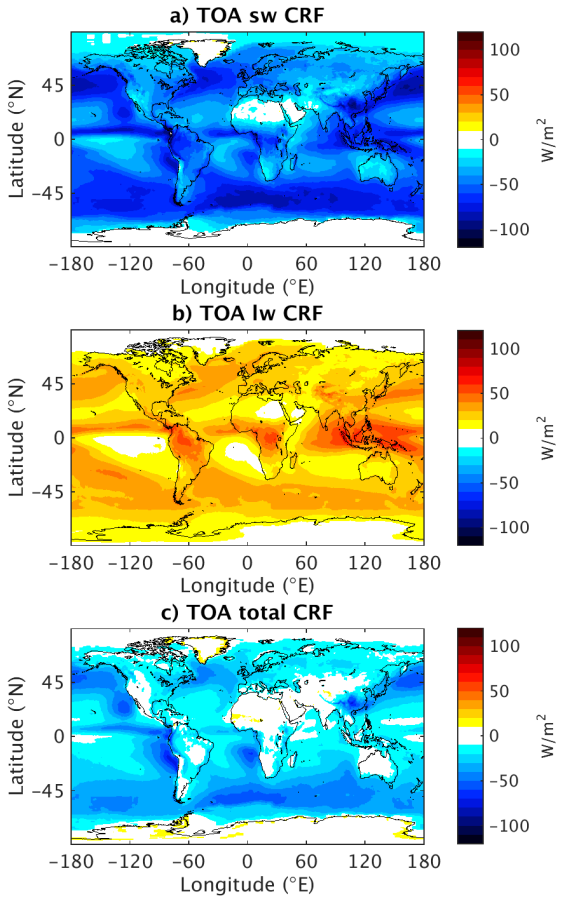

Figure 4.4: Global annual mean cloud radiative forcing (CRF) on total net (downwelling - upwelling) radiation at top-of-atmosphere in CERES observations, for shortwave, longwave and total spectral regions.

sky longwave absorption and emission and therefore an overestimation of CRF in the longwave.

Figure 4.5 shows the annual mean change in CRF due to 3D cloud side effects, $\Delta_{\text{3D cloud side}}$CRF, calculated as the difference in CRF in the 3D control run and the 1D SPARTACUS solver run, which does not include cloud side transport but allows horizontal in-region transport in the shortwave, where the effect is relevant (the effect is due to in-region diffusion combined with backscattering; in the longwave clouds scatter less and absorb more, strongly reducing multiple scattering and hence the horizontal transport effect). As discussed in Section 2.4, complete horizontal diffusion as in traditional region-based two-stream schemes or SPARTACUS could potentially overestimate this effect. However, in our experiments agreement with fully 3D codes was very good

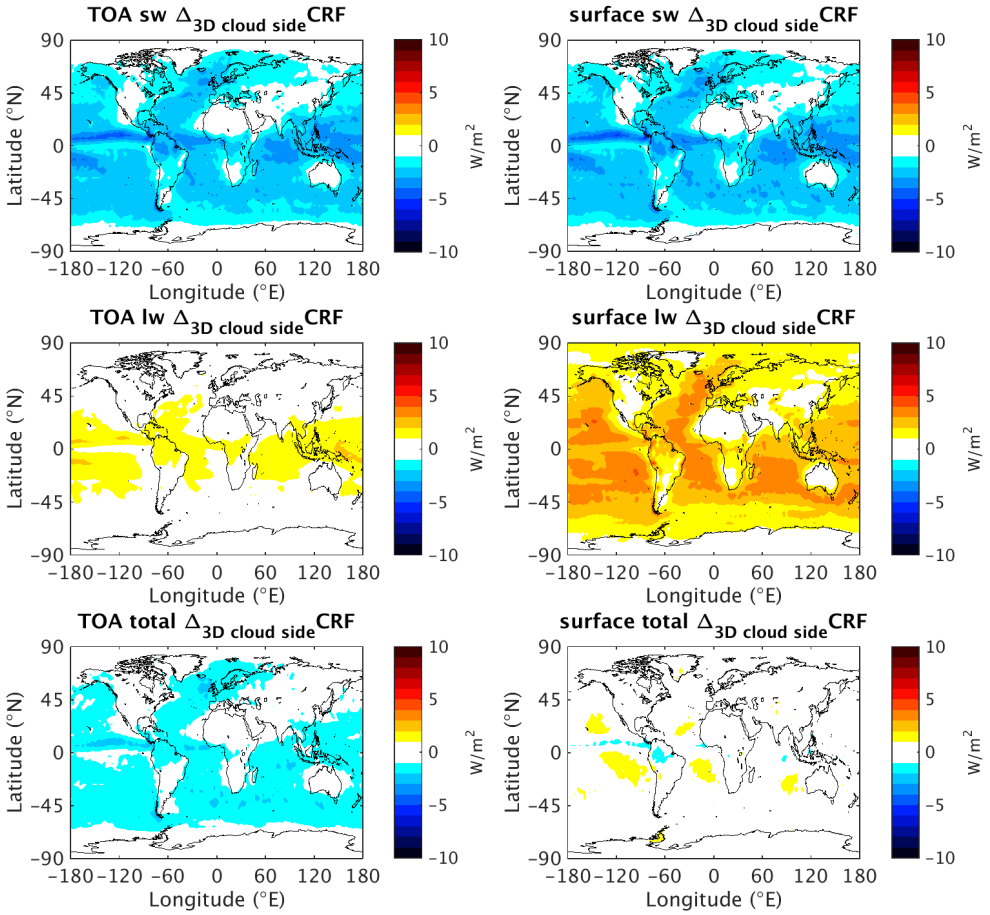

Figure 4.5: Global annual mean 3D cloud side effect on cloud radiative forcing (CRF), $\Delta_{\text{3D cloud side}}$CRF. Effects on total net (downwelling - upwelling) radiation at top-of-atmosphere (TOA, left-hand column) and at the surface (right-hand column), for shortwave, longwave and total spectral regions in the 3D control run, relative to the 1D SPARTACUS control run including horizontal in-region transport in the shortwave.

suggesting that the effect is not strongly overestimated.

Cloud side effects are seen in most regions of the globe that have sufficient cloud cover, peaking at the ITCZ in the shortwave and over mid-latitude storm track regions in the longwave (particularly at the surface). The effects are weakest over land areas that have few clouds, but shortwave effects also decrease over the poles, where no sunlight is incident for half of the year and the surface is very reflective. Shortwave global annual mean cloud side effects are negative, showing that in the annual mean, the negative shortwave cloud side illumination effect encountered when the sun is low dominates over the positive shortwave cloud side leakage effect seen for overhead sun (which is

only relevant to a small section of the globe at any given time). Longwave 3D cloud side effects at TOA are weaker than at the surface, leading to a total global mean TOA cloud side effect of $-1.04\,\mathrm{W\,m^{-2}}$. The shortwave effect somewhat deteriorates agreement of CRF with CERES data, while the longwave effect improves agreement. Since the shortwave effects are stronger, overall agreement with CERES is slightly degraded by 3D cloud side effects. At the surface, shortwave and longwave cloud side effects nearly compensate each other. The strength of the effects depends on the cloud geometry. We will further investigate this dependence in Section 4.3.3. Full results for several cloud geometry inputs are summarised in Table 4.4.

The shortwave horizontal in-region transport effect we see in the 1D SPARTACUS

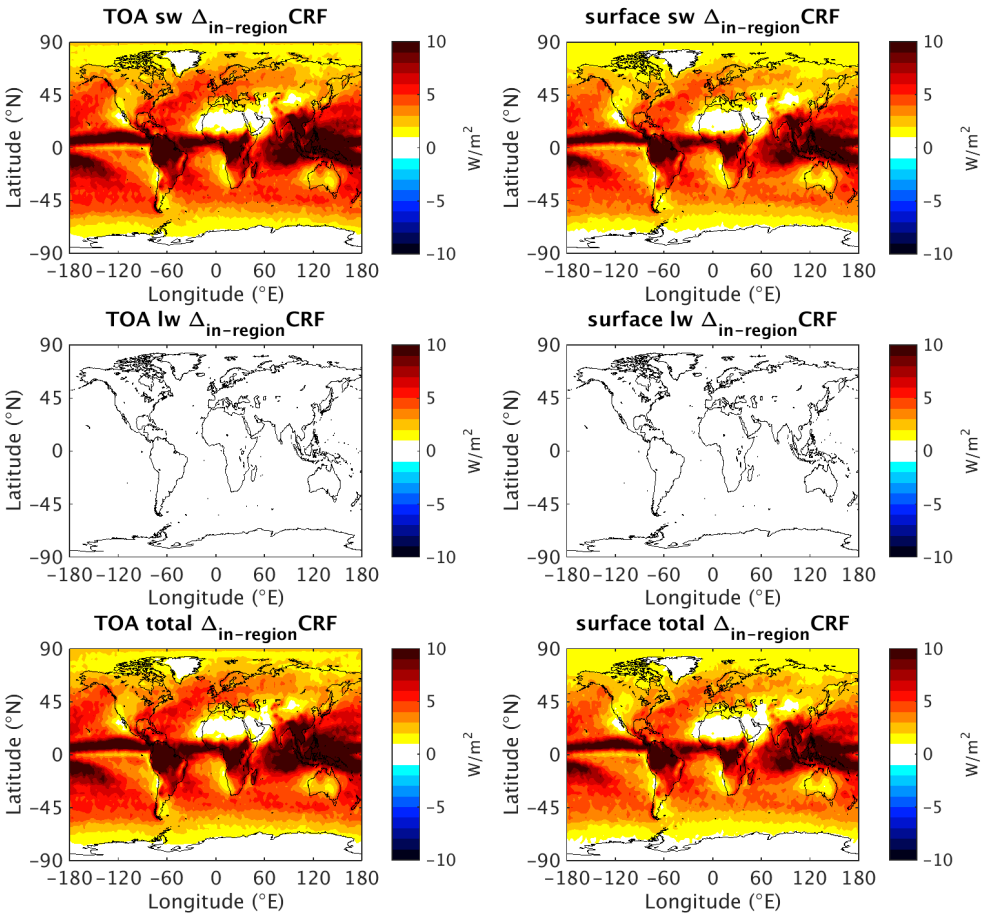

Figure 4.6: Global annual mean effect on cloud radiative forcing (CRF) due to in-region horizontal transfer, $\Delta_{\text{in-region}}$CRF. Effects on net (downwelling - upwelling) radiation at top-of-atmosphere (TOA, left-hand column) and at the surface (right-hand column), for shortwave, longwave and total spectral regions in the 1D SPARTACUS run, relative to the McICA run.

Run name	TOA sw	TOA lw	TOA total	SFC sw	SFC lw	SFC total
1D SPARTACUS	4.88	0.11	4.99	4.23	−0.03	4.20

Table 4.3: Global annual mean change on cloud radiative forcing due to horizontal in-region transport, $\Delta_{\text{in-region}}$CRF (in $\mathrm{W\,m^{-2}}$) in the 1D SPARTACUS run compared to the McICA experiment, at TOA and at the surface (SFC).

run compared to the McICA run (shown in Figure 4.6, global mean results in Table 4.3) is stronger than the shortwave 3D cloud side effect, and of opposite sign: the in-region transport effect decreases cloud shortwave reflectivity and thereby warms the Earth, while there is no change to longwave CRF (as expected). The effect occurs all over the globe except in regions with very little cloud occurrence and high surface reflectivity, but is strongest over tropical oceans and tropical rain forest, and stronger at TOA than at the surface.

This leads to a total 3D cloud effect on CRF compared to the McICA run, Δ_{3D}CRF (encompassing both cloud side effects and in-region transport and shown in Figure 4.7), that looks very different from the cloud side effect alone: the shortwave total 3D effect relative to McICA has the opposite sign to the 3D cloud side effect seen compared to the 1D SPARTACUS experiment. This change greatly increases the magnitude of the total 3D effect and at TOA also changes its sign, since total 3D effects in the shortwave and the longwave have the same sign and hence do not compensate but add to each other.

Global annual mean total 3D effects are around 1.5 to $3.0\,\mathrm{W\,m^{-2}}$ in the shortwave, 0.7 to $2.9\,\mathrm{W\,m^{-2}}$ in the longwave and 3.5 to $4.4\,\mathrm{W\,m^{-2}}$ in total (see Table 4.5 for exact results for each run). This is larger than the radiative forcing effects of anthropogenic greenhouse gases added since 1750 (estimated as 2.54 to 3.12 $\mathrm{W\,m^{-2}}$, Myhre et al., 2013) and similar to the effects of horizontal and vertical cloud inhomogeneity (Shonk and Hogan, 2010, found total effects of around $4\,\mathrm{W\,m^{-2}}$ due to horizontal cloud structure and around $2\,\mathrm{W\,m^{-2}}$ for vertical cloud structure at both TOA and the surface). Local 3D effects in individual GCM gridboxes are stronger, up to $10\,\mathrm{Wm^{-2}}$ even in the annual average and at the large $1.5^\circ \times 1.5^\circ$ gridboxes we are considering. The total global 3D effects amount to −14% of total CRF at TOA and −18% at the surface in the 3D control run. These results for the first time provide a systematic estimate of the impact of 3D cloud effects on both longwave and shortwave radiation on a global scale.

Including the positive in-region horizontal transfer effect markedly improves agree-

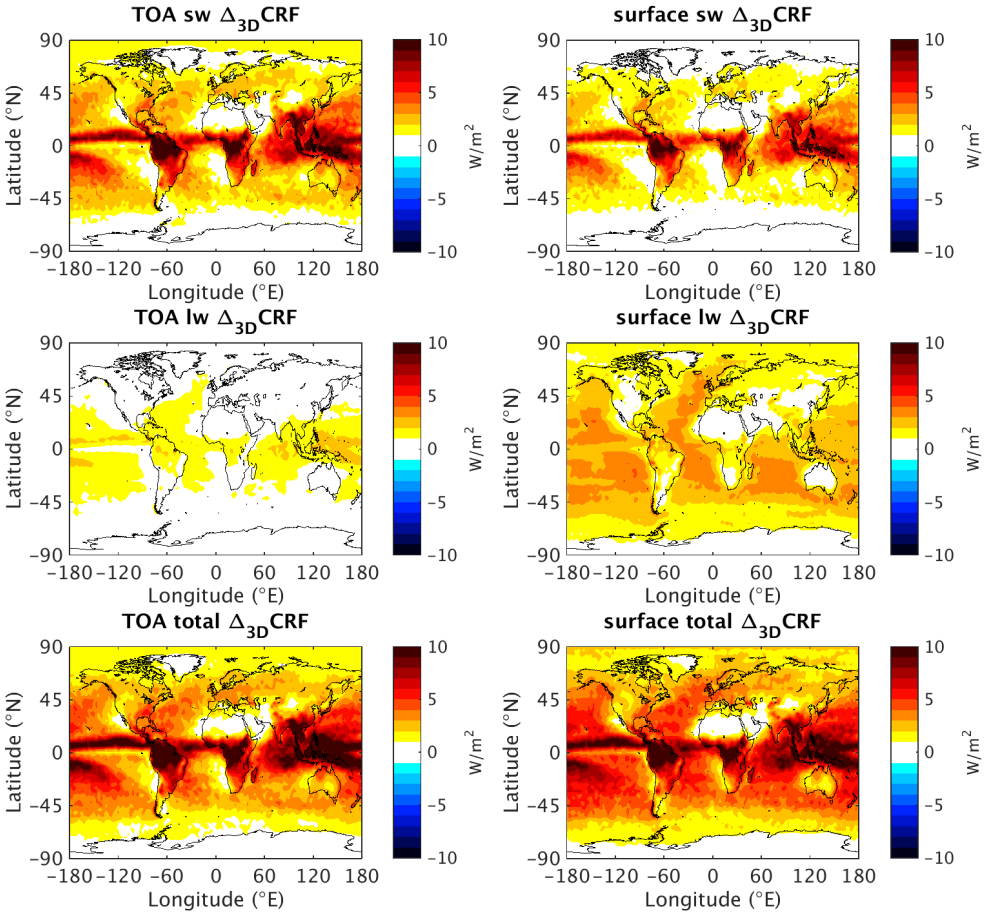

Figure 4.7: Global annual mean total 3D effect on cloud radiative forcing (CRF), Δ_{3D}CRF. Effects on net (downwelling - upwelling) radiation at top-of-atmosphere (TOA, left-hand column) and at the surface (right-hand column), for shortwave, longwave and total spectral regions in the 3D control run, relative to the McICA run.

ment with CERES data, reducing the differences between model CRF at TOA and observations by about 56% in the shortwave, 18% in the longwave and 37% in total in the 3D control run compared to the McICA run. This agrees with the increase in global flux bias relative to CERES-EBAF Paquin-Ricard et al. (2016) reported for the McICA method compared to a region-based 1D radiation scheme. The bias increase was mostly due to shortwave cloud reflectivity overestimation in McICA.

Bearing in mind some remaining uncertainty about whether the in-region horizontal transport in SPARTACUS is slightly overestimated, the strength of the in-region horizontal transfer effect and hence the large spread between different 1D models is still remarkable, reaching -18% of total 3D CRF at TOA and -17% at the surface. The McICA

control run best represents the behaviour of current climate models, many of which use McICA methods, while the 1D SPARTACUS run represents traditional region-based two-stream models. We have compared shortwave reflected flux from various 1D solvers to fully 3D MYSTIC calculations for one cumulus cloud scene in Figure 2.5, which suggested that for high sun, 1D SPARTACUS is very close to the correct 3D shortwave fluxes, while for lower sun all 1D codes underestimate reflectivity, the 1D SPARTACUS solver (in which reflectivity is also reduced by in-region horizontal transfer) somewhat more so than ICA codes. Averaged over the diurnal cycle, the 3D shortwave results lie between the results of region-based schemes that include horizontal in-region transport and ICA or McICA schemes, while in the longwave, 3D effects increase CRE relative to all classes of 1D models. This suggests that on the global scale also, correct 3D CRF should lie in between the CRF computed by 1D region-based and ICA solvers, as the CRF in our 3D experiment does.

4.3.3 Zonal mean 3D effect and sensitivity to cloud geometry input and 1D model assumptions

Tables 4.4 and 4.5 show the range of results seen in the 3D experiments using our best estimate of cloud scale (the 3D control experiment) and the range of cloud scale inputs we consider probable (the 3D maximum C_S and minimum C_S experiments), relative to the 1D McICA run and the 1D in-region horizontal transport run, respectively.

It is worth noting that the sensitivity of total 3D effect, compared to McICA, on cloud scale has opposite signs for longwave and shortwave: while the 3D longwave effect increases with decreasing cloud scale (as we would expect, since this increases the amount of cloud edge in each gridbox), the shortwave 3D effect decreases. This is because the

Run name	TOA sw	TOA lw	TOA total	SFC sw	SFC lw	SFC total
control 3D	−1.87	0.83	−1.04	−1.94	2.10	0.16
maximum C_S	−1.33	0.57	−0.76	−1.40	1.53	0.13
minimum C_S	−2.66	1.17	−1.48	−2.73	2.92	0.19

Table 4.4: Global annual mean 3D cloud side change on cloud radiative forcing $\Delta_{\text{3D cloud side}}$CRF (in W m^{-2}) for various experiments (all relative to the 1D SPARTACUS run including shortwave horizontal in-region transport), at TOA and at the surface (SFC).

Run name	TOA sw	TOA lw	TOA total	SFC sw	SFC lw	SFC total
control 3D	3.01	0.94	3.95	2.29	2.07	4.36
maximum C_S	3.55	0.68	4.22	2.83	1.50	4.33
minimum C_S	2.22	1.28	3.51	1.50	2.89	4.39

Table 4.5: Global annual mean total 3D change on cloud radiative forcing Δ_{3D}CRF (in $\mathrm{W\,m^{-2}}$) for the various experiments (all relative to the McICA 1D control run), at TOA and at the surface (SFC).

difference between 3D experiments and McICA results is due to two effects: the 3D cloud side effect and the horizontal in-region transport effect, and the two effects partially compensate each other. The results on 3D effects shown above are not very sensitive to cloud geometry input, changing by a maximum of 42% of the 3D control value for the TOA 3D cloud side effect and by much less for most other quantities over our range of cloud scale inputs.

In order to explore the extreme range of possible cloud geometry input, and estimate the role of spatial resolution of cloud observations and the relative impact of high versus low clouds, we have conducted additional experiments using the value of $C_S = 10\,\mathrm{km}$ in the boundary layer, as derived from MODIS data from Jensen et al. (2008), and with 3D effects only for boundary layer clouds. Figures 4.8 and 4.9 show longitudinal annual averages of CRF in the 3D control and McICA experiments and the difference between all other experiments and McICA CRF results, in all spectral regions, at TOA and surface, respectively. At TOA, CERES CRF is also shown. We observe a number of interesting features: first, although all 3D experiments have higher positive longwave CRF than both 1D codes, in the shortwave the differences between 1D McICA and 1D with in-region horizontal transport are large, and all 3D experiments fall in between, at both TOA and at the surface, with the exception of the experiment with minimum C_S at the surface at high southern latitudes. This confirms that the in-region horizontal transport effect (which is included in the 1D SPARTACUS run) is stronger than the cloud side horizontal transport effect (which is only included in the 3D runs). As we have reasoned in Section 1.3, the effects are of opposite sign (except for overhead sun) and partially compensate each other in the 3D experiments.

Second, although the 3D experiments show appreciable differences from the 1D in-region horizontal transport run and from each other in both shortwave and longwave

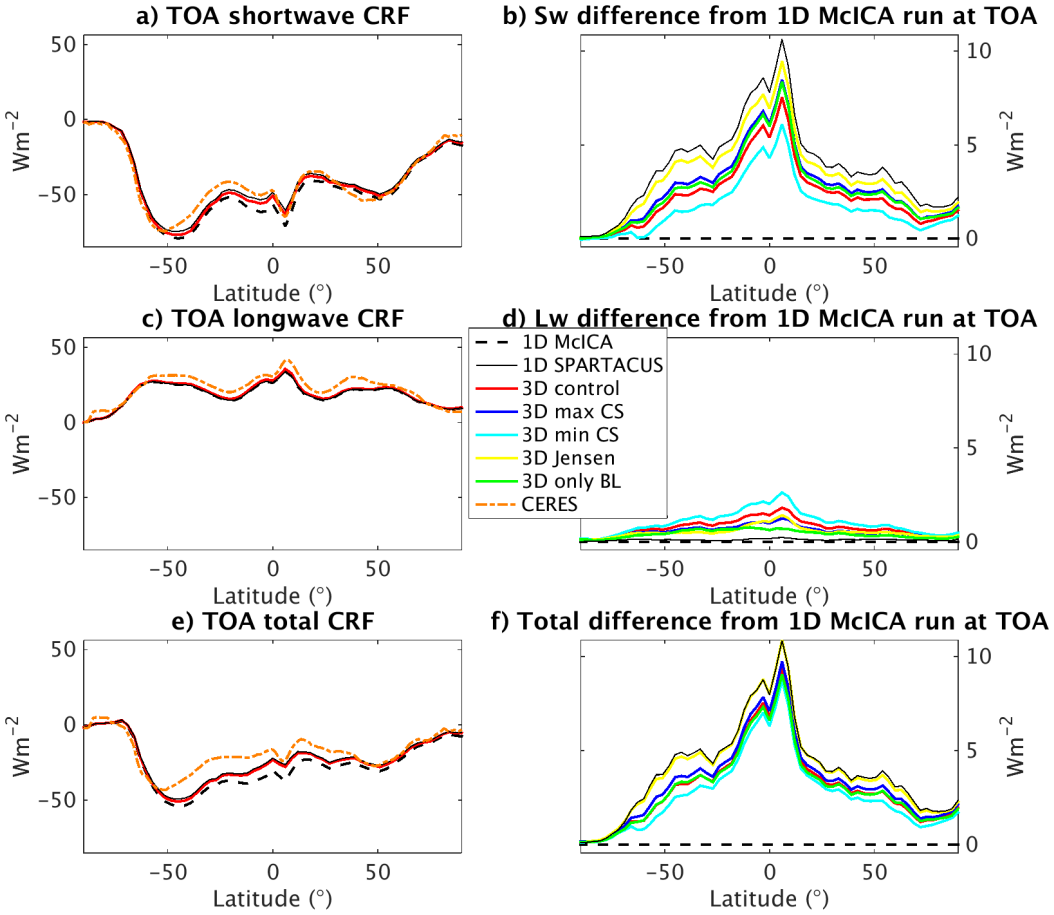

Figure 4.8: (a, c, e) Global annual mean longitudinally averaged CRF at top-of-atmosphere in the 3D control and 1D McICA experiment and in CERES observations for 2000 to 2011. (b, d, f) Difference in annual mean longitudinally averaged TOA CRF between each experiment and McICA, in the shortwave (top row), longwave (second row) and total (third row).

separately (at both TOA and surface), the differences tend to be of opposite sign between the spectral regions. Those 3D experiments showing the strongest negative difference to the 1D in-region horizontal transport run (which is the 3D cloud side effect) in the shortwave also have the largest positive 3D cloud side effect in the longwave. Consequently these differences partly compensate when looking at the overall broadband results: at the surface all codes except McICA agree to within $1\,\mathrm{W\,m^{-2}}$, with somewhat larger remaining differences at TOA.

In general, both CRF and the differences between various codes (the 3D radiative transport effects) show peaks at the mid-to-high latitudes of the storm tracks and in the tropics, particularly at the mean position of the ITCZ (as can also be seen in the global

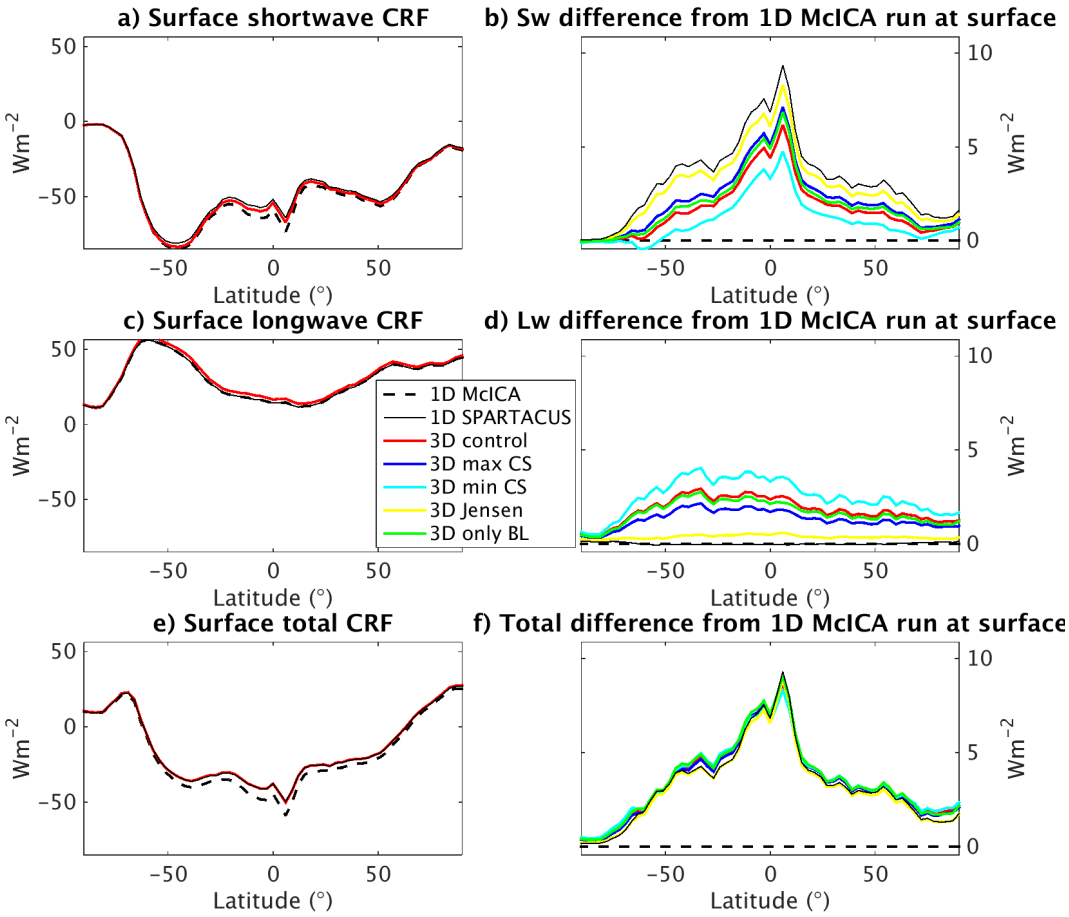

Figure 4.9: As in Figure 4.8, but at the surface and without CERES data.

maps in Figures 4.7 and 4.5), with the marked exception of longwave surface effects, which do not peak in the tropics. There are important hemispheric asymmetries, due to differences in land-sea distribution: south of 70°S, CRF is near zero in the shortwave and very low in the longwave, as this region is over the landmass of Antarctica, where conditions are too cold and dry to form much cloud. Shortwave CRF is also reduced due to the high albedo of the ice-covered surface. Both effects only apply to the Arctic for part of the year, since there is open water in the Arctic in summer. Conversely, in the mid-to-high latitudes between ±30°N and 70°N, both CRF and 3D transport effects in the shortwave, or longwave at the surface, are much stronger in the Southern Hemisphere, where these latitudes contain much more ocean than the corresponding northern latitudes, and ocean has both a lower surface albedo and higher average cloud cover than land. The peaks associated with the ITCZ reflect the latitudinal pattern of annual mean

ITCZ position, and are shifted north from the equator since the mean annual position of the ITCZ lies at about 6°N (e.g. Waliser and Gautier, 1993). These phenomena and their annual cycle will be investigated in more detail in Section 4.3.4.

The differences between the results of the different 3D experiments give a measure of the sensitivity of 3D transport effects to cloud geometry input: as expected, we see the strongest 3D cloud side effects for the experiments with the smallest cloud-scale inputs, which correspond to the largest area of cloud sides. The range of results of the maximum C_S, 3D control and minimum C_S experiments gives the range of uncertainty of 3D cloud side effects we consider most probable, which is less than $\pm 1\,\mathrm{W\,m^{-2}}$ in zonal-mean CRF, while the results of the 3D Jensen C_S run provide the lower bound of 3D cloud side effects from low clouds we regard as possible (while the high cloud effects are the same as in the 3D control run).

Remarkably, the 3D maximum C_S and 3D Jensen C_S runs, which differ by an order of magnitude in the low cloud scale, agree very closely on longwave CRF at TOA, confirming that this effect is overwhelmingly due to high clouds. The two experiments show appreciable differences in shortwave results and most particularly in longwave results at the surface, on which the low clouds have a stronger impact. For these quantities, the 3D Jensen C_S results are closer to those of the 1D SPARTACUS code, showing that the effective cloud scale of 10 km for low clouds as assumed in the Jensen C_S experiment is large enough to remove the majority of low cloud side effects.

The results of the 3D run with cloud side effects only in the boundary layer are quite close to those of the maximum C_S run in the shortwave and for TOA longwave except in the tropics, while the only boundary layer 3D experiment's longwave surface results nearly coincide with the 3D control run. These observations confirm that longwave CRF and its 3D effects at the surface indeed depend almost exclusively on low clouds, while the shortwave cloud side effects and longwave cloud side effects of high clouds at TOA (the difference between the only boundary layer 3D and 3D control experiments) are below $\pm 0.5\,\mathrm{W\,m^{-2}}$. This is because high clouds often have low optical depth in the shortwave, while mean free path in the longwave is commonly so short that effects at each level are dominated by the impact of the nearest cloud layers. High clouds are also larger than boundary layer clouds (with a larger effective cloud scale), reducing their impact on 3D cloud side effects. The strongest impact of high clouds can, unsurprisingly,

be seen in the deep convective region around the ITCZ for TOA longwave effects.

As we have mentioned in Section 4.3.2, including 3D effects (specifically the in-region horizontal transfer effect) improves agreement with CERES observations. Since the improved agreement is due to the in-region horizontal transfer effect, it is also seen in the 1D SPARTACUS run which only includes this effect and no 3D cloud side transport. This improvement is zonally dependent: between 50°S and the equator and north of 80°N, CERES data still shows larger shortwave CRF than the 3D experiment, while between 30°N and 50°N CERES shortwave CRF is actually lower than the results of all models. In-region horizontal transfer is a shortwave effect and therefore does not change the difference between model results and CERES observations in the longwave (which is, however, slightly reduced by longwave 3D cloud side effects). Overall, including 3D effects either improves or leaves unchanged the agreement with total CERES CRF observations at all latitudes; although there is some remaining uncertainty due to the possibility of compensating errors and model tuning.

4.3.4 Annual cycle

Apart from the annual average, it is also instructive to consider the annual cycle of cloud-radiative effects. Figure 4.10 shows the annual cycle of longitudinal averages of CRF in the 3D control run, again for each spectral region and at TOA and surface, depending on latitude and month of the year. There are a number of interesting effects to observe: The strongest monthly and longitudinal-mean CRFs in both shortwave and total occur over the mid-to-high latitudes (about $\pm$35°N to 70°N) in summer, where Southern Hemispheric CRF is the strongest. This is to be expected, as this region in the Southern hemisphere is nearly completely covered in ocean, while the corresponding latitudes in the Northern Hemisphere contain extensive landmasses. Shortwave cloud radiative effects are stronger over ocean since ocean albedo is low and hence the contrast between clear and cloudy albedo is larger, and clouds occur often over the ocean. Conversely, the lack of cloud radiative effect south of around 80°S (south of around 70°S in austral winter) is because there is little cloud there, and because Antarctica is covered with ice and snow, causing a high surface albedo and reducing cloud radiative effects. The same is true for the Arctic outside of boreal summer (in January to April and September to December). Between May and August, however, enough of the Arctic sea ice gives way to open ocean

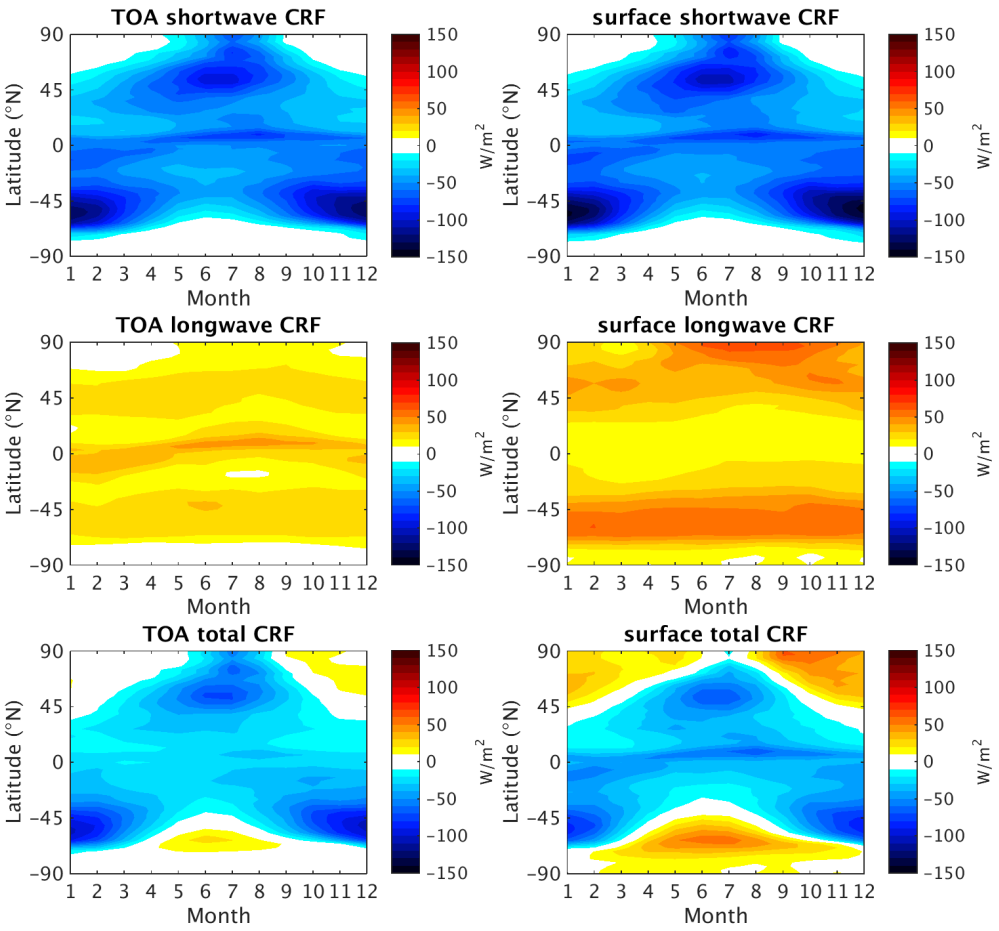

Figure 4.10: Longitudinally averaged net (downwelling - upwelling) cloud radiative forcing at TOA and surface for each month of 2001 in the 3D control run.

to allow for significant shortwave CRF in the Arctic (helped by near-constant insolation).

Another region of high shortwave CRF is the ITCZ, which shifts across the equator in the course of the year. While the peaks in CRF at mid-to-high latitudes are in step with the annual cycle of insolation, the peaks in the Arctic and over the ITCZ occur 1 to 2 months later in the year, presumably since they are due to sea ice melting and circulation changes that take some time to develop.

Again, we see a different distribution of longwave CRF at TOA and at the surface. The position of maximum longitudinally averaged longwave TOA coincides with the ITCZ, and follows the ITCZ's seasonal shift pattern. Secondary peaks occur at the mid-to-high latitudes of the storm tracks in the north Atlantic and north Pacific and over the Southern ocean. At the surface, the highest longwave CRF values in the annual average

occur at these mid-to-high latitudes (strongest over the Southern Ocean). However, for those months when parts of the Arctic ocean are free of sea ice (which reduces thermal emissivity as well as increasing shortwave albedo), the highest monthly values of longwave CRF are seen over the Arctic Ocean. Zonal longwave CRF decreases south of 80°S, particularly in austral winter, as there are very few clouds over inner Antarctica.

This seasonal analysis shows more clearly than the annual mean the times and places where total CRF at TOA turns positive, because longwave CRF dominates over shortwave effects when insolation is low, but temperature and humidity are still high enough for significant cloud occurrence, and not all of the surface is covered in ice. This occurs around 70°S in austral winter, and north of 45°N in the time between when solar insolation reduces in boreal autumn and when the ocean freezes over (hence the peak moves southwards between September and January). As we already saw in the global annual average, TOA longwave CRF partly compensates shortwave CRF over the ITCZ, leaving the mid-to-high latitudes and Arctic in summer as the regions with the strongest negative total TOA CRF. The overall pattern and annual cycle of zonal surface total CRF is somewhat similar. However, surface CRF shows stronger positive total CRF at the high latitudes (nearly cancelling the Arctic shortwave CRF even in summer, and showing a similar seasonal asymmetry pattern based on sea ice cover over the Arctic as at TOA).

Figure 4.11 and Figure 4.12 show the total 3D change on longitudinally averaged CRF Δ_{3D}CRF and 3D cloud side effect $\Delta_{3D\,\text{cloud side}}$ CRF, as seen in the 3D control run with regard to the 1D McICA and 1D SPARTACUS experiments respectively, again shown over the annual cycle, at TOA and surface and for all spectral regions. As in the annual average, the total 3D effect Δ_{3D}CRF when compared to McICA is positive in all spectral regions, adding up to a pronounced total 3D effect. Shortwave Δ_{3D}CRF strongly peaks at the ITCZ, with secondary peaks over summer mid-to-high latitudes and the Arctic in boreal summer. Longwave Δ_{3D}CRF is below $5\,\mathrm{W\,m^{-2}}$ in the zonal average and at TOA peaks in the tropics (some hemispheric asymmetry is likely due to the different distribution of landmasses and therefore of cloudy areas). Again, the distribution is not hemispherically symmetric: Δ_{3D}CRF is stronger in the Southern Hemisphere but very small south of 80°S. Longwave Δ_{3D}CRF varies much less over the annual cycle than in the shortwave.

By contrast, in the 3D cloud side effects compared to the 1D SPARTACUS run, short-

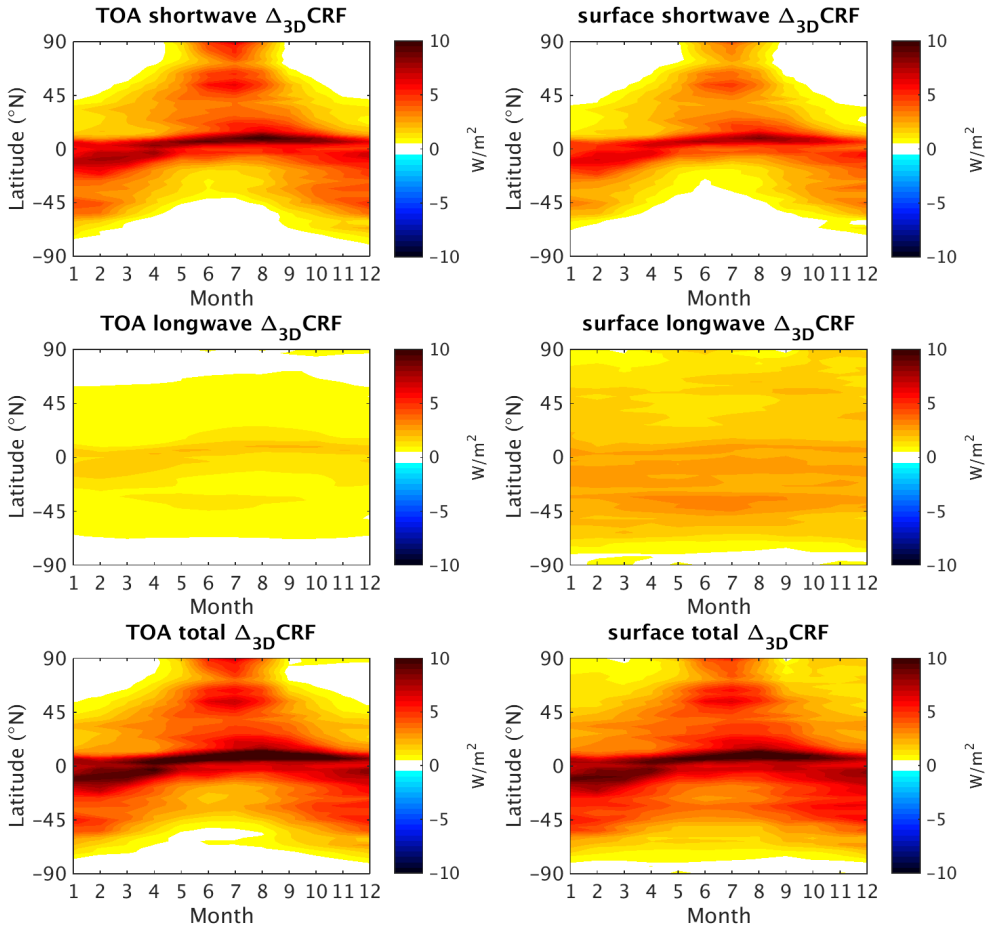

Figure 4.11: Total 3D change in longitudinally averaged net (downwelling - upwelling) cloud radiative forcing Δ_{3D}CRF at TOA and surface for each month of 2001 in the 3D control run relative to the 1D McICA control run.

wave and longwave 3D effects have different signs and partly cancel each other in the total $\Delta_{3D\ \text{cloud side}}$CRF (see Figure 4.12). The maximum absolute values of $\Delta_{3D\ \text{cloud side}}$CRF are also lower that the in-region horizontal transport effect. However, the zonal and annual patterns of the two 3D effects are broadly similar: the strongest (negative) shortwave 3D effects compared to 1D SPARTACUS occur over the ITCZ and mid-to-high latitudes in summer. Both zonal and temporal variation are somewhat weaker than for the total Δ_{3D}CRF with regards to McICA.

Longwave $\Delta_{3D\ \text{cloud side}}$CRFs with regards to both 1D experiments are very close in both value and spatio-temporal distribution (as is to be expected, since we did not include longwave in-region horizontal transport). Comparing the 3D control CRF against

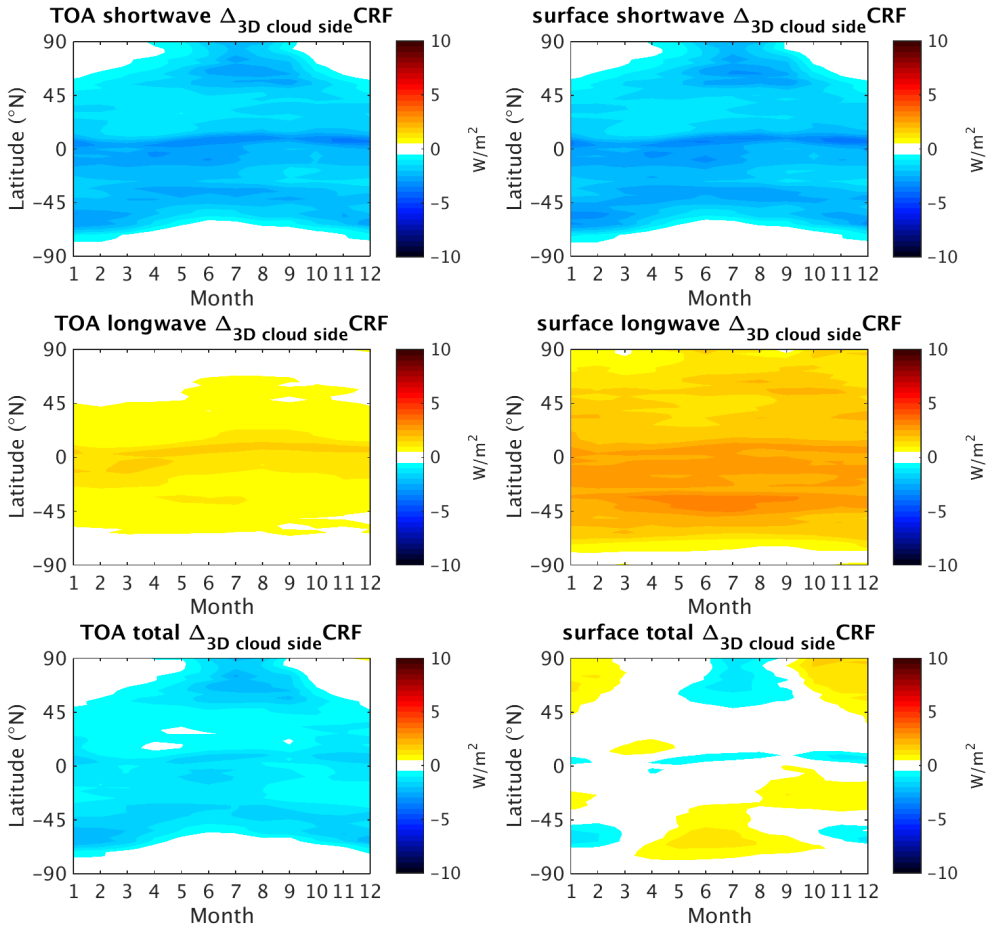

Figure 4.12: 3D cloud side change in longitudinally averaged net (downwelling - upwelling) cloud radiative forcing $\Delta_{\text{3D cloud side}}$CRF at TOA and surface for each month of 2001 in the 3D control run relative to the 1D SPARTACUS solver run.

1D SPARTACUS with in-region horizontal transport shows that this results in negative total zonal average $\Delta_{\text{3D cloud side}}$CRF at TOA of less than $-5\,\text{W}\,\text{m}^{-2}$ at most latitudes, strongest at mid-to-high latitudes in summer and vanishing at high latitudes in winter, but also over some temperate areas. At the surface, total zonal average $\Delta_{\text{3D cloud side}}$CRF is very small nearly everywhere, mostly showing some 3D effect on CRF at high latitudes, positive in winter and negative in summer.

4.3.5 Heating rates

Top-of-atmosphere and surface fluxes provide important information on the Earth's total energy budget and on surface temperature evolution, which determines sensible and

latent heat fluxes that strongly affect atmospheric dynamics. However, the temperature and dynamics of the atmosphere are also strongly influenced by atmospheric heating and cooling rates. Clouds have a strong impact on these heating rates: since the clear-sky atmosphere is nearly transparent to visible light, clouds strongly increase atmospheric heating through shortwave absorption, while also increasing both cooling via longwave emission (at cloud top, especially in low clouds) and heating via longwave absorption of surface emission (at cloud base, especially in high clouds), when compared to the clear sky. It is worth investigating how three-dimensional effects, both of cloud sides and internal radiative transport in regions, modify these effects. We calculate heating rates from the monthly averages of instantaneous radiative fluxes in our experiments. Since mean atmospheric conditions such as temperature, relative humidity and pressure change only slowly over the annual cycle, we feel justified in assuming that pressure and heat capacity at each level are constant during each month at their values seen in the monthly mean atmospheric conditions.

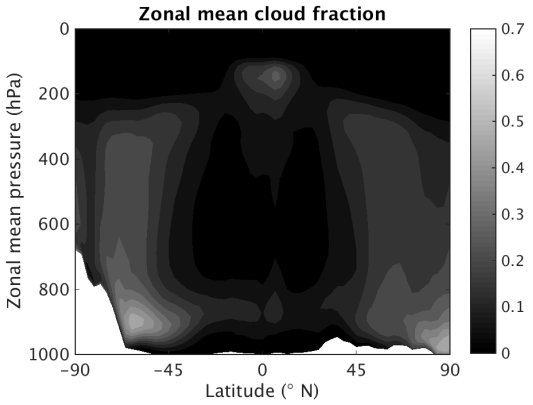

Figure 4.13: Longitudinally averaged annual mean cloud fraction in ERA-Interim in 2001.

Figure 4.13 shows a latitude-pressure section of zonal annual mean cloud fraction in the ERA-Interim data for 2001, showing where clouds are most common and we would therefore expect the strongest cloud effects. Figure 4.14 shows latitude-pressure sections of the total heating rate (in the left-hand column) and the cloud effect on heating rates (in the right-hand column) in each spectral region in the 3D control run, while Figure 4.15 shows latitude-pressure sections of changes in the 3D control run when compared to the 1D SPARTACUS run with horizontal in-region transport (the 3D cloud side effects) and compared to the McICA (the total 3D effects). Both the strongest cloud effects and strongest 3D effects on heating rates are in and below the lowest cloud layer. This is

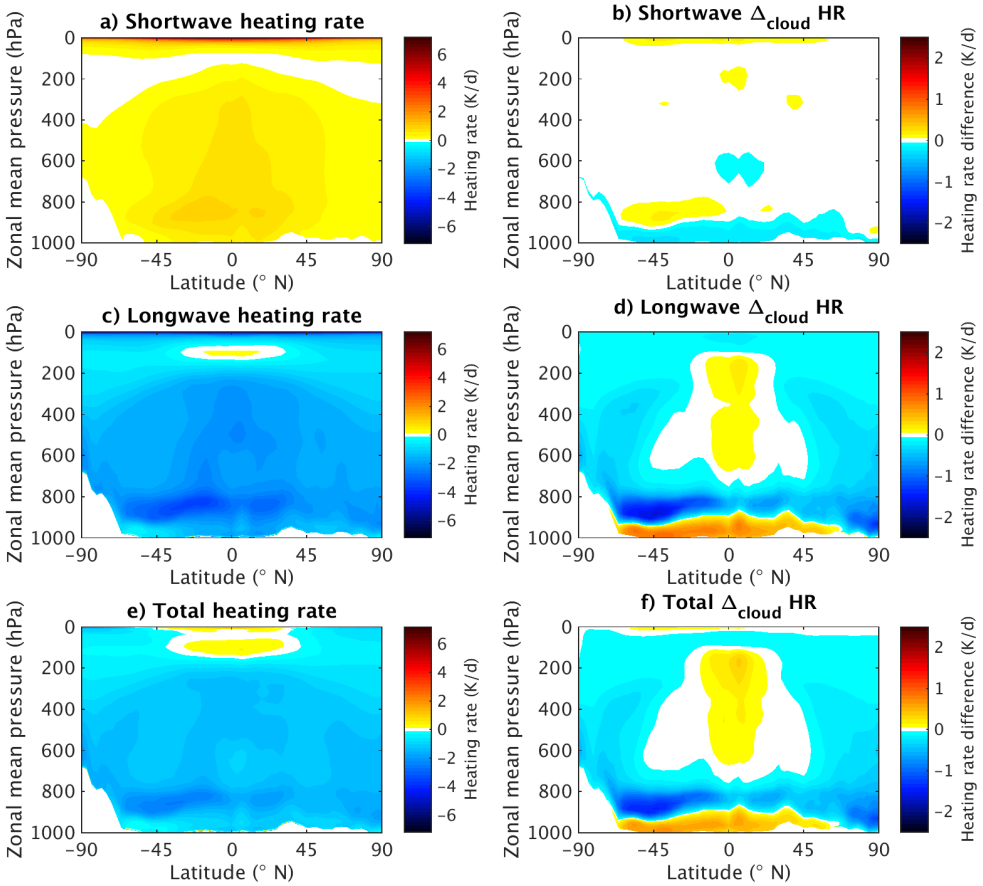

Figure 4.14: (a, c, e) Longitudinally averaged annual mean atmospheric heating rates in 2001 in the 3D control run, in the shortwave, longwave and total spectral regions. (b, d, f) Longitudinally averaged annual mean cloud effect on heating rates Δ_{cloud}HR (heating rates with cloud minus clear-sky heating rates) in 2001 in the 3D control run, in the shortwave, longwave and total spectral regions. Please note different colour scales.

unsurprising, since this is not only the most consistently cloudy layer (especially in the middle and high latitudes, as seen in Figure 4.13), but these low clouds also tend to be optically thick in both longwave and shortwave and comparatively warm, causing high longwave emission. As we found in Chapter 3, these low clouds also tend to be smaller and more broken (which is expressed via a smaller radiative effective cloud scale C_S of 1 km), increasing 3D cloud side effects.

The dominant cloud effect is longwave cooling by emission within the low cloud layer, and longwave heating below due to radiation from the surface absorbed by the cloud layer. 3D effects (specifically cloud side effects, as in-region transport effects are assumed to be negligible in the longwave) further increase these effects through cloud

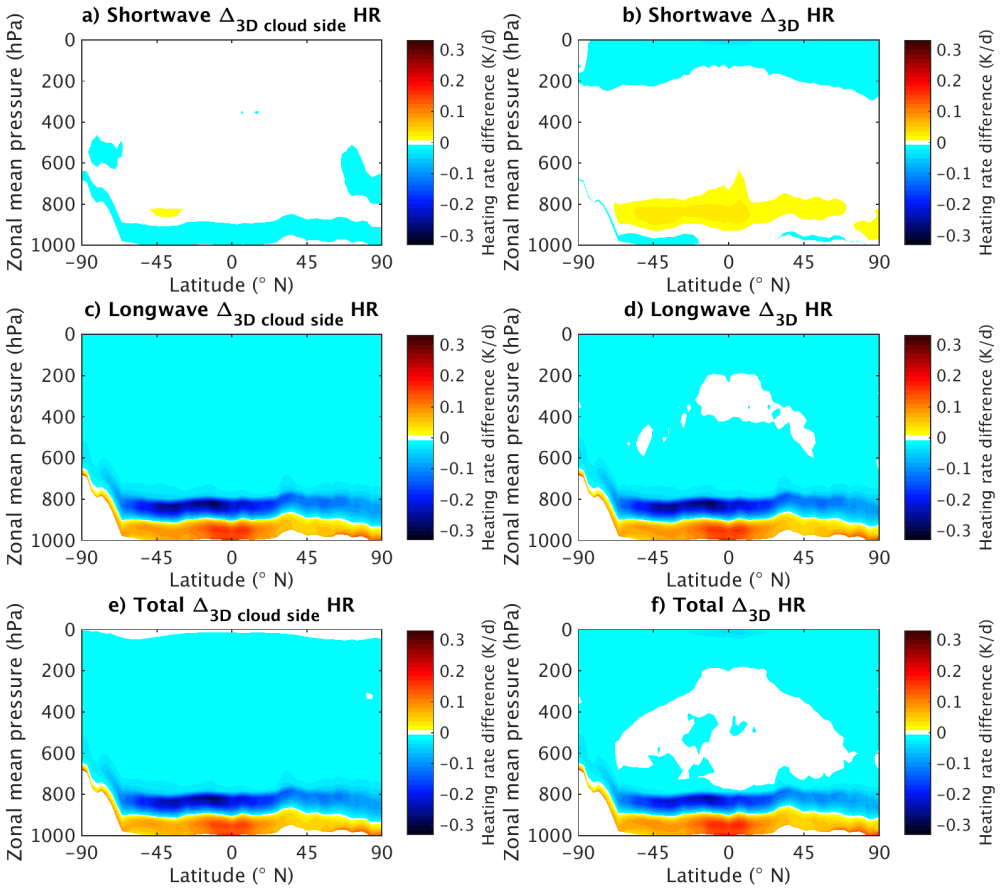

Figure 4.15: (a, c, e) 3D cloud side change in longitudinally averaged annual mean atmospheric heating rates $\Delta_{\text{3D cloud side}}$HR in 2001 in the 3D control run compared to the 1D SPARTACUS run with horizontal in-region transport, in the shortwave, longwave and total spectral regions. (b, d, f) Total 3D change in longitudinally averaged annual mean heating rates Δ_{3D}HR in 2001 in the 3D control run compared to the McICA run, in the shortwave, longwave and total spectral regions.

side emission and interception. Longwave cooling can also be observed in higher cloudy layers up to 10 km in the mid-to-high latitudes, while the high cloud layers in the tropics show longwave heating. We hypothesise that this is because there is little mid-level cloud in the tropics, so that most of the longwave radiation emitted upwards by the surface or low, warm clouds reaches the high clouds between 10 and 20 km height, where much of it is absorbed and causes longwave heating. This heating dominates over the cooling caused by the comparatively low emission from these cold high clouds. At the higher latitudes, on the other hand, layers with high mean cloud fraction are vertically continuous. This suggests that much of the upward radiation emitted at each level of

the atmosphere is absorbed within a few layers above. Since the temperature difference between near layers is much less than that between the warm surface in the tropics and cold high tropical clouds, heating from the absorbed radiation (which is only a fraction of the upward flux emitted in a layer) is not enough to overcome cooling from longwave emission by the absorbing layers.

Absorption by high tropical clouds leads to longwave cooling in the tropical stratosphere above when compared to clear-sky heating rates, since less upwelling longwave radiation reaches these heights. Longwave 3D cloud side effects are not strong above the lowest cloud layer, presumably because the high clouds have less cloud edge, with an effective cloud scale of $C_S = 10\,\text{km}$.

Shortwave atmospheric heating rates are generally weaker than in the longwave in the troposphere. Low clouds absorb shortwave radiation, causing heating within the cloud layer and cooling below, relative to clear skies. These effects are slightly increased by 3D cloud side effects (as seen in Figure 4.15a), and heating is also increased by in-region horizontal transfer (demonstrated by the fact that the heating increase due to both 3D cloud side and in-region transfer effects seen in Figure 4.15b is stronger than the 3D cloud side effect alone in Figure 4.15a). Clouds also cause shortwave heating in the stratosphere, as radiation reflected up from the clouds is absorbed in the ozone layer. This effect is somewhat increased by 3D cloud side effects, but in-region transfer effects, which reduce overall cloud reflectivity (as discussed in Section 1.3), cause an even stronger reduction, leading to an overall reduction of stratospheric shortwave heating in the 3D control run compared to the McICA run in Figure 4.15b.

In total, the effect of clouds on the higher layers of the atmosphere consists of radiative cooling at the high latitudes, radiative heating in the tropical highest cloud layers and some heating in the stratosphere above. These effects are not precisely hemispherically symmetric in the annual mean, partly due to asymmetries in mean cloud cover (see Figure 4.13). The peak in tropical high-cloud heating lies around 6° north of the equator, coinciding with the mean position of the ITCZ, while shortwave cloud effects are generally stronger over the Southern Hemisphere, which contains more low-albedo ocean and thus provides a stronger contrast between clear and cloudy skies. 3D cloud side effects (seen in the left-hand column of Figure 4.15) are dominated by an increase of longwave heating in the lowest cloud layer and cooling below, while the shortwave

effects (of opposite sign in and below the low cloud layer, and increasing stratospheric heating) are too weak to change the total 3D effect much. When considered together with the in-region horizontal transfer effect, the total 3D effect (in the right-hand column of Figure 4.15) is still dominated by increased longwave heating in the lowest cloud layer and cooling below, but also shows some cooling of the stratosphere due to decreased overall cloud reflectivity.

The zonal distribution of both the clouds and the heating rate changes they cause changes over the course of the annual cycle. Figure 4.16 shows the cloud distribution for four individual months, sampling the annual cycle. Figures 4.17 and 4.18 show the heating rate changes due to clouds, Δ_{cloud}HR, in the 3D control run (in the left-hand columns) and the total 3D effects compared to the McICA run, Δ_{3D}HR, (in the right-hand columns) in June and December. In general, the whole pattern of heating rate changes shifts north in boreal summer and south in boreal winter. However, both polar regions in their respective summer show much stronger shortwave heating within the high clouds than the annual average, nearly compensating the longwave cooling. The patterns in September and March are closer to that of the annual average (not shown).

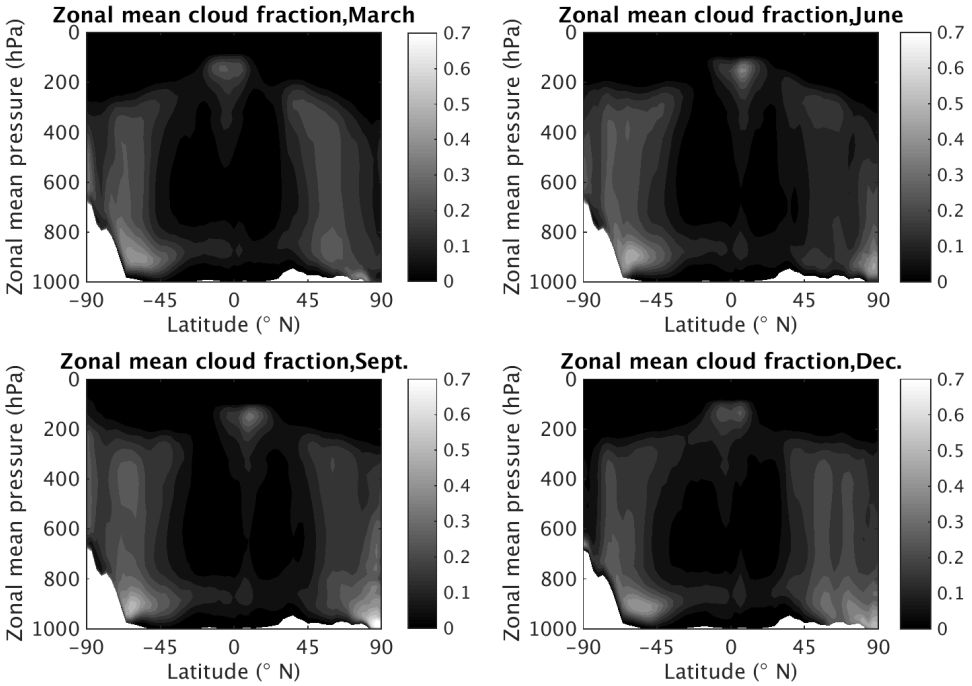

Figure 4.16: Longitudinally averaged monthly-mean cloud fraction in ERA-Interim in March, June, September and December 2001.

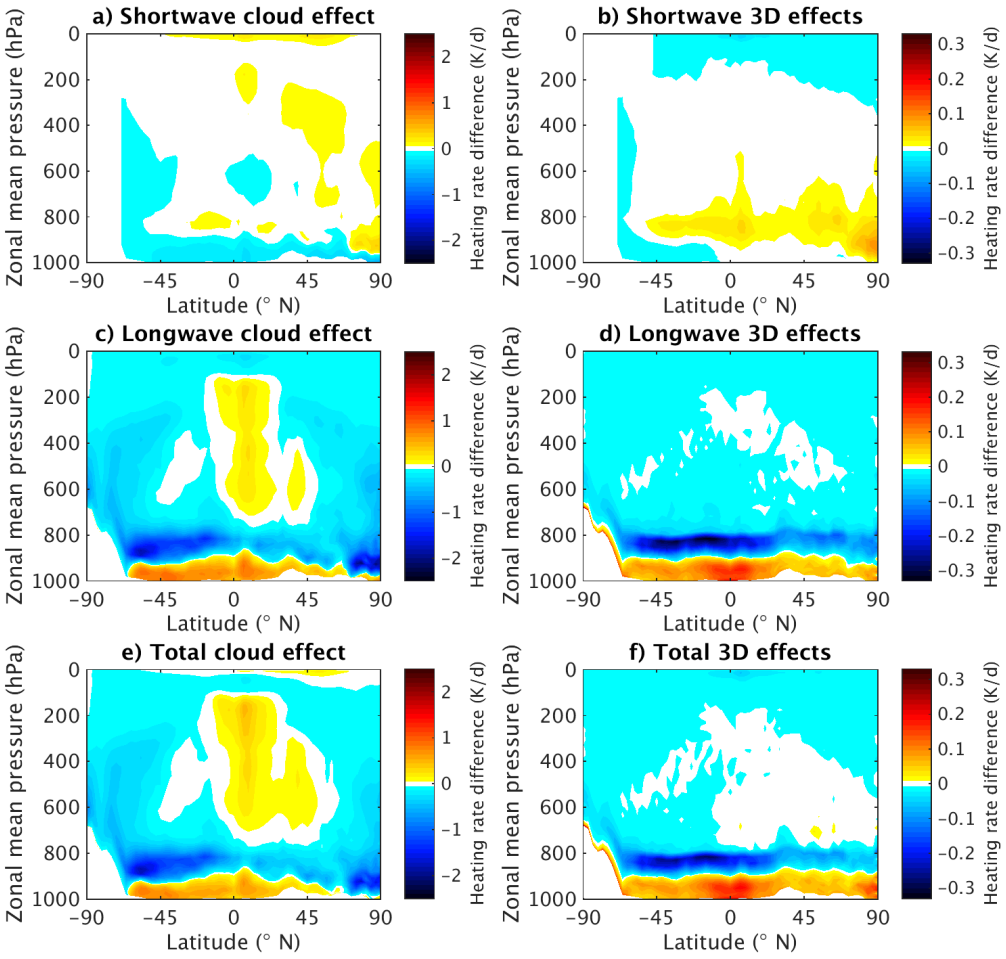

Figure 4.17: (a, c, e) Longitudinally averaged monthly-mean cloud effect on atmospheric heating rates Δ_{cloud}HR (heating rates with cloud minus clear-sky heating rates) in June 2001 in the 3D control run, in the shortwave, longwave and total spectral regions. (b, d, f) Total 3D change in longitudinally averaged monthly-mean cloud effect on heating rates Δ_{3D}HR in June 2001 in the 3D control run compared to the McICA run, in the shortwave, longwave and total spectral regions. Please note different colour scales.

For December, we can compare our heating rate results in the shortwave to those of Cole et al. (2005), who estimated the change between a 2D radiation calculation (as approximation for 3D) and an ICA experiment. In order to facilitate comparison, we have plotted the total change in our shortwave heating rates between the 3D control and McICA runs in December against pressure in as similar a manner as in Cole et al. (2005) as possible (comparison in Figure 4.19).

Some of the distribution of heating rate differences due to 3D effects in latitude and pressure we find is similar to that seen by Cole et al. (2005) for 2D calculations, like the

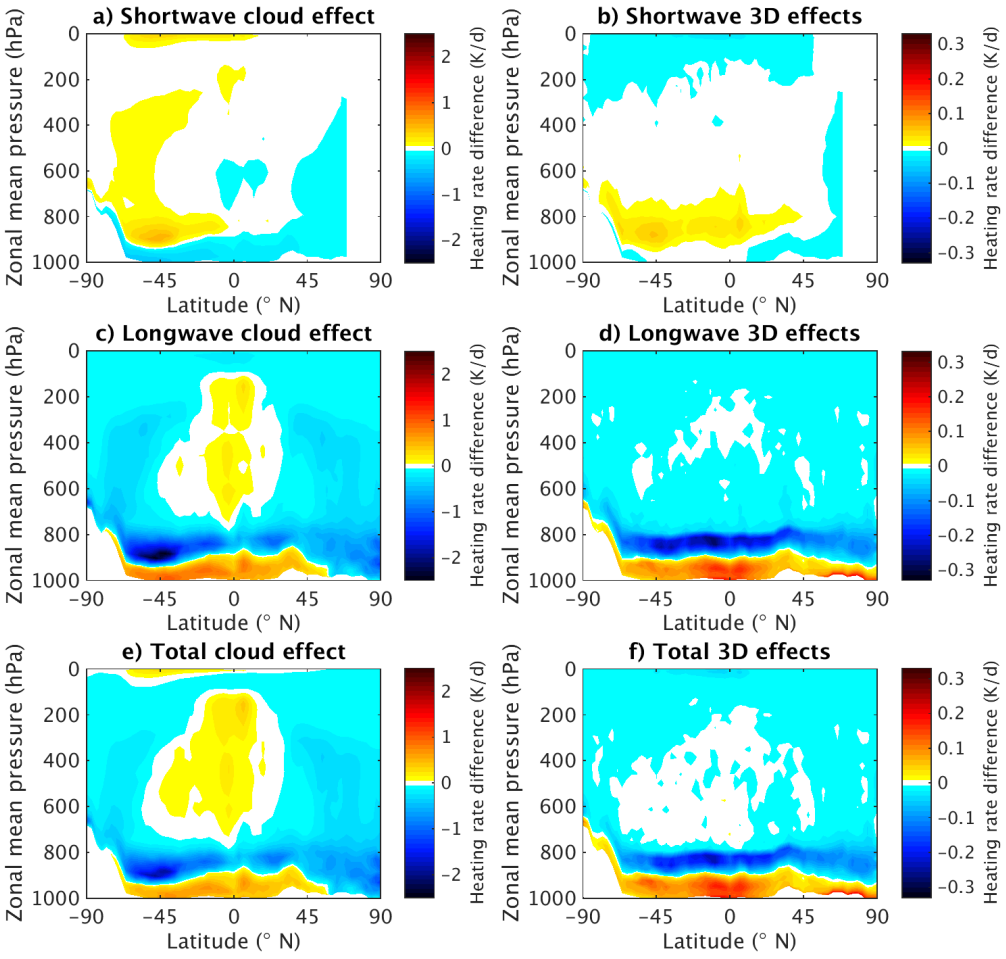

Figure 4.18: (a, c, e) Longitudinally averaged monthly-mean cloud effect on atmospheric heating rates Δ_{cloud}HR (heating rates with cloud minus clear-sky heating rates) in December 2001 in the 3D control run, in the shortwave, longwave and total spectral regions. (b, d, f) Total 3D change in longitudinally averaged monthly-mean cloud effect on heating rates Δ_{3D}HR in December 2001 in the 3D control run compared to the McICA run, in the shortwave, longwave and total spectral regions. Please note different colour scales.

peak in positive 3D (or 2D) effect near the equator (although it extends further up in Cole et al.'s figure), or the negative 3D effect in the Southern Hemisphere's stratosphere and at the surface south of 60°S and between 20°N and 60°N. There are a number of marked differences as well: for one, we find a very strong positive low cloud effect over the Southern Ocean storm track, which does not appear in Cole et al.'s data. On the other hand, they see a strong positive effect at around 80°S to 90°S and 500 hPa and a somewhat weaker peak at 80°S and 850hPa, that we do not see. In our experiment the reduction in high cloud effect away from the equator is less marked, and the equatorial

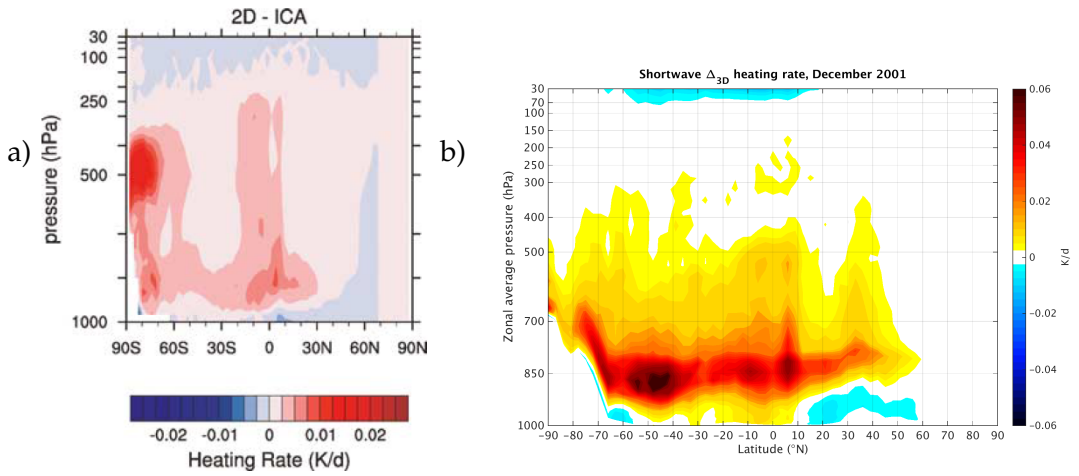

Figure 4.19: a) Monthly-mean cross section of differences in shortwave atmospheric heating rates between 2D radiative transfer and ICA for December 2000 as a function of latitude and pressure, from Cole et al. (2005). b) Monthly and longitudinal-mean 3D effect on shortwave heating rates, Δ_{3D}HR for December 2001 in our 3D control run compared to the McICA run.

peak lies slightly farther north, while our low cloud positive effect also extends further north.

These differences could be due to different clouds, as the two cases are in different years and the cloud input from ERA-Interim we used is different from the super-parametrisation model used by Cole et al. (2005). Our low cloud effects are generally stronger, which we would expect since both the low resolution of cloud fields of 4 km and the use of 2D rather than 3D calculations by Cole et al. (2005) would tend to reduce the 3D effect.

4.4 Conclusions on global impact of 3D cloud-radiation effects

We have here for the first time presented systematic global estimates of the various changes to radiative fluxes and heating rates due to 3D cloud-radiation interactions and in each spectral region. The effects divide into 3D cloud side effects and in-region horizontal transport effects. Neither of these are taken into account in ICA schemes, but region-based 1D two-stream schemes (including the 1D SPARTACUS solver) allow in-region horizontal transfer. For our experiments, we have used ERA-Interim atmospheric data for the year 2001 as input, together with the effective cloud scale estimates we derived in Chapter 3. We have calculated the 3D cloud side effects (as the difference between the 3D experiments and the 1D SPARTACUS run) and in-region horizontal trans-

port effect (as the difference between 1D SPARTACUS and McICA) on their own, and the total 3D effect.

We find that while the longwave 3D cloud side effects on net radiative fluxes at TOA or surface are always positive, increasing the longwave cloud radiative effect, the shortwave 3D cloud side effects vary with solar zenith angle. For overhead sun, cloud side leakage has a positive effect, reducing the negative shortwave cloud effect, while for low sun, cloud side interception enhances the negative shortwave cloud radiative forcing. In the annual mean, it is this negative cloud side interception effect that is strongest, dominating over the cloud side leakage effect and at TOA also over the longwave effect, leading to a negative total 3D cloud side effect of $-1.0\pm0.5\,\mathrm{W\,m^{-2}}$ in the global average, while shortwave and longwave 3D cloud side effects nearly compensate at the surface.

The shortwave in-region horizontal transfer effect, on the other hand, is positive, decreasing global annual-mean cloud reflectance at TOA by $5.0\,\mathrm{W\,m^{-2}}$. This effect is stronger than the shortwave 3D cloud side effects, leading to total 3D effects on CRF that are positive in both the longwave and the shortwave and decrease the negative total CRF by $4.0\pm0.5\,\mathrm{W\,m^{-2}}$ at TOA and $4.36\pm0.03\,\mathrm{W\,m^{-2}}$ at the surface, where the uncertainty range represents the uncertainty due to our range of cloud scale estimates only (other uncertainties are harder to quantify). These changes to CRF are somewhat larger than the radiative forcing of anthropogenic greenhouse gases since pre-industrial times of 2.54 to 3.12 $\mathrm{W\,m^{-2}}$ (Myhre et al., 2013).

The results are not very sensitive to the effective cloud scale input. 3D effects on CRF estimated using our uncertainty range of cloud scales vary by around 40% or less. Zonal mean shortwave CRF results for all 3D experiments we conducted, including those allowing 3D effects only in the boundary layer or using the much larger effective cloud scale estimated from coarse MODIS data by Jensen et al. (2008), fall within the spread of 1D models between the CRF seen in McICA calculations and when using the 1D SPARTACUS solver, which is a region-based 1D two-stream scheme.

Indeed, since when averaged over long timescales, longwave and shortwave 3D cloud side effects on net fluxes nearly compensate each other, the 3D CRF results averaged in time and space are quite close to those of the traditional two-stream 1D SPARTACUS solver (especially at the surface). Therefore, in contexts where only total time-averaged net fluxes at TOA or surface are important, a cheaper alternative to using 3D

SPARTACUS in climate models would be to use a scheme that only includes the shortwave in-region transport effect, like a traditional two-stream scheme, which results in similar total fluxes on average. However, with this method, there are still differences of up to $3\,\mathrm{W\,m^{-2}}$ to the 3D results in the average longwave and shortwave CRF results separately, and also significant differences in the heating rates, especially in and below the lowest cloud layer. This is because in general, 3D effects on atmospheric heating rates are stronger in the longwave than the shortwave, and are mostly due to 3D cloud side effects. 3D effects (as all cloud effects) on radiative heating are strongest in and below the lowest cloud layer, and zonal mean additional heating below this layer due to 3D effects can be up to $0.2\,\mathrm{K\,d^{-1}}$, while additional cooling in the layer can be up to $-0.3\,\mathrm{K\,d^{-1}}$. Shortwave in-region transport effects cause an opposite, but much weaker, heating rate change in these layers, while the reduction in reflected shortwave radiation in the upper atmosphere also causes some stratospheric cooling.

1D region-based two-stream schemes are also not a good approximation when instantaneous fluxes instead of long-term averages are considered, because the opposite shortwave cloud side effects for different solar zenith angles do not compensate. Thus, in contexts that depend on response to radiative fluxes on timescales of days or less, like short and medium-range weather forecasts, we would ideally use 3D SPARTACUS in both longwave and shortwave to obtain radiative fluxes that are as correct as possible.

Overall, the 3D effects are similar in magnitude to anthropogenic greenhouse gas forcing, and would therefore be worth including in climate models. Compared to both 3D and region-based 1D schemes, McICA methods overestimate cloud reflectivity because they neglect in-region horizontal transfer. Region-based two-stream schemes that only consider one cloudy region also overestimate cloud reflectivity since they neglect in-cloud horizontal structure. 3D SPARTACUS together with Tripleclouds therefore provides a very useful method to avoid both these reflectivity biases. As a cheaper approximation in cases where only time-averaged total fluxes are of interest, 1D region-based two-stream schemes could be used, but they cause significant errors in spectral fluxes, instantaneous fluxes and heating rates.

Chapter 5

Summary, conclusions and future work

In global weather and climate models, radiation is treated in a one-dimensional way, travelling in the vertical only. We need to understand the errors caused by neglecting the complex interaction of radiation with the 3D structure of clouds in reality and determine their global impact. This requires a radiation model that can represent the important 3D cloud-radiation effects in an efficient enough way to be able to run globally, as well as a cloud geometry parametrisation that provides the required information on 3D cloud shapes, overcoming a lack of globally available three-dimensional observations. More concretely, our work addresses three key questions:

1. How can we represent 3D effects, particularly in the longwave, in a numerically efficient radiative transfer model?

2. How can cloud size best be characterised for radiative transfer?

3. What is the global impact of 3D cloud-radiation interactions?

We have incorporated 3D cloud effects into the one-dimensional SPARTACUS radiation model (whose longwave part we have developed in this thesis) and evaluated it against fully 3D calculations to address the first question. We have also derived a cloud size parameter, the *effective cloud scale*, that together with the cloud parameters in a global model fully characterises cloud geometry for radiation purposes and only depends on cloud type. These developments have allowed us to conduct a set of global offline radiation calculations on atmospheric conditions from a year-long set of ERA-Interim reanalysis data from which we can estimate not only the global impact of 3D cloud effects on radiative fluxes and heating rates in each spectral region but also their global and zonal distribution, annual cycle and sensitivity to effective cloud scale.

In general, all 3D effects have been investigated together in previous studies, and longwave effects have often been neglected. However, several different 3D effects of similar magnitude occur in the longwave and in the shortwave at different solar illumination angles, caused by different physical mechanisms and features of cloud geometry, as we have described in Section 1.3. These 3D effects can partly compensate, depending on the geometry of the sun and clouds, which is why only considering the total 3D effect can be misleading. In particular, we find that one 3D effect that has previously rarely been investigated is noticeable: the effect of shortwave horizontal transfer between parts of the same region that overlap differently with other vertical layers. While other 3D effects change sign between different spectral regions or times of day, the in-region horizontal transport effect uniformly decreases cloud reflectance, and therefore has a significant warming effect in the long-term global average. By conducting global experiments with several radiation models that include different subsets of 3D effects, we can distinguish their separate impact.

5.1 How can we represent 3D effects in a numerically efficient radiative transfer model?

We have developed the longwave part of the SPARTACUS model to represent 3D cloud effects, both due to radiative transport across cloud sides and internal horizontal transport in regions, in the shortwave and longwave spectral intervals. The scheme can incorporate treatment of horizontal cloud inhomogeneity using the Tripleclouds method of Shonk and Hogan (2008), thus avoiding two alternative errors in common current radiation schemes that both lead to an overestimation of cloud reflectance, either due to neglecting cloud inhomogeneity in region-based schemes or due to incorporating inhomogeneity but neglecting horizontal transfer within regions in ICA schemes.

For idealised cubic clouds, we can determine 3D cloud-side effects theoretically, thus providing an important guide for the development of SPARTACUS and test case for evaluation. We find that longwave cloud emission is underestimated by a factor of exactly three if cloud-side effects are neglected for an optically thick cubic cloud. Reference to this test case has also allowed us to evaluate SPARTACUS model mechanics like the estimate of the best effective direction assumed for the radiative stream that treats hori-

zontal transport of diffuse radiation. The best estimate of effective direction is different to the effective direction assumed for the vertical streams in two-stream models, because the dependence of radiance on direction that is approximated by the effective direction is different in both cases. We have also found that due to build-up of emitted radiation and scattering, the horizontal distribution of longwave fluxes within clouds can be non-homogeneous even in homogeneous clouds. We have derived a functional description of the difference between radiative flux at cloud sides and in-cloud average flux depending on cloud optical and geometric parameters, which is relevant for determining the correct total emitted flux at cloud sides.

Taking account of these geometric effects and their impact on horizontal radiative transfer, SPARTACUS reproduces well radiative fluxes from fully 3D calculations in both idealised and realistic test cases and the theoretical values for the cubic cloud, in a manner efficient enough for a global weather and climate model. The scheme has been implemented by Hogan et al. (2016) for use in ECMWF's global Integrated Forecast System (IFS) model.

5.2 How can cloud size best be characterised for radiative transfer?

The information about cloud geometry SPARTACUS requires is the *radiatively relevant* cloud edge length in a model gridbox at a given height. This parameter can be measured as the cloud edge length once the cloud field is smoothed at scales up to that of radiative smoothing. Clustering of clouds increases interception of radiation from neighbouring clouds and can decrease the effective amount of cloud edge. Since the cloud edge length depends strongly on cloud fraction, it is not a very useful parameter to compare between different cloud scenes. We have derived a new parameter, the effective cloud scale C_S, that is a measure of cloud edge in a cloud field and is independent of cloud fraction, only depending on cloud type. This allows global specification of effective cloud scale for each cloud type, which provides the only cloud geometry variable necessary for SPARTACUS in addition to those provided in a global model.

We have analysed high-resolution 3D cloud cases from both cloud radar observation and cloud-resolving models to derive typical values of cloud scale for various cloud

types. We found that cloud scales for different boundary layer clouds are remarkably similar, and also do not differ between the cloud fields from simulations and observations we investigated. This allows us to adopt a unified cloud scale value for all boundary layer clouds of $C_S = 1.0 \pm 0.4$ km. Higher clouds tend to be larger than boundary-layer clouds and contain fewer cloud edges in the same area of cloud scene. The variation between the very different types of mid-level and high cloud, like thin cirrus clouds and cumulonimbus anvils, is much larger than for boundary-layer clouds. However, due to the limited number of available high cloud cases, we could not distinguish effective cloud scale values for the separate high cloud types beyond the range of uncertainty. This would be an interesting question for future work. We have established that a cloud scale range of 5 to 20 km with a best estimate of $C_S = 10$ km covers the higher uncertainty for high clouds.

We represent cloud clustering in a simplified manner by an empirical reduction factor of 0.7 to cloud edge length and a corresponding increase in effective cloud scale. There is considerable uncertainty in this approach, and we have included this uncertainty in our estimate of minimum and maximum effective cloud scales for our experiments to ensure that any insufficient representation of cloud clustering does not lead to an overestimation of 3D cloud effects.

5.3 What is the global impact of 3D cloud-radiation interactions?

Thus equipped with an efficient global radiative transfer model and the cloud geometry input to provide to it, we have conducted global radiation calculations on a year-long atmospheric re-analysis data set. This allowed us, for the first time, to comprehensively determine the global impact of each 3D cloud effect on radiative fluxes and heating rates, while the atmospheric response to these changes would be a subject for future research. The year-long experiment with calculations for four global scenes per day allowed us to investigate both instantaneous and time-averaged 3D effects and their annual cycle, and could in future also be analysed with respect to the diurnal cycle. We separated different 3D effects by considering spectral regions separately and by comparing to several one-dimensional calculations that included and excluded different 3D effects. Thereby we could judge the separate impact of cloud-side and in-region horizontal transport effects,

in the longwave and in the shortwave. We tested sensitivity of radiation results on effective cloud scale input by repeating the 3D SPARTACUS experiments with cloud scales representing the range of uncertainty.

We found that 3D cloud-radiation effects are significant even on a global scale in shortwave, longwave and total radiation results. Overall, these 3D interactions decrease the magnitude of the cooling shortwave cloud effect, but increase the warming cloud effect in the longwave, both of which mechanisms act to warm the Earth and reduce the total global-mean negative effect of clouds on net downward radiative fluxes by around 3.5 to 4.4 $\mathrm{W\,m^{-2}}$ or 15 to 18 %. In the longwave and for atmospheric heating rates, the impact of 3D cloud-side effects is dominant, which increases both longwave heating below clouds by up to 0.2 $\mathrm{K\,d^{-1}}$ and cooling in low clouds by up to $-0.3\,\mathrm{K\,d^{-1}}$. Shortwave 3D cloud-side effects change sign depending on solar zenith angle and partly cancel over the course of the day and against the longwave cloud-side effects. This is why total global time-averaged 3D cloud side effects are below 1.5 $\mathrm{W\,m^{-2}}$ at TOA and close to zero at the surface, although time-averaged cloud-side effects in shortwave and longwave separately amount to between $-3\,\mathrm{W\,m^{-2}}$ and 3 $\mathrm{W\,m^{-2}}$. Shortwave cloud-side effects can be significant for instantaneous fluxes at overhead or low sun, however.

For net fluxes at top-of-atmosphere or at the surface and in the shortwave spectral region, the strongest time-averaged 3D effect is due to horizontal in-region transport, which increases net downwelling fluxes by 4 to 5 $\mathrm{W\,m^{-2}}$. This is remarkable, as this effect has previously rarely been investigated, and also because it is an effect that is implicitly represented in traditional region-based one-dimensional radiative transfer models. However, in-region horizontal transport is suppressed in the McICA radiation schemes that are widely used in current state-of-the-art radiative transfer models, causing significant errors in net fluxes in the shortwave in these current models. Neglecting horizontal in-region transfer artificially increases cloud reflectance, leading to an overestimation of radiation reflected out of the Earth's atmosphere and an underestimation of radiative heating in the troposphere and at the surface.

Traditional region-based 1D two-stream schemes can roughly capture the total change in time-average net fluxes due to horizontal in-region transfer, but they are incapable of reproducing 3D cloud side effects, which dominate instantaneous 3D effects and their short-term impact. This inclusion of only part of the 3D effects also still causes

errors in fluxes in each separate spectral region and in heating rates. The use of these region-based 1D schemes could therefore be used as a numerically cheap approximation only in specific contexts where long-term average total net fluxes are the only variables of interest. The SPARTACUS method can accurately capture both in-region horizontal transport and 3D cloud side effects, at a numerical cost of around 3 times that of a region-based 1D scheme or 4 times that of a McICA scheme.

The 3D effects depend on the effective cloud scale provided as input, but are not extremely sensitive. The generous uncertainty range of cloud scale we tested led to a variation in 3D effects of maximum 40 % and much less in most cases. Boundary-layer clouds have stronger 3D effects than high clouds which we explain with their high optical depth and small physical size.

5.4 Future work

Several further questions arise from this study as challenges for future work:

- Can the SPARTACUS model be further improved, either by increasing precision or by enhancing efficiency, possibly through further approximations? The best trade-off between precision and speed will depend on the particular application.
- Can analysis of a wider range of cloud cases improve the precision and confidence of the effective cloud scale parametrisation globally? Variation between different cloud types might be represented using the distinction between stratiform and convective cloud made in many global models, like the IFS.
- What would be a more rigorous representation of the reduction of effective cloud edge length by cloud clustering? Since the relevant parameter for interception of radiation by neighbouring clouds is the average path length of radiation between clouds, this could potentially be described using a mean gap length as utilised in the cloud statistics of Alexandrov et al. (2010b,a). This parameter would then have to be parametrised globally based on the available cloud information, as we have done with the effective cloud scale.
- Can confidence in both the SPARTACUS model and the cloud geometry parametrisation be increased through comparison against fully 3D radiation calculations

in a wider range of cases, ideally involving a range of different cloud types and multi-layer cloud? Our validation of SPARTACUS has so far been confined to idealised clouds and realistic cumulus cases. It would be interesting to evaluate both the model and the cloud geometry parametrisation for a wider range of different clouds, especially multi-layer clouds with their more complex geometry. Such a study will depend on the availability of both 3D cloud fields and fully 3D radiation calculations to compare against.

- What is the impact of the SPARTACUS radiation model on forecast skill in numerical weather prediction? What model tuning adjustments might not be necessary any longer once 3D effects are included?

- How do clouds and atmospheric dynamics in general respond to the changes in radiative fluxes and heating rates due to 3D cloud-radiation effects? What is the dynamic feedback on 3D cloud-radiation interaction? Determining the atmospheric feedback will require running a full general circulation model interactively with the SPARTACUS radiation scheme. In order to correctly account for changes in surface heating, the simulation will need to utilise a coupled atmosphere and ocean model, adding an additional level of complexity and potentially presenting a challenge for determining the response to 3D cloud-radiation interaction to a good statistical significance.

These and further questions will provide ample scope for ongoing and future work on understanding the wider impact of 3D cloud-radiation effects.

Bibliography

Albrecht, B. A., C. S. Bretherton, D. Johnson, W. H. Scubert, and A. S. Frisch, 1995: The Atlantic stratocumulus transition experiment — ASTEX. *Bull. Amer. Meteor. Soc.*, **76**, 889–904.

Alexandrov, M. D., A. S. Ackerman, and A. Marshak, 2010a: Cellular statistical models of broken cloud fields. Part II: Comparison with a dynamical model and statistics of diverse ensembles. *J. Atmos. Sci.*, **67**, 2152–2170.

Alexandrov, M. D., A. Marshak, and A. S. Ackerman, 2010b: Cellular statistical models of broken cloud fields. Part I: Theory. *J. Atmos. Sci.*, **67**, 2125–2151.

Allan, R. P., 2011: Combining satellite data and models to estimate cloud radiative effect at the surface and in the atmosphere. *Meteorological Applications*, **18**, 324–333.

Allan, R. P. and M. A. Ringer, 2003: Inconsistencies between satellite estimates of longwave cloud forcing and dynamical fields from reanalyses. *Geophys. Res. Lett.*, **30**.

Arakawa, A. and W. H. Schubert, 1974: Interaction of a cumulus cloud ensemble with the large-scale environment, Part I. *Journal of the Atmospheric Sciences*, **31**, 674–701.

Baran, A. J., P. Hill, K. Furtado, P. Field, and J. Manners, 2014: A coupled cloud physics–radiation parameterization of the bulk optical properties of cirrus and its impact on the Met Office Unified Model Global Atmosphere 5.0 configuration. *J. Climate*, **27**, 7725–7752.

Barker, H., M. Jerg, T. Wehr, S. Kato, D. P. Donovan, and R. J. Hogan, 2011: A 3D cloud-construction algorithm for the EarthCARE satellite mission. *Q. J. R. Meteorol. Soc.*, **137**, 1042–1058.

Barker, H. W., 2008: Overlap of fractional cloud for radiation calculations in GCMs: A global analysis using CloudSat and CALIPSO data. *J. Geophys. Res.*, **113**.

Barker, H. W., J. N. Cole, J. Li, and K. von Salzen, 2016: A parametrization of 3-D subgrid-scale clouds for conventional GCMs: Assessment using A-Train satellite data and solar radiative transfer characteristics. *Journal of Advances in Modeling Earth Systems*.

Barker, H. W., J. N. Cole, J. Li, B. Yi, and P. Yang, 2015: Estimation of Errors in Two-Stream Approximations of the Solar Radiative Transfer Equation for Cloudy-Sky Conditions. *J. Atmos. Sci.*, **72**, 4053–4074.

Barker, H. W. and J. A. Davies, 1992: Cumulus cloud radiative properties and the characteristics of satellite radiance wavenumber spectra. *Remote Sensing of Environment*, **42**, 51–64.

Barker, H. W., G. L. Stephens, P. T. Partain, J. W. Bergman, B. Bonnel, K. Campana, E. E. Clothiaux, S. Clough, S. Cusack, J. Delamere, et al., 2003: Assessing 1D atmospheric solar radiative transfer models: Interpretation and handling of unresolved clouds. *J. Climate*, **16**, 2676–2699.

Benner, T. C. and K. F. Evans, 2001: Three-dimensional solar radiative transfer in small tropical cumulus fields derived from high-resolution imagery. *J. Geophys. Res.*, **106**, 14975–14984.

Boers, R., J. Jensen, P. Krummel, and H. Gerber, 1996: Microphysical and short-wave radiative structure of wintertime stratocumulus clouds over the Southern Ocean. *Q. J. R. Meteorol. Soc.*, **122**, 1307–1339.

Boucher, O. D. R., P. Artaxo, C. Bretherton, G. Feingold, P. Forster, V.-M. Kerminen, Y. Kondo, H. Liao, U. Lohmann, P. Rasch, S. K. Satheesh, S. Sherwood, B. Stevens, and X. Y. Zhang, 2013: Clouds and aerosols. *Climate Change 2013: The Physical Science Basis. Contribution of Working Group I to the Fifth Assessment Report of the Intergovernmental Panel on Climate Change*, T. Stocker, D. Qin, G.-K. Plattner, M. Tignor, S. Allen, J. Boschung, A. Nauels, Y. Xia, V. Bex, and P. Midgley, eds., Cambridge.

Cahalan, R., 1994: Bounded cascade clouds: Albedo and effective thickness. *Nonlinear Processes in Geophysics*, **1**, 156–167.

Cahalan, R. F. and J. H. Joseph, 1989: Fractal statistics of cloud fields. *Mon. Weath. Rev.*, **117**, 261–272.

Cahalan, R. F., L. Oreopoulos, A. Marshak, K. F. Evans, A. B. Davis, R. Pincus, K. H. Yetzer, B. Mayer, R. Davies, T. P. Ackerman, H. W. Barker, E. E. Clothiaux, R. G. Ellingson, M. J. Garay, E. Kassianov, S. Kinne, A. Macke, W. O'Hirok, P. T. Partain, S. M. Prigarin, A. N. Rublev, G. L. Stephens, F. Szczap, E. E. Takara, T. Várnai, G. Wen, and T. B. Zhuravleva, 2005: The I3RC: Bringing Together the Most Advanced Radiative Transfer Tools for Cloudy Atmospheres. *Bull. Amer. Meteor. Soc.*, **86**, 1275–1293, doi:10.1175/BAMS-86-9-1275.

Cahalan, R. F., W. Ridgway, W. J. Wiscombe, T. L. Bell, and J. B. Snider, 1994a: The albedo of fractal stratocumulus clouds. *J. Atmos. Sci.*, **51**, 2434–2455.

Cahalan, R. F., W. Ridgway, W. J. Wiscombe, and S. Gollmer, 1994b: Independent pixel and Monte Carlo estimates of stratocumulus albedo. *J. Atmos. Sci.*, **51**, 3776–3790.

Cahalan, R. F. and J. B. Snider, 1989: Marine stratocumulus structure. *Remote Sensing of Environment*, **28**, 95–107.

Cole, J. N. S., H. W. Barker, W. O'Hirok, E. E. Clothiaux, M. F. Khairoutdinov, and D. A. Randall, 2005: Atmospheric radiative transfer through global arrays of 2D clouds. *Geophys. Res. Lett.*, **32**.

Davis, A., A. Marshak, R. Cahalan, and W. Wiscombe, 1997: The Landsat scale break in stratocumulus as a three-dimensional radiative transfer effect: Implications for cloud remote sensing. *J. Atmos. Sci.*, **54**, 241–260.

Davis, A. B., A. Marshak, H. Gerber, and W. J. Wiscombe, 1999: Horizontal structure of marine boundary layer clouds from centimeter to kilometer scales. *J. Geophys. Res. Atmos.*, **104**, 6123–6144.

Dee, D. P., S. M. Uppala, A. J. Simmons, P. Berrisford, P. Poli, S. Kobayashi, U. Andrae, M. A. Balmaseda, G. Balsamo, P. Bauer, P. Bechtold, A. C. M. Beljaars, L. van de Berg, J. Bidlot, N. Bormann, C. Delsol, R. Dragani, M. Fuentes, A. J. Geer, L. Haimberger, S. B. Healy, H. Hersbach, E. V. Holm, L. Isaksen, P. Kållberg, M. Köhler, M. Matricardi, A. P. McNally, B. M. Monge-Sanz, J. Morcrette, B. Park, C. Peubey, P. de Rosnay,

C. Tavolato, J. Thépaut, and F. Vitart, 2011: The ERA-Interim reanalysis: Configuration and performance of the data assimilation system. *Q. J. R. Meteorol. Soc.*, **137**, 553–597.

Di Giuseppe, F. and A. M. Tompkins, 2003a: Effect of spatial organization on solar radiative transfer in three-dimensional idealized stratocumulus cloud fields. *J. Atmos. Sci.*, **60**, 1774–1794.

— 2003b: Three-dimensional radiative transfer in tropical deep convective clouds. *J. Geophys. Res.*, **108**, doi:10.1029/2003JD003392.

— 2015: Generalizing cloud overlap treatment to include the effect of wind shear. *J. Atmos. Sci.*, **72**, 2865–2876.

Duda, D. P., G. L. Stephens, and S. Cox, 1991: Microphysical and radiative properties of marine stratocumulus from tethered balloon measurements. *Journal of Applied Meteorology*, **30**, 170–186.

ECMWF, 2007: Part IV: Physical Processes. *IFS Documentation CY31R1*, ECMWF, IFS Documentation, Operational implementation 12 September 2006.

Edwards, J. M. and A. Slingo, 1996: Studies with a flexible new radiation code. I: Choosing a configuration for a large-scale model. *Q. J. R. Meteorol. Soc.*, **122**, 689–719.

Elsasser, W., 1942: *Heat Transfer by Infrared Radiation in the Atmosphere*, volume 6 of *Harvard Meteorological Studies*. Harvard University Press.

Emde, C. and B. Mayer, 2007: Simulation of solar radiation during a total eclipse: a challenge for radiative transfer. *Atmospheric Chemistry and Physics*, **7**, 2259–2270.

Euler, L., 1783: De serie lambertina plurimisque eius insignibus proprietatibus. *Acta Acad. Scient. Petropol*, **2**, 29–51.

Evans, K. F. and W. J. Wiscombe, 2004: An algorithm for generating stochastic cloud fields from radar profile statistics. *Atmospheric Research*, **72**, 263–289.

Falconer, K., 1990: Fractal geometry. *Mathematical Foundations and Applications*.

Fielding, M. D., 2014: *Retrieving Cloud Properties in 3D using Scanning Cloud Radar and Zenith Radiances for Shortwave Radiation Closure*. Ph.D. thesis, University of Reading, Department of Meteorology.

Fielding, M. D., J. C. Chiu, R. J. Hogan, and G. Feingold, 2013: 3D cloud reconstructions: Evaluation of scanning radar scan strategy with a view to surface shortwave radiation closure. *J. Geophys. Res. Atmos.*, **118**, 9153–9167.

— 2014: A novel ensemble method for retrieving properties of warm cloud in 3-D using ground-based scanning radar and zenith radiances. *J. Geophys. Res. Atmos.*, **119**.

Fu, Q., K. Liou, M. Cribb, T. Charlock, and A. Grossman, 1997: Multiple scattering parameterization in thermal infrared radiative transfer. *J. Atmos. Sci.*, **54**, 2799–2812.

Gounou, A. and R. J. Hogan, 2007: A sensitivity study of the effect of horizontal photon transport on the radiative forcing of contrails. *J. Atmos. Sci.*, **64**, 1706–1716.

Harshvardhan and D. A. Randall, 1985: Comments on the parameterization of radiation for numerical weather prediction and climate models. *Mon. Weath. Rev.*, **113**, 1832–1833.

Heidinger, A. K. and S. K. Cox, 1996: Finite-cloud effects in longwave radiative transfer. *J. Atmos. Sci.*, **53**, 953–963.

Heus, T., C. C. van Heerwaarden, H. J. J. Jonker, A. P. Siebesma, S. Axelsen, K. van den Dries, O. Geoffroy, A. F. Moene, D. Pino, S. de Roode, et al., 2010: Formulation of and numerical studies with the Dutch Atmospheric Large-Eddy Simulation (DALES). *Geosci. Model. Dev.*, **3**, 415–444.

Heymsfield, A. J., A. Bansemer, P. R. Field, S. L. Durden, J. L. Stith, J. E. Dye, W. Hall, and C. A. Grainger, 2002: Observations and parameterizations of particle size distributions in deep tropical cirrus and stratiform precipitating clouds: Results from in situ observations in TRMM field campaigns. *J. Atmos. Sci.*, **59**, 3457–3491.

Hinkelman, L. M., K. F. Evans, E. E. Clothiaux, T. P. Ackerman, and P. W. Stackhouse Jr, 2007: The effect of cumulus cloud field anisotropy on domain-averaged solar fluxes and atmospheric heating rates. *J. Atmos. Sci.*, **64**, 3499–3520.

Hinkelman, L. M., B. Stevens, and K. F. Evans, 2005: A large-eddy simulation study of anisotropy in fair-weather cumulus cloud fields. *J. Atmos. Sci.*, **62**, 2155–2171.

Hogan, R. J. and A. J. Illingworth, 2000: Deriving cloud overlap statistics from radar. *Q. J. R. Meteorol. Soc.*, **126**, 2903–2909.

Hogan, R. J. and S. F. Kew, 2005: A 3D stochastic cloud model for investigating the radiative properties of inhomogeneous cirrus clouds. *Q. J. R. Meteorol. Soc.*, **131**, 2585–2608.

Hogan, R. J., S. A. K. Schäfer, C. Klinger, J. C. Chiu, and B. Mayer, 2016: Representing 3-D cloud radiation effects in two-stream schemes: 2. Matrix formulation and broadband evaluation. *J. Geophys. Res. Atmos.*, 8583–8599, doi:10.1002/2016JD024875.

Hogan, R. J. and J. K. P. Shonk, 2013: Incorporating the effects of 3D radiative transfer in the presence of clouds into two-stream multilayer radiation schemes. *J. Atmos. Sci.*, **70**, 708–724.

Hogan, R. J., L. Tian, P. R. Brown, C. D. Westbrook, A. J. Heymsfield, and J. D. Eastment, 2012: Radar scattering from ice aggregates using the horizontally aligned oblate spheroid approximation. *J. Appl. Meteorol*, **51**, 655–671.

Illingworth, A. J., H. W. Barker, A. Beljaars, M. Ceccaldi, H. Chepfer, N. Clerbaux, J. Cole, J. Delanoë, C. Domenech, D. P. Donovan, et al., 2015: The EarthCARE satellite: The next step forward in global measurements of clouds, aerosols, precipitation, and radiation. *Bull. Amer. Meteor. Soc.*, **96**, 1311–1332.

Illingworth, A. J., R. J. Hogan, E. J. O'Connor, D. Bouniol, M. E. Brooks, J. Delanoë, D. P. Donovan, J. D. Eastment, N. Gaussiat, J. W. F. Goddard, M. Haeffelin, H. Klein Baltink, O. A. Krasnov, J. Pelon, J. Piriou, A. Protat, H. W. J. Russchenberg, A. Seifert, A. M. Tompkins, G. van Zadelhoff, F. Vinit, U. Willén, D. R. Wilson, and C. Wrench, 2007: Cloudnet. *Bull. Amer. Meteor. Soc.*, **88**, 883.

Jakub, F. and B. Mayer, 2015: A Three-Dimensional Parallel Radiative Transfer Model for Atmospheric Heating Rates for use in Cloud Resolving Models—the TenStream solver. *Journal of Quantitative Spectroscopy and Radiative Transfer*.

Jensen, M. P., A. M. Vogelmann, W. D. Collins, G. J. Zhang, and E. P. Luke, 2008: Investigation of regional and seasonal variations in marine boundary layer cloud properties from MODIS observations. *J. Climate*, **21**, 4955–4973, doi:10.1175/2008JCLI1974.1.

Jiang, X., D. E. Waliser, J.-L. Li, and C. Woods, 2011: Vertical cloud structures of the boreal summer intraseasonal variability based on CloudSat observations and ERA-Interim reanalysis. *Climate Dynamics*, **36**, 2219–2232.

Justice, C. O., E. Vermote, J. R. Townshend, R. Defries, D. P. Roy, D. K. Hall, V. V. Salomonson, J. L. Privette, G. Riggs, A. Strahler, et al., 1998: The Moderate Resolution Imaging Spectroradiometer (MODIS): Land remote sensing for global change research. *IEEE Transactions on Geoscience and Remote Sensing*, **36**, 1228–1249.

Kablick III, G. P., R. G. Ellingson, E. E. Takara, and J. Gu, 2011: Longwave 3D benchmarks for inhomogeneous clouds and comparisons with approximate methods. *J. Climate*, **24**, 2192–2205.

Kidd, C., V. Levizzani, and P. Bauer, 2009: A review of satellite meteorology and climatology at the start of the twenty-first century. *Progress in Physical Geography*, **33**, 474–489.

Killen, R. M. and R. G. Ellingson, 1994: The effect of shape and spatial distribution of cumulus clouds on longwave irradiance. *J. Atmos. Sci.*, **51**, 2123–2136.

Klinger, C. and B. Mayer, 2014: Three-dimensional Monte Carlo calculation of atmospheric thermal heating rates. *Journal of Quantitative Spectroscopy and Radiative Transfer*, **144**, 123–136.

— 2016: The Neighboring Column Approximation (NCA)—A fast approach for the calculation of 3D thermal heating rates in cloud resolving models. *Journal of Quantitative Spectroscopy and Radiative Transfer*, **168**, 17–28.

Kneifel, S., M. Kulie, and R. Bennartz, 2011: A triple-frequency approach to retrieve microphysical snowfall parameters. *J. Geophys. Res. Atmos.*, **116**.

Kollias, P., N. Bharadwaj, K. Widener, I. Jo, and K. Johnson, 2014a: Scanning ARM cloud radars. Part I: Operational sampling strategies. *Journal of Atmospheric and Oceanic Technology*, **31**, 569–582.

Kollias, P., I. Jo, P. Borque, A. Tatarevic, K. Lamer, N. Bharadwaj, K. Widener, K. Johnson, and E. E. Clothiaux, 2014b: Scanning ARM cloud radars. Part II: Data quality control and processing. *Journal of Atmospheric and Oceanic Technology*, **31**, 583–598.

Koren, I., L. A. Remer, Y. J. Kaufman, Y. Rudich, and J. V. Martins, 2007: On the twilight zone between clouds and aerosols. *Geophys. Res. Lett.*, **34**.

Kummerow, C., W. Barnes, T. Kozu, J. Shiue, and J. Simpson, 1998: The tropical rainfall measuring mission (TRMM) sensor package. *Journal of Atmospheric and Oceanic Technology*, **15**, 809–817.

Lambert, J. H., 1758: Observationes variae in mathesin puram. *Acta Helvetica*, **3**, 128–168.

Lovejoy, S., 1982: Area-perimeter relation for rain and cloud areas. *Science*, **216**, 185–187.

Mandelbrot, B. B., 1967: How long is the coast of Britain. *Science*, **156**, 636–638.

— 1977: *Fractals*. Wiley Online Library.

— 1983: *The fractal geometry of nature*, volume 173. Macmillan.

Marshak, A., A. Davis, R. Cahalan, and W. Wiscombe, 1994: Bounded cascade models as nonstationary multifractals. *Physical Review E*, **49**, 55.

Marshak, A., A. Davis, R. F. Cahalan, and W. Wiscombe, 1998: Nonlocal independent pixel approximation: Direct and inverse problems. *IEEE Transactions on Geoscience and Remote Sensing*, **36**, 192–205.

Marshak, A., A. Davis, W. Wiscombe, and R. Cahalan, 1995: Radiative smoothing in fractal clouds. *J. Geophys. Res.*, **100**, 26247–26261.

Mayer, B., 2009: Radiative transfer in the cloudy atmosphere. *ERCA 2008—From the Human Dimensions of Global Environmental Change to the Observation of the Earth From Space*, vol. 1, C. Boutron, ed., EPJ Web of Conf., Grenoble, France, volume 1, 75–99.
URL `http://dx.doi.org/10.1140/epjconf/e2009-00912-1`

Mayer, B., S. Hoch, and C. Whiteman, 2010: Validating the MYSTIC three-dimensional radiative transfer model with observations from the complex topography of Arizona's Meteor Crater. *Atmospheric Chemistry and Physics*, **10**, 8685–8696.

Mayer, B. and A. Kylling, 2005: Technical note: The libRadtran software package for radiative transfer calculations — description and examples of use. *Atmospheric Chemistry and Physics*, **5**, 1855–1877.

Meador, W. and W. Weaver, 1980: Two-stream approximations to radiative transfer in planetary atmospheres: A unified description of existing methods and a new improvement. *J. Atmos. Sci.*, **37**, 630–643.

Minnis, P., D. F. Young, S. Sun-Mack, P. W. Heck, D. R. Doelling, and Q. Z. Trepte, 2004: CERES cloud property retrievals from imagers on TRMM, Terra, and Aqua. *Remote Sensing*, International Society for Optics and Photonics, 37–48.

Mlawer, E. J., S. J. Taubman, P. D. Brown, M. J. Iacono, and S. A. Clough, 1997: Radiative transfer for inhomogeneous atmospheres: RRTM, a validated correlated-*k* model for the longwave. *J. Geophys. Res.*, **102**, 16663–16682.

Moeng, C. H., W. R. Cotton, B. Stevens, C. Bretherton, H. A. Rand, A. Chlond, M. Khairoutdinov, S. Krueger, W. Lewellen, M. MacVean, et al., 1996: Simulation of a stratocumulus-topped planetary boundary layer: Intercomparison among different numerical codes. *Bull. Amer. Meteor. Soc.*, **77**, 261–278.

Mokhov, I. L. and M. E. Schlesinger, 1994: Analysis of global cloudiness: 2. Comparison of ground-based and satellite-based cloud climatologies. *J. Geophys. Res. Atmos.*, **99**, 17045–17065.

Morcrette, C. J., 2012: Improvements to a prognostic cloud scheme through changes to its cloud erosion parametrization. *Atmospheric Science Letters*, **13**, 95–102.

Morcrette, J.-J., P. Bechtold, A. Beljaars, A. Benedetti, A. Bonet, F. Doblas-Reyes, J. Hague, M. Hamrud, J. Haseler, J. Kaiser, M. Leutbecher, G. Mozdzynski, M. Razinger, D. Salmond, S. Serrar, M. Suttie, A. Tompkins, A. Untch, and A. Weisheimer, 2007: Recent advances in radiation transfer parametrizations. 50 pp.

Morcrette, J.-J. and Y. Fouquart, 1986: The overlapping of cloud layers in shortwave radiation parameterizations. *J. Atmos. Sci.*, **43**, 321–328.

Myhre, G., D. Shindell, F.-M. Bréon, W. Collins, J. Fuglestvedt, J. Huang, D. Koch, J.-F. Lamarque, D. Lee, B. Mendoza, T. Nakajima, A. Robock, G. Stephens, T. Takemura, and H. Zhang, 2013: Anthropogenic and natural radiative forcing. *Climate Change 2013: The Physical Science Basis. Contribution of Working Group I to the Fifth Assessment Report of the Intergovernmental Panel on Climate Change*, T. Stocker, D. Qin, G.-K. Plattner, M. Tignor, S. Allen, J. Boschung, A. Nauels, Y. Xia, V. Bex, and P. Midgley, eds., Cambridge.

Neggers, R., H. Jonker, and A. Siebesma, 2003a: Size statistics of cumulus cloud populations in large-eddy simulations. *J. Atmos. Sci.*, **60**, 1060–1074.

Neggers, R. A. J., P. G. Duynkerke, and S. M. A. Rodts, 2003b: Shallow cumulus convection: A validation of large-eddy simulation against aircraft and Landsat observations. *Q. J. R. Meteorol. Soc.*, **129**, 2671–2696.

Oreopoulos, L. and H. W. Barker, 1999: Accounting for subgrid-scale cloud variability in a multi-layer 1D solar radiative transfer algorithm. *Q. J. R. Meteorol. Soc.*, **125**, 301–330.

Paquin-Ricard, D., P. A. Vaillancourt, H. W. Barker, and J. N. S. Cole, 2016: A Comparison of Two Representations of Subgrid-scale Cloud Structure in a Global Model: Radiative Effects as a Function of Cloud Characteristics. *Q. J. R. Meteorol. Soc.*, 2551–2561.

Petty, G. W., 2006: *A first course in atmospheric radiation*. Sundog.

Pincus, R., H. W. Barker, and J.-J. Morcrette, 2003: A fast, flexible, approximate technique for computing radiative transfer in inhomogeneous cloud fields. *J. Geophys. Res.*, **108**.

Pincus, R. and K. F. Evans, 2009: Computational cost and accuracy in calculating three-dimensional radiative transfer: Results for new implementations of Monte Carlo and SHDOM. *J. Atmos. Sci.*, **66**, 3131–3146, doi:10.1175/2009JAS3137.1.

Pincus, R., C. Hannay, and K. F. Evans, 2005: The accuracy of determining three-dimensional radiative transfer effects in cumulus clouds using ground-based profiling instruments. *J. Atmos. Sci.*, **62**, 2284–2293.

Pincus, R., S. Platnick, S. A. Ackerman, R. S. Hemler, and R. J. P. Hofmann, 2012: Reconciling Simulated and Observed Views of Clouds: MODIS, ISCCP, and the Limits of Instrument Simulators. *J. Climate*, **25**, 4699–4720, doi:10.1175/JCLI-D-11-00267.1.

Plank, V. G., 1969: The size distribution of cumulus clouds in representative Florida populations. *J. Appl. Meteorol*, **8**, 46–67.

Platnick, S., M. D. King, S. A. Ackerman, W. P. Menzel, B. A. Baum, J. C. Riédi, and R. A. Frey, 2003: The MODIS cloud products: Algorithms and examples from Terra. *IEEE Transactions on Geoscience and Remote Sensing*, **41**, 459–473.

Prigarin, S. M. and A. Marshak, 2009: A simple stochastic model for generating broken cloud optical depth and cloud-top height fields. *J. Atmos. Sci.*, **66**, 92–104.

Randall, D., M. Khairoutdinov, A. Arakawa, and W. Grabowski, 2003: Breaking the cloud parameterization deadlock. *Bull. Amer. Meteor. Soc.*, **84**, 1547.

Roy, D. P., M. A. Wulder, T. R. Loveland, C. E. Woodcock, R. G. Allen, M. C. Anderson, D. Helder, J. R. Irons, D. M. Johnson, R. Kennedy, et al., 2014: Landsat-8: Science and product vision for terrestrial global change research. *Remote Sensing of Environment*, **145**, 154–172.

Schäfer, S. A. K., R. J. Hogan, C. Klinger, J. C. Chiu, and B. Mayer, 2016: Representing 3-D cloud radiation effects in two-stream schemes: 1. Longwave considerations and effective cloud edge length. *J. Geophys. Res. Atmos.*, 8567–8582, doi:10.1002/2016JD024876.

Schiffer, R. A. and W. B. Rossow, 1983: The International Satellite Cloud Climatology Project(ISCCP) - The first project of the World Climate Research Programme. *Bull. Amer. Meteor. Soc.*, **64**, 779–784.

Shonk, J. K. P. and R. J. Hogan, 2008: Tripleclouds: An efficient method for representing horizontal cloud inhomogeneity in 1D radiation schemes by using three regions at each height. *J. Climate*, **21**, 2352–2370.

— 2010: Effect of improving representation of horizontal and vertical cloud structure on the earth's global radiation budget. Part II: The global effects. *Q. J. R. Meteorol. Soc.*, **136**, 1205–1215.

Shonk, J. K. P., R. J. Hogan, J. M. Edwards, and G. G. Mace, 2010: Effect of improving representation of horizontal and vertical cloud structure on the earth's global radiation budget. Part I: Review and parametrization. *Q. J. R. Meteorol. Soc.*, **136**, 1191–1204.

Siebesma, A. and H. Jonker, 2000: Anomalous scaling of cumulus cloud boundaries. *Phys. Rev. Let.*, **21**, 214–217.

Stein, T. H., R. J. Hogan, K. E. Hanley, J. C. Nicol, H. W. Lean, R. S. Plant, P. A. Clark, and C. A. Halliwell, 2014: The three-dimensional morphology of simulated and observed convective storms over southern England. *Mon. Weath. Rev.*, **142**, 3264–3283.

Stein, T. H. M., R. J. Hogan, P. A. Clark, C. E. Halliwell, K. E. Hanley, H. W. Lean, J. C. Nicol, and R. S. Plant, 2015a: The DYMECS project: A statistical approach for the evaluation of convective storms in high-resolution NWP models. *Bull. Amer. Meteor. Soc.*, **96**, 939–951.

Stein, T. H. M., C. D. Westbrook, and J. C. Nicol, 2015b: Fractal geometry of aggregate snowflakes revealed by triple-wavelength radar measurements. *Geophys. Res. Lett.*, **42**, 176–183.

Stephens, G. L., 1985: Reply (to Comments on The parameterization of radiation for numerical weather prediction and climate models). *Mon. Weath. Rev.*, **113**, 1834–1835.

— 2003: The useful pursuit of shadows. *American Scientist*, **91**, 442–449.

Stephens, G. L., J. Li, M. Wild, C. A. Clayson, N. Loeb, S. Kato, T. L'Ecuyer, P. W. Stackhouse Jr, M. Lebsock, and T. Andrews, 2012: An update on Earth's energy balance in light of the latest global observations. *Nature Geoscience*, **5**, 691–696.

Stephens, G. L., D. G. Vane, R. J. Boain, G. G. Mace, K. Sassen, Z. Wang, A. J. Illingworth, E. J. O'Connor, W. B. Rossow, S. L. Durden, et al., 2002: The CloudSat mission and the A-Train: A new dimension of space-based observations of clouds and precipitation. *Bull. Amer. Meteor. Soc.*, **83**, 1771–1790.

Stokes, G. M. and S. E. Schwartz, 1994: The Atmospheric Radiation Measurement (ARM) Program: Programmatic background and design of the cloud and radiation test bed. *Bull. Amer. Meteor. Soc.*, **75**, 1201–1221.

Szczypta, C., J. Calvet, C. Albergel, G. Balsamo, S. Boussetta, D. Carrer, S. Lafont, and C. Meurey, 2011: Verification of the new ECMWF ERA-Interim reanalysis over France. *Hydrology and Earth System Sciences*, **15**, 647–666.

Takara, E. E. and R. G. Ellingson, 2000: Broken cloud field longwave-scattering effects. *J. Atmos. Sci.*, **57**, 1298–1310.

Tao, W.-K. and J. Simpson, 1993: The Goddard cumulus ensemble model. Part I: Model description. *Terr. Atmos. Oceanic Sci.*, **4**, 35–72.

Tao, W.-K., J. Simpson, D. Baker, S. Braun, M.-D. Chou, B. Ferrier, D. Johnson, A. Khain, S. Lang, B. Lynn, et al., 2003: Microphysics, radiation and surface processes in the Goddard Cumulus Ensemble (GCE) model. *Meteorology and Atmospheric Physics*, **82**, 97–137.

Tiedtke, M., 1993: Representation of clouds in large-scale models. *Mon. Weath. Rev.*, **121**, 3040–3061.

Tompkins, A. M., 2001: Organization of tropical convection in low vertical wind shears: The role of cold pools. *J. Atmos. Sci.*, **58**, 1650–1672.

Várnai, T. and R. Davies, 1999: Effects of cloud heterogeneities on shortwave radiation: Comparison of cloud-top variability and internal heterogeneity. *J. Atmos. Sci.*, **56**, 4206–4224.

Waliser, D. E. and C. Gautier, 1993: A satellite-derived climatology of the ITCZ. *J. Climate*, **6**, 2162–2174.

Welch, R. and B. Wielicki, 1984: Stratocumulus cloud field reflected fluxes: The effect of cloud shape. *J. Atmos. Sci.*, **41**, 3085–3103.

Wielicki, B. A., B. R. Barkstrom, E. F. Harrison, R. B. Lee III, G. Louis Smith, and J. E. Cooper, 1996: Clouds and the Earth's Radiant Energy System (CERES): An earth observing system experiment. *Bull. Amer. Meteor. Soc.*, **77**, 853–868.

Wielicki, B. A. and R. M. Welch, 1986: Cumulus cloud properties derived using Landsat satellite data. *Journal of Climate and Applied Meteorology*, **25**, 261–276.

Winker, D. M., J. R. Pelon, and M. P. McCormick, 2003: The CALIPSO mission: Spaceborne lidar for observation of aerosols and clouds. *Third International Asia-Pacific Environmental Remote Sensing Remote Sensing of the Atmosphere, Ocean, Environment, and Space*, International Society for Optics and Photonics, 1–11.

Wood, R. and P. R. Field, 2011: The distribution of cloud horizontal sizes. *J. Climate*, **24**, 4800–4816.

Zhong, W., R. J. Hogan, and J. D. Haigh, 2008: Three-dimensional radiative transfer in midlatitude cirrus clouds. *Q. J. R. Meteorol. Soc.*, **134**, 199–215.

Zib, B. J., X. Dong, B. Xi, and A. Kennedy, 2012: Evaluation and intercomparison of cloud fraction and radiative fluxes in recent reanalyses over the Arctic using BSRN surface observations. *J. Climate*, **25**, 2291–2305.

Zinner, T., A. Marshak, S. Lang, J. V. Martins, and B. Mayer, 2008: Remote sensing of cloud sides of deep convection: towards a three-dimensional retrieval of cloud particle size profiles. *Atmospheric Chemistry and Physics*, **8**, 4741–4757.

Zuidema, P. and K. F. Evans, 1998: On the validity of the independent pixel approximation for boundary layer clouds observed during ASTEX. *J. Geophys. Res.*, **103**, 6059–6074.

Zygmuntowska, M., T. Mauritsen, J. Quaas, and L. Kaleschke, 2012: Arctic Clouds and Surface Radiation — a critical comparison of satellite retrievals and the ERA-Interim reanalysis. *Atmospheric Chemistry and Physics*, **12**, 6667–6677.